

Jets from X-ray Binaries to Active Galactic Nuclei

Dissertation

zur

Erlangung des Doktorgrades (Dr. rer. nat.)

der

Mathematisch-Naturwissenschaftlichen Fakultät

der

Rheinischen Friedrich-Wilhelms-Universität Bonn

vorgelegt von

Elmar Körding

aus

Darmstadt

Bonn 2004

Angefertigt mit Genehmigung der Mathematisch-Naturwissenschaftlichen
Fakultät der Rheinischen Friedrich-Wilhelms-Universität Bonn

1. Referent: Prof. Dr. Heino Falcke
2. Referent: Prof. Dr. Peter Schneider

Tag der Promotion: 21.9.2004

Diese Dissertation ist auf dem Hochschulschriftenserver der ULB Bonn
http://hss.ulb.uni-bonn.de/diss_online elektronisch publiziert.

Summary

It is generally believed that active galactic nuclei (AGN) and black hole X-ray binaries (XRBS) have a similar central engine and that they could be described with a unified model. However, this model is not yet established. In this thesis we present a symbiotic disk/jet model for both classes. Energy and mass conservation can be used to derive scaling laws for the emission of a jet. This allows us to identify the main parameters of the system: the mass of the central black hole and the accretion rate.

We follow the idea that the spectral energy distributions (SEDs) of all slowly accreting black holes are probably jet dominated while highly accreting black holes are thermally dominated. Thus, the developed model can be used to argue for a unifying view of all slowly accreting black holes: a unification of XRBS and AGN. We classify the zoo of AGN in jet and disk dominated sources and test our unification scheme of slowly accreting sources by establishing a universal radio/X-ray correlation for XRBS and AGN.

Our model is further tested by exploring the phenomenon of ultra-luminous X-ray sources (ULXs) which are bright off-nucleus X-ray point sources. If the central engine of XRBS and AGN is indeed similar, there should be a stellar analogue of a blazar (a blazar is an AGN with its relativistic jet pointing towards the observer). We have shown that these microblazars can indeed explain the known population of ULXs. As the detection of a compact radio core at the positions of the ULX would strongly support this explanation, we have monitored a sample of ULXs to search for radio flares and continuous emission. We interpret the non-detections in the context of the universal radio/X-ray correlation.

Finally we investigated if the complex timing behavior of accreting black holes is in agreement with our jet model. The power law in the spectrum created by synchrotron emission originates mainly from one area in the jet. Thus, the power law in the SED can only vary in intensity and spectral index. Such a pivoting power law can be used to explain the Fourier time lags and other statistical properties of XRBS. Thus our disk/jet model is in agreement with the observations and connects stellar mass XRBS to the supermassive AGN.

Contents

1	Introduction	1
1.1	The Current Paradigm	4
1.2	Scope of the Thesis	8
2	Jet Scaling	9
2.1	Introduction	9
2.2	Relativistic Hydrodynamics	10
2.3	The Jet-Disk Connection	12
2.3.1	Enthalpy and Internal Energy of the Jet	12
2.3.2	Relativistic Particles	14
2.3.3	The Parameters	16
2.4	Emission from the Jet	18
2.4.1	Synchrotron Emission	18
2.4.2	Compton Emission	23
2.4.3	High Energy Cut-off	28
2.5	Scaling of the Jet	29
2.5.1	Synchrotron Emission	30
2.5.2	Synchrotron Self-Compton Emission	32
2.5.3	The Assumption of Equipartition	33
2.5.4	Dependence on the Parameters	35
2.6	Discussion	39
3	A Scheme to Unify Low-Power Accreting Black Holes	41
3.1	Introduction	41
3.2	Low-Power Unification	43
3.2.1	A Scheme for Sub-Eddington Black Holes	43

3.2.2	Consequences and Tests of our Proposed Unification Scheme	47
3.3	The X-Ray/Radio Correlations	47
3.3.1	The Predicted Scaling	47
3.3.2	The Scaling of Synchrotron Self-Compton Emission	51
3.3.3	The Samples	52
3.3.4	Results	57
3.4	Mass Estimates from the Radio/X-Ray Correlation	58
3.5	Conclusion and Discussion	58
4	Ultra-Luminous X-ray Sources	65
4.1	Introduction	65
4.2	Simple Models	67
4.2.1	The Jet/Disk Model	67
4.2.2	The Disk-Only Model	70
4.3	Data	70
4.4	Results	71
4.5	Summary and Discussion	73
5	Radio Observations of ULXs	75
5.1	Introduction	75
5.2	Observations	76
5.2.1	Sample Selection	76
5.2.2	Observing Scheme	76
5.3	Observational Results	79
5.3.1	Error Limits	79
5.3.2	Non-Detections	79
5.3.3	M82	80
5.4	Theoretical Interpretations	83
5.4.1	Flares	83
5.4.2	Background Sources	86
5.4.3	Steady State Emission	87
5.4.4	Other Radio Detections of ULXs	88
5.5	Conclusions	89
5.6	Appendix: The LLAGN in NGC 4736	90

6	Short Time Variability of XRBs	93
6.1	Introduction	93
6.2	Parameterization of the Pivoting Power Law Model	96
6.3	Analytic Results	99
6.3.1	Definition and Energy Dependence of Phase Lags	99
6.3.2	Fourier Frequency Dependence of the Phase Lag	100
6.3.3	Cross-Correlation Function	102
6.3.4	Negative Correlation of Hardness and Flux	105
6.4	Monte Carlo Simulations	106
6.5	Applications to BHXRBs	108
6.5.1	Photon Energy Dependence of the Phase Lags	108
6.5.2	Fourier Frequency Dependence of the Phase Lags	109
6.5.3	Auto- and Cross-Correlation Function	111
6.5.4	Coherence Function	111
6.5.5	Failed State Transitions	113
6.6	Summary and Conclusions	114
6.7	Appendix: Derivation of the phase lags	117
6.8	Appendix: Derivation of the cross-correlation function	119
7	Conclusions	121
8	Acknowledgments	139

1

Introduction

Accretion is probably the most powerful source of energy available in the Universe. It is thought to power active galactic nuclei (AGN): compact sources which can be more luminous than a whole galaxy. It is also the energy source of X-ray binaries (XRBs), cataclysmic variables (CVs) and has a strong impact on young stellar objects (YSOs). Accretion is therefore a central theme in modern astronomy.

However, its mysteries are far from solved. A good understanding of its physics will help to understand the central object and to understand why the accretion process seems to be intrinsically coupled to the ejection of jets (e.g., YSO: Bachiller 1996, XRBs: Mirabel & Rodríguez 1999, AGN: Zensus 1997). The emission from jets in many cases contributes significantly to or even dominates the overall emission. Furthermore, the kinetic power of the jet can significantly alter its surrounding medium. In this thesis we establish and test a unifying view of the jet-dominated sources of all masses and power.

The accretion and ejection process can be best studied for black holes, because they can be described by very few parameters, namely their mass and spin. Due to their event horizon there is no radiation or magnetic field coming from the central object itself, only the accretion flow and the jet are visible. Black holes started as a mathematical concept with the development of general relativity (Schwarzschild 1916), but in recent years there is increasing evidence that this concept is indeed realized in nature. The most certain cases are probably the center of our Galaxy (c.f., Melia & Falcke 2001 and references therein) or NGC 4258 (Miyoshi et al. 1995), but there are numerous other indirect arguments for the existence of black holes (e.g, Narayan & Heyl 2002).

The accretion flow around a black hole can reach down to the innermost stable orbit, where general relativistic effects play an important role. Thus, these exciting objects provide an opportunity to study general relativity but we have to understand the accretion and ejection process to use it as a tool.

A good understanding of black holes in the Universe is not only interesting in its own right but is also important for cosmology, galaxy evolution and early star formation. They also play an important role for astro-particle physics, as they are major sources of high-energy particles and photons (Rachen & Biermann 1993). Until now we know two islands of black holes: supermassive and stellar mass black holes. Supermassive black holes are thought to be in the center of every galaxy (Kormendy & Richstone 1995) where, if they accrete, they reveal their existence as AGN. An XRB is thought to be a close binary system of a compact object (neutron star or black hole) and a star. Mass donated by the star will accrete on the compact object. Stellar-mass black holes can be observed in those XRBs, whose compact object is too heavy to be neutron star. Currently there are of the order of 10 active black hole XRBs known. Until now no intermediate-mass black holes have been unambiguously identified, although there are some recent candidates (see e.g., Colbert & Mushotzky 1999; Strohmayer & Mushotzky 2003). Besides their possible existence in the center of globular clusters such black holes are also expected as remnants of primordial stars. This ‘missing link’ between the supermassive and stellar black holes is also important for cosmology, as the central black holes of galaxies seem to be connected to galaxy evolution through the bulge/black-hole mass correlation (Gebhardt et al. 2000; Ferrarese & Merritt 2000).

It is generally believed that AGN and XRBs have a similar geometry (Mirabel & Rodríguez 1998; Mirabel & Rodríguez 1999): a central black hole surrounded by an accretion disk which usually powers a relativistic jet. They differ mainly in the scales and the source of accreting material. Quasars, one type of AGN, are among the brightest objects in the Universe and are visible up to very high redshifts. They and other AGN harbor supermassive black holes with up to $10^9 M_{\odot}$ and powerful jets extending millions of parsecs (see also the bottom of Fig. 1.3), while black hole XRBs have stellar masses. Microquasars, i.e., XRBs showing radio jets, have jets reaching only a few light years (see Fig. 1.1). Thus, the time scales for accretion and injection processes also differ by many orders of magnitude, so that a process that may require hundreds of years to evolve in an AGN can be observed in hours in an XRB. To understand the physics of AGN and XRBs it is therefore important to look at both classes and to use the knowledge of one class to understand the other.

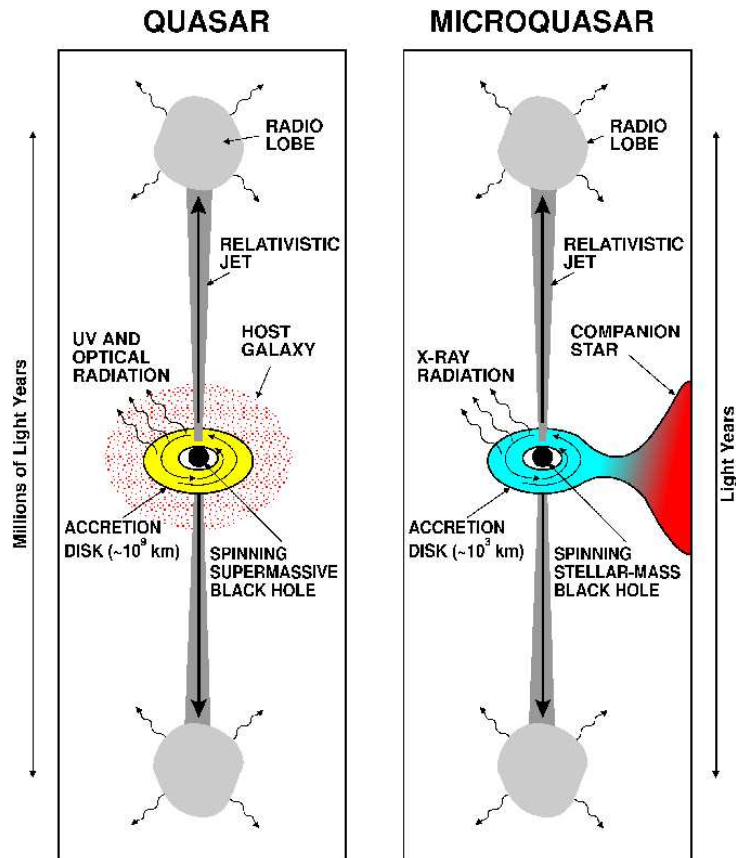


FIGURE 1.1— The quasar-microquasar analogy, reproduced from Mirabel & Rodriguez (1998). Both types objects have a similar central engine: a black hole surrounded by an accretion disk. Only the mass donor is different.

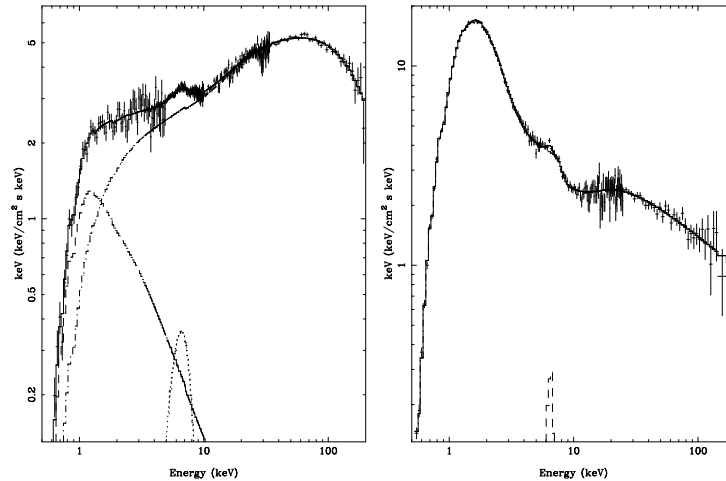


FIGURE 1.2— On the left: Low hard state of Cyg X-1, the overall spectrum is dominated by a hard power law. On the right: The high state is dominated by thermal emission. This plot has been reproduced from Frontera et al. (2001).

However, both classes cover distinct parameter spaces and the connection is complicated by the zoo of different types of AGN (Antonucci 1993) and the variety of different spectral states exhibited by XRBs. The most prominent states (c.f., Tanaka & Shibazaki 1996) are the low hard state (hard power law in the X-ray spectrum, see Fig. 1.2), the high state (soft thermal spectrum, Fig. 1.2), and the very high state (soft power law in the X-rays). The spectra are usually modeled using emission from an accretion disk and a hot corona (Sunyaev & Trümper 1979). However, there is an ongoing discussion about how much the relativistic jet contributes to the overall emission (Falcke & Biermann 1999; Markoff et al. 2001a; Zdziarski & Gierlinski 2004). This thesis further explores the effects of the jet on the appearance of AGN and XRBs and thus tries to connect the two islands of known black holes. This connection is crucial to exploit synergies between the two fields of research and may lead to a better understanding of black holes in general.

1.1 The Current Paradigm

The observed emission from AGN and XRBs is usually interpreted using different concepts. Models for radio-loud AGN involve jets, which are probably responsible for the broad band emission (radio to γ -rays). For a prototype ra-

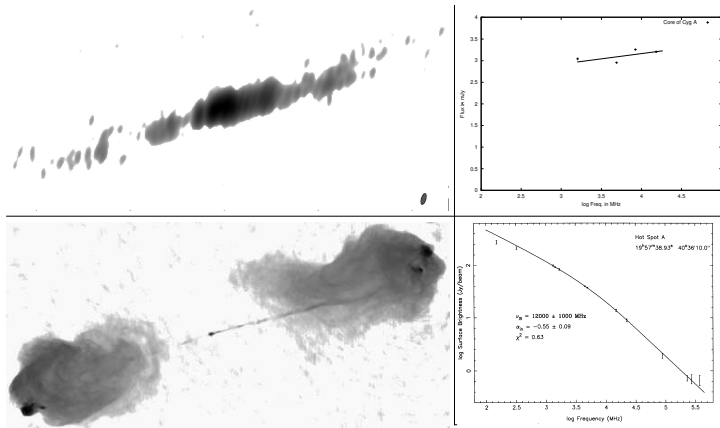


FIGURE 1.3— Top: Map of the central region of Cygnus-A together with the flat spectrum of the core component measured with very long baseline interferometry (Kindly provided by Bach 2004). In this thesis we concentrate on the emission from the core. Bottom: Large scale radio-map (from the Very Large Array) of Cygnus-A and steep spectrum of one hot-spot. The hot-spots dominate the overall spectrum of the source. Reproduced from Perley et al. (1984) and Carilli et al. (1991)

dio galaxy see Fig. 1.3, where we show Cyg A on small and large scales. In this thesis we concentrate on the emission from the central core. The accretion disk and its corona are mainly used to explain the thermal component and partly the power law X-ray emission. The prominence of the jet in the spectral energy density (SED) of radio-quiet AGN is still under debate. Most models for XRBs, even for radio-loud microquasars, focus on the accretion flow only. Only recently is the effect of jets being discussed (Falcke & Biermann 1999; Markoff et al. 2001a; Fender 2001).

As mentioned above, XRBs are observed in a number of different spectral states, which are thought to be created by different accretion flow geometries. From these states the low hard and the high soft state are the most common. The low hard state is often found in weakly accreting systems and the system changes its state once it reaches a critical accretion rate. The high state is characterized by bright soft component (see Fig. 1.2), which is interpreted as thermal disk emission. Here and for the very high state the standard geometrically thin, optically thick disk probably reaches in to the innermost stable radii (see Fig. 1.4) and may be accompanied by a hot corona (see e.g., Shakura & Sunyaev 1973; Haardt & Maraschi 1991). Besides looking at the continuum

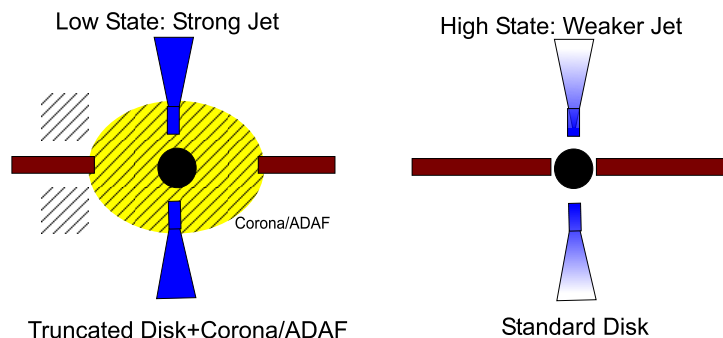


FIGURE 1.4— Sketch of the low and high state. In the low state the standard disk is truncated and turn into an radiative inefficient accretion flow.

spectra, this idea can be tested by the observation of the iron line emission, which can be explained by fluorescence in the innermost parts of the disk (see e.g., Miller et al. 2001). For strongly accreting XRBs the jet is only visible in the very high state; in the high state it seems to be quenched or non existent.

Low-state objects on the other hand have truncated standard disks (Esin et al. 1997), for a sketch see Fig. 1.4. The accretion flow turns into a radiatively inefficient flow in the innermost region at the transition radius (ADAF or similar; Narayan & Yi 1994). This thick disk usually powers a relativistic jet. The prominence of jets supports the finding that the power for jets can be extracted more easily from thick disks than from standard thin disks (c.f., Meier et al. 2001). The non-detection of a relativistic iron line in low hard state objects further supports the idea of a truncated disk. The spectral energy density is often fitted only with the accretion flow (the weak thermal emission) and the corona (the power law component, see e.g., Shapiro et al. 1976), if one excludes the radio emission. But the spectra of these objects can also be described by jet models (Falcke & Biermann 1999; Markoff et al. 2001a). As the accretion flow is radiatively inefficient for the inner radii it may be that the jet emission can even dominate the total radiated power (Fender et al. 2003).

AGN on the other hand are classified into a zoo of different types of sources. For radio-loud sub-classes the jet emission plays an important role in the models. Jet emission is intrinsically broad band, reaching from radio up to γ -rays (see e.g., von Montigny et al. 1995). Its SED has two components (see Fig. 1.5), at lower photon energies the emission is thought to be synchrotron emission from a population of relativistic particles, while the X-rays and γ -rays

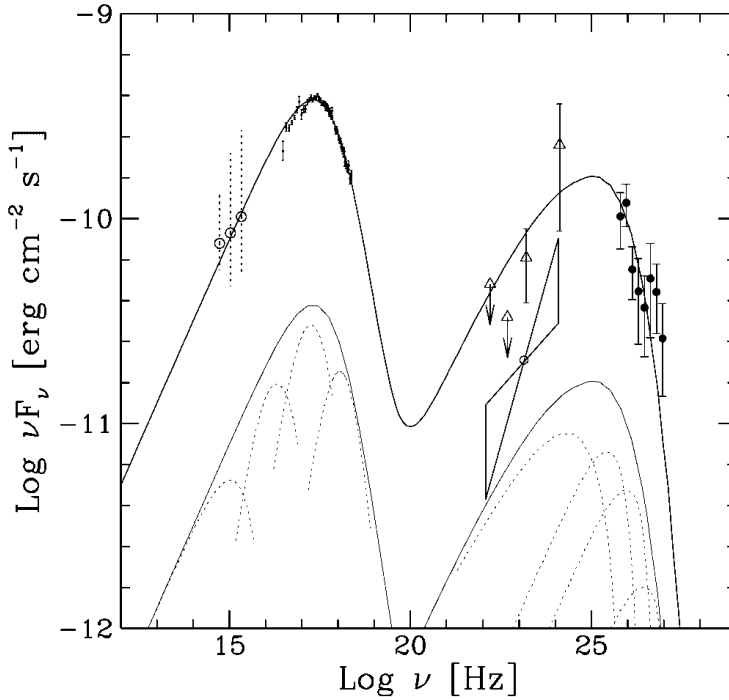


FIGURE 1.5— In Mkn 421 the effect of synchrotron and inverse Compton emission is clearly visible. While the first ‘bump’ at lower frequencies is created by synchrotron the second can be explained by inverse Compton scattering (reproduced from Maraschi et al. 1999).

may originate from inverse Compton processes (see e.g., Gursky & Schwartz 1977; Fossati et al. 1998). For weakly accreting AGN (e.g., low-luminosity AGN, FR I radio galaxies (Fanaroff & Riley 1974), BL Lac objects) the jet emission can dominate the total power of the AGN. Some AGN can also be classified as ‘high state’ objects - objects whose SED is dominated by a thermal component in the optical wavelengths (e.g., Seyferts, quasars, FR II radio galaxies). As for XRBs the standard disk probably reaches to the innermost stable orbits. In some of these strong accreting AGN one also observes a relativistic iron line (Fabian et al. 2000). However, some AGN that show many characteristics of the high state have powerful jets (FR II radio galaxies). The reason for this discrepancy with high-state XRBs is still unknown.

Previously, the two classes of black holes (supermassive and stellar) have been treated separately. We have argued above, that we need to unify both

types to gain a better understanding of the physics of accretion and jet ejection. Recently some connections have been found. For the high-state objects, McHardy et al. (2004) showed that the power spectral density (PSD) of the X-ray noise shows similar features in a narrow line Seyfert 1 galaxy as in X-ray binaries in the high-state. Abramowicz et al. (2004) suggested that quasi-periodic oscillations in the X-ray variability could also be used to connect XRBs to other black holes. Both ideas are mainly empirical and theoretical studies are needed.

1.2 Scope of the Thesis

In this thesis we explore the effect of jets in XRBs and AGN and search for connections between both classes of objects. The idea of jet-domination of the SED will be used to unify weakly accreting XRBs and AGN. The developed analytical jet model correctly predicts the correlation between radio and X-ray emission. This finding further strengthens the idea of X-rays originating from jets also in XRBs, and other implications of the jet model are tested. By analogy with the blazar phenomenon, which are AGN with their relativistic jet pointing towards the observer, there should be microblazars. This idea will be used to explain some of the recently-detected ultra-luminous X-ray sources (ULXs). Up to now these sources are - unlike blazars - mostly detected in the X-rays. We have therefore monitored a well defined sample of ULXs to search for radio emission. Finally we will explore whether the observed X-ray variability is in agreement with the jet picture.

In chapter 2 we develop the jet model, it forms the basis for the subsequent studies. In chapter 3 it will be used to argue for a unification scheme for AGN and XRBs. Chapter 4 and 5 covers the ULX phenomenon, and chapter 6 tests the jet picture for the short time variability of XRBs.

2

Jet Scaling

2.1 Introduction

In this chapter we derive an analytical model for relativistic jets. Using conservation laws we are able to predict the emission properties of jets and their scaling for changes in accretion rate and black hole mass.

The creation mechanism for relativistic jets and their connection to accretion processes is not fully understood. It is generally believed that relativistic magneto-hydrodynamic (MHD) processes are responsible for the jet launching (c.f., Meier et al. 2001). However, analytical solutions for realistic cases are usually impossible and even simulations on super-computers have severe limitations. Here we use the approach that the accretion and ejection processes are connected via a "black box", perhaps MHD, which is described by a parameter connecting accretion power and the power of the jet. This parameter will probably depend on the spin of the black hole (the 'spin-paradigm' c.f., Blandford et al. 1990 and ref. therein) or whether the accretion disk is geometrically thin or thick. This chapter is based on the ideas outlined in Falcke & Biermann (1995). Here the parameterization is different as the present work is more focused on the scaling of jets. We also improve the prior work by using exact formulas for the enthalpy and a detailed discussion of inverse-Compton emission.

The jet will be described by relativistic hydrodynamics. The jet plasma can either be a normal electron-proton plasma, an electron-positron plasma in the case that pair creation plays a significant role, or a mixture of both. Besides the thermal plasma we include a population of highly relativistic particles. This

population is included as we observe their synchrotron and inverse Compton radiation in the radio regime as well as in the optical and even γ -rays (see e.g., Begelman et al. 1984; Stievelli et al. 1991; von Montigny et al. 1995).

The ingredients of the jet model are:

- The jet is described in the hydrodynamic approximation, magnetic fields only enter in the enthalpy. This model is therefore unable to yield the jet launching or create the initial confinement.
- The jet plasma is assumed to be a perfect gas with a constant adiabatic index. This assumption is valid for a mixture of non-relativistic thermal and ultra-relativistic particles. For slightly relativistic particles the adiabatic index will vary from $\frac{5}{3}$ to $\frac{4}{3}$ (see e.g., Taub 1948).
- We allow no lateral structure of the jet. For simplicity the jet is assumed to be homogeneous up to its radius R_j . We usually describe the jet using cylindrical coordinates.
- We use a fixed geometry for the jet. The jet is accelerated and confined into a nozzle, behind this nozzle the jet will expand described by the function $R_j(z)$, e.g. it could expand freely (Blandford & Königl (1979); Falcke & Biermann (1995) and references therein).
- The Lorentz factor of the jet is a fixed parameter.
- The internal energy contained in the different populations of particles is assumed to be in equipartition with the magnetic field within a constant factor. This factor can be used to also describe sources which are not in equipartition but where the internal particle energy is correlated with the magnetic field.

Using these assumptions we will derive the relativistic plasma properties in section two. In section three we present the synchrotron and Compton emission of jet and give their scaling laws in the fourth section. This chapter is the basis of the following chapters where the ideas developed here will be tested and applied to black holes across the Universe.

2.2 Relativistic Hydrodynamics

In this section we present the hydrodynamic and thermodynamic concepts needed for the subsequent jet theory. It follows the presentation given in Königl

(1980), which we briefly summarize. For a detailed study the reader is referred to the original paper.

All thermodynamic quantities given here denote the values measured in the local rest-frame. We denote the rest-frame particle density as n , the average mass per particle as m , the temperature as T , the internal energy density as e , and the total mass-energy density of the fluid is $\rho = mnc^2 + e$. The adiabatic index Γ is defined as

$$\Gamma = \left. \frac{\partial \ln P}{\partial \ln n} \right|_S, \quad (2.1)$$

where P represents the pressure and the subscript S denotes that the entropy is fixed. The first law of thermodynamics can be written as

$$d\rho = \frac{\omega}{n}dn + nTdS, \quad (2.2)$$

where ω denotes the enthalpy defined as $\omega = \rho + P$. Combined with the definition of the adiabatic index the equation can be used to derive the sound speed, defined as

$$\beta_s \equiv \sqrt{\left. \frac{\partial P}{\partial \rho} \right|_S} = \sqrt{\frac{\Gamma P}{\omega}}. \quad (2.3)$$

The proper Mach number is defined as

$$\mathcal{M} = \frac{\gamma\beta}{\gamma_s\beta_s}, \quad (2.4)$$

where γ denotes the Lorentz factor of the fluid in the observer-frame, β the velocity of the fluid divided by the speed of light, and γ_s the Lorentz factor of the sound speed (β_s). It can be shown that disturbances in the supersonic relativistic flow can only propagate downstream in a cone with a half-opening angle of $1/\mathcal{M}$. This is the same result as in the Newtonian case, only the normal Mach number has to be exchanged with the proper Mach number. Thus, the freely expanding jet will have a half-opening angle of $1/\mathcal{M}$. Strong magnetic fields or angular momentum will change this scenario.

The stress-energy tensor for ideal fluids can be used to derive that an isentropic ($S = \text{const}$) flow follows the relativistic Bernoulli equation

$$\frac{\gamma\omega}{n} = \left. \frac{\omega}{n} \right|_0 = \text{const}. \quad (2.5)$$

The right hand side of this equation has to be evaluated at the stagnation point

($\beta = 0$).

We generally assume that the fluid can be described as a perfect gas ($P = nkT$, k is the Boltzmann constant) and that the adiabatic index Γ is constant. The latter assumption is only valid in the nonrelativistic and ultra-relativistic regime. In between Γ decreases slightly with increasing particle temperature. The adiabatic index has to be in the range $\frac{4}{3} \leq \Gamma \leq \frac{5}{3}$ (Taub 1948). However, the assumption remains valid for a mixture of an ultra-relativistic and a nonrelativistic population, e.g., a mixture of thermal protons and relativistic electrons. In this case the adiabatic index is $\Gamma = (4 - \frac{3}{2}r)/(3 - \frac{3}{2}r)$, where r denotes the number ratio of the two populations.

For such a perfect gas with a constant Γ and $P = (\Gamma - 1)e$ we can express the enthalpy as:

$$\omega = m_p n c^2 + \frac{\Gamma P}{\Gamma - 1}. \quad (2.6)$$

If the fluid is magnetized we have to include the magnetic energy density and pressure in the enthalpy. The magnetic pressure of an ordered magnetic field is

$$P_M = \frac{B^2}{8\pi}. \quad (2.7)$$

However, the magnetic field also creates a magnetic tension along the field lines (see c.f., Jackson 1975). In a turbulent field the magnetic pressure will therefore be reduced to

$$P_{Mturb} = \frac{1}{3} \frac{B^2}{8\pi}. \quad (2.8)$$

We can include the magnetic fields in our description by adding this pressure to the enthalpy (eq. 2.6) with an adiabatic index $\Gamma = 4/3$.

2.3 The Jet-Disk Connection

In this section we use the relativistic Bernoulli equation to derive the evolution of the relativistic plasma along the jet. Using equipartition we can calculate the number of relativistic particles and the strength of the magnetic fields. These properties will be used in the subsequent sections to derive the jet emission.

2.3.1 Enthalpy and Internal Energy of the Jet

The relativistic Bernoulli equation (2.5) describes the enthalpy along the jet, once we know the initial condition at the base of the jet. The enthalpy per particle $\frac{\omega}{n}|_0$ at the base of the jet depends on the accretion model. For example

there could be a split between matter with low enthalpy accreting into the black hole and matter ejected in the jet. As there are many open questions in the formation of the jet we will simply parameterize the enthalpy and the matter transferred into the jet. The matter injected into one jet \dot{M}_j is assumed to be a fraction q_m of the total accretion rate. Similarly we will assume that the enthalpy injected into the jet is a fraction q_e of the total accretion power $\dot{M}c^2$. Thus, we have the initial condition

$$\left. \frac{\omega}{n} \right|_0 = \frac{q_e \dot{M} c^2 m_p}{q_m \dot{M}} = \frac{q_e m c^2}{q_m}, \quad (2.9)$$

where m denotes the average particle mass. In the absence of significant pair production (e.g., electron-positron plasma) it will be dominated by the proton mass.

If we assume that the radial structure of the jet with a Lorentz factor of γ_j is homogeneous up to the jet radius R_j we can derive the particle density n

$$n = \frac{q_m \dot{M}}{\gamma_j \beta_j c m \pi R_j^2}. \quad (2.10)$$

Thus, the relativistic Bernoulli equation (2.5) allows us to derive the enthalpy in the jet at any distance from the black hole:

$$\omega = \frac{q_e \dot{M} c}{\gamma_j^2 \beta_j \pi R_j^2} \quad (2.11)$$

On the other hand, we know from section 2.2 that

$$\omega = n m c^2 + \frac{\Gamma P}{\Gamma - 1} = n m c^2 + \Gamma U_j, \quad (2.12)$$

where U_j denotes the internal energy density, in which we are interested. Using our formula for n we find

$$\Gamma U_j = \omega - n m c^2 = \frac{\dot{M} c}{\gamma_j^2 \beta_j \pi R_j^2} (q_e - \gamma_j q_m), \quad (2.13)$$

and define the reduced coupling factor $\hat{q}_e = (q_e - \gamma_j q_m)$.

As mentioned in the introduction the internal energy is assumed to have three parts: the energy of the magnetic field, the energy of the relativistic par-

ticles, and the turbulent kinetic energy of the nonrelativistic particles,

$$U_j = U_{\text{turb}} + U_B + U_{\text{rel}}. \quad (2.14)$$

We will assume that the different energy densities are correlated with each other. This connection will be established automatically if there is a mechanism, e.g. shocks, that can transfer one type of energy into an other. If these energy densities are in equipartition all three will be roughly the same. To include the non-equipartition case as well we define 'equipartition parameters'

$$k_{\text{rel}} = \frac{U_{\text{rel}}}{U_B}, \quad k_{\text{turb}} = \frac{U_{\text{turb}}}{U_B}, \quad \text{and} \quad k_{\text{eq}} = 1 + k_{\text{rel}} + k_{\text{turb}}, \quad (2.15)$$

that describe how strong the jet deviates from equipartition. Therefore we can write the enthalpy as

$$\omega - nmc^2 = \Gamma (U_{\text{turb}} + U_B + U_{\text{rel}}) = k_{\text{eq}} \Gamma U_B. \quad (2.16)$$

This parameterization allows to solve eq. (2.13) for the magnetic field:

$$B = \sqrt{\frac{8\pi\hat{q}_e\dot{M}c}{\Gamma\gamma_j^2\beta_j\pi R_j^2 k_{\text{eq}}}}. \quad (2.17)$$

Using the parameterization described above we can also derive the sound speed

$$\beta_s = \sqrt{\frac{\Gamma P}{\omega}} = \sqrt{\frac{\hat{q}_e}{q_e} (\Gamma - 1)} = \sqrt{\Gamma - 1} \sqrt{1 - \gamma_j \frac{q_m}{q_e}}. \quad (2.18)$$

The maximal possible sound speed is therefore $\beta_s = \sqrt{\Gamma - 1}$. However, this maximal sound speed will only be reached if the total power injected into the jet is much higher than the power stored in the rest mass and their bulk motion ($q_e \dot{M} c^2 \gg q_m \gamma_j \dot{M} c^2$). In this case the kinetic energy of the matter inside the jet is comparable with the rest mass itself and the gas becomes 'photon-like' and the sound speed in the jet reaches the sound speed of a photon gas.

2.3.2 Relativistic Particles

From the assumption that the total energy of the relativistic particles is connected with the magnetic field we can derive the relativistic particle density. In optically thin radio jets one usually observes a power law in the spectrum. This

power law is interpreted as synchrotron emission, which is created by power-law distributed relativistic electrons. Such a distribution also arises from shock acceleration theory (see e.g., Begelman & Kirk 1990). Thus, we assume that the relativistic electrons and protons are distributed as

$$dN_{\text{elp}} = \mathcal{N}_{\text{elp},0} \gamma_{\text{elp}}^{-p} d\gamma_{\text{elp}}, \quad (2.19)$$

where γ_{elp} denotes the Lorentz factor of the electrons or protons in contrast to the bulk Lorentz factor of the jet γ_j . The power law index of the relativistic particles is denoted by a lower case p . In principle the power law indices for electron/positron and protons could be different. We will usually only use the value for the electrons, the proton contribution will be absorbed into the relativistic electron/proton ratio. With the parameters defined in eq. (2.15) we find:

$$k_{\text{rel}} \frac{B^2}{8\pi} = \mathcal{N}_{\text{e},0} \int_{\gamma_{\text{min,e}}}^{\gamma_{\text{max,e}}} \gamma m_{\text{e}} c^2 \gamma^{-p} d\gamma + \mathcal{N}_{\text{p},0} \int_{\gamma_{\text{min,p}}}^{\gamma_{\text{max,p}}} \gamma m_{\text{p}} c^2 \gamma^{-p} d\gamma. \quad (2.20)$$

The integrals can be solved analytically, and name their solutions

$$\Lambda_{\text{elp}} = \begin{cases} \left(\gamma_{\text{min,elp}}^{2-p} - \gamma_{\text{max,elp}}^{2-p} \right) / (p-2) & \text{for } p \neq 2, \\ \ln \frac{\gamma_{\text{max,elp}}}{\gamma_{\text{min,elp}}} & \end{cases}. \quad (2.21)$$

Only the electrons are visible in synchrotron radiation in almost every case (but see Aharonian 2002), we therefore describe the relativistic particles with the electron density, and connect the protons to this quantity. The relativistic electron/proton ratio is defined as

$$\mu_{\text{e/p}} = 1 + \frac{\mathcal{N}_{\text{p},0} \Lambda_{\text{p}} m_{\text{p}}}{\mathcal{N}_{\text{e},0} \Lambda_{\text{e}} m_{\text{e}}}, \quad (2.22)$$

and the fudge-factor f as

$$f = \frac{\Lambda_{\text{e}} \mu_{\text{e/p}}}{k_{\text{rel}}}. \quad (2.23)$$

With these parameters we find for the normalization factor $\mathcal{N}_{\text{e},0}$ of the power-law distribution

$$\mathcal{N}_{\text{e},0} = \frac{B^2}{8\pi f m_{\text{e}} c^2}. \quad (2.24)$$

We can use this distribution together with the magnetic field strength to derive the jet emission.

2.3.3 The Parameters

Observable parameters needed to fix the setting

The following parameters describe the central engine and its jet. They are in principle measurable.

- M denotes the mass of the central black hole. For XRBs the mass will only be a few solar masses, while AGN masses go up to a few times $10^9 M_\odot$.
- \dot{M} is the accretion rate. It describes the total mass/energy rate brought into the central engine.
- γ_j gives the Lorentz factor of the jet. For many XRBs the Lorentz factor is not well constrained (Fender et al. 1999), usually lower values than for AGN are given, including the range $\gamma_j = 2-5$. In some blazars these values can go up to 25 (see e.g., Ghisellini et al. 1993). The Lorentz factor can either be deduced from the spectral energy distribution or measured directly via VLBI (c.f., Cohen et al. 1977; Kellermann et al. 2004).
- p is the power-law index of the electron distribution. As we will see in the section 2.4 p can be deduced from the measured power-law index of the optically thin part of the spectrum. Values around $p \approx 2-3$ correspond to the observed spectral power laws and can be created using particle acceleration in relativistic shocks (see e.g., Blandford & Rees 1974).

Parameters intrinsic to the model

As we do not derive the connection between the disk and the jet from first principles we have to parameterize this 'black box'.

- q_e denotes the fraction of energy inserted into the enthalpy at the base of the jet. Energy conservation limits this value to $q_e \leq 1$. This maximal value cannot be reached as an accretion flow is needed to power the relativistic jet. A fraction of a few percent seems reasonable and is needed to produce the observed luminosities.

- q_m gives the fraction of mass ejected in the jet. Mass conservation limits $q_m \leq 1$ as long as pair creation is negligible. We will consider values around $q_m \lesssim 0.01$.
- $\hat{q}_e = q_e - \gamma_j q_m$ is the reduced enthalpy parameter, it corresponds to the magnetic energy density in the jet. This combined parameter will, with the above choices for q_m and q_e , be of the order of $\hat{q}_e \approx 0.01$.
- k_{eq} gives the fraction of the non rest-mass related enthalpy to the magnetic field energy. The ratio of the energy in relativistic particles and of the turbulent plasma compared with the magnetic field energy is given by k_{rel} and k_{turb} respectively. For total equipartition these latter parameters will be one while $k_{\text{eq}} = 3$. If the magnetic field dominates the overall internal energy k_{rel} and k_{turb} will get small. Theory of shock acceleration utilizes magnetic fields (see e.g., Jokipii 1987). Thus, the energy in the relativistic particles will probably not exceed the magnetic energy density ($k_{\text{rel}} \leq 1$).
- $f = \Lambda_e \mu_{p/e} / k_{\text{rel}}$ is the fudge-factor. It combines the equipartition parameter k_{rel} with the relativistic electron/proton ratio $\mu_{p/e}$ and the integral factor Λ_e . For $p = 2$, Λ_e depends logarithmically on the ratio of the maximal and minimal lorentz factor of the relativistic particles. As we usually explore the case that p is around two, this parameter will only vary little. $\mu_{p/e}$ will be unity if there are no relativistic protons, it will increase with the proton fraction. The fudge-factor therefore has a lower bound around 4 and can get very large if the jet is not in equipartition.
- R_{acc} is the jet radius where the first relativistic particles are accelerated. It corresponds directly to the distance from the black hole Z where the particle acceleration starts, once a jet geometry is given. A typical value is around 10 Schwarzschild radii. Such a value is often found in fits to spectra (see e.g., Markoff et al. 2001a). This radius also gives a lower limit for the size of the emitting region, which could be measured using VLBI. For the Galactic Center the size has been measured recently by Bower et al. (2004) to be as small as 27 Schwarzschild radii, for earlier work see e.g., Krichbaum et al. (1998). For M87 Junor et al. (1999) give an upper limit of $30 R_G$ at a observing frequency of 43 GHz.

2.4 Emission from the Jet

In section 2.3 we have derived the magnetic field (eq. 2.17) and the relativistic electron density (eq. 2.24). With these quantities and the jet geometry we can calculate the synchrotron and inverse-Compton emission from the jet. In this section we give the analytical solutions and in the next section we present the emission formulae in numbers scaled for a black hole XRB.

The jet is usually thought to be accelerated and collimated in a nozzle and it will expand beyond this nozzle (see Fig. 2.1). A freely expanding jet will have a conical shape with an opening angle given by the relativistic Mach number $1/\mathcal{M}$. Here we will allow for slightly more general geometries and denote the jet radius depending on the distance from the black hole Z as the function $R_j(Z)$. As we are interested in an analytical solution we will only consider power-law dependencies, e.g.,

$$R_j(z) = \xi_1 z^{\xi_2}. \quad (2.25)$$

However, these simple geometries will already explain the existence of flat and inverted radio cores. More general solutions would require a numerical treatment. For the free jet the opening angle in the rest frame of the black hole is $1/\mathcal{M}$, and we find: $\xi_1 = \gamma_j/\mathcal{M}$ and $\xi_2 = 1$.

2.4.1 Synchrotron Emission

The synchrotron emissivity of power-law distributed electrons is given for example in Shu (1991); Rybicki & Lightman (1979):

$$\epsilon_\nu = \frac{\sqrt{3}N_{e,0}e^3}{(p+1)m_e c^2} (B \sin \alpha)^{\frac{p+1}{2}} \left(\frac{2\pi m_e c \nu}{3e}\right)^{-\frac{p-1}{2}} \Gamma\left(\frac{p}{4} + \frac{19}{12}\right) \Gamma\left(\frac{p}{4} - \frac{1}{12}\right), \quad (2.26)$$

and the absorption coefficient is given as

$$\kappa_\nu = \frac{N_{e,0}c e^2}{4\sqrt{3}m_e c^2} \left(\frac{3e}{2\pi m_e c}\right)^{\frac{p+2}{2}} \Gamma\left(\frac{3p+2}{12}\right) \Gamma\left(\frac{3p+22}{12}\right) (B \sin \alpha)^{\frac{p+2}{2}} \nu^{-\frac{p+4}{2}}. \quad (2.27)$$

For our jet model we can use eq. (2.24) to eliminate $\mathcal{N}_{e,0}$. For convenience we combine all constant parameters into a new constant C_ϵ :

$$\begin{aligned} \epsilon_\nu &= C_\epsilon B^{\frac{p+5}{2}} \nu^{-\frac{p-1}{2}} \\ \text{with } C_\epsilon &= \frac{\sqrt{3}e^3 (\sin \alpha)^{\frac{p+1}{2}}}{8\pi f(p+1)(m_e c^2)^2} \left(\frac{2\pi m_e c}{3e}\right)^{-\frac{p-1}{2}} \Gamma\left(\frac{p}{4} + \frac{19}{12}\right) \Gamma\left(\frac{p}{4} - \frac{1}{12}\right). \end{aligned} \quad (2.28)$$

The absorption coefficient yields:

$$\begin{aligned} \kappa_\nu &= C_\kappa B^{\frac{p+6}{2}} \nu^{-\frac{p+4}{2}} \\ \text{with } C_\kappa &= \frac{ce^2 (\sin \alpha)^{\frac{p+2}{2}}}{32\pi f \sqrt{3} (m_e c^2)^2} \left(\frac{3e}{2\pi m_e c}\right)^{\frac{p+2}{2}} \Gamma\left(\frac{3p+2}{12}\right) \Gamma\left(\frac{3p+22}{12}\right). \end{aligned} \quad (2.29)$$

The emissivity and the absorption coefficient above is given in the rest frame of the fluid. In the rest frame of the observer this jet is moving relativistically with a Lorentz factor γ_j . To derive the emission in the observers frame we utilize, that ϵ_ν/ν^2 and the optical depth τ are Lorentz invariants (Rybicki & Lightman 1979). The Doppler factor \mathcal{D} is defined as

$$\mathcal{D} = \frac{1}{\gamma_j(1 - \beta_j \cos i_{\text{obs}})}, \quad (2.30)$$

where the subscript $_{\text{obs}}$ denotes that a quantity is measured in the observers frame. The relativistic Doppler effect relates the emitted photon frequency in the comoving frame with the observed value:

$$\nu_{\text{com}} = \frac{\nu_{\text{obs}}}{\mathcal{D}}. \quad (2.31)$$

It follows from the fact that ϵ_ν/ν^2 is a Lorentz invariant that the emissivity in the observers frame will be:

$$\epsilon_{\nu,\text{obs}}(\nu_{\text{obs}}) = \mathcal{D}^2 \epsilon_{\nu,\text{com}}(\nu_{\text{obs}}/\mathcal{D}) \quad (2.32)$$

To derive the optical depth we also need to know the Lorentz transformation of the inclination angle of the jet:

$$\sin i = \mathcal{D} \sin i_{\text{obs}}. \quad (2.33)$$

Under the assumption of a conical jet we find, that the Lorentz invariant optical depth τ is in the comoving frame $\tau \approx 2R_j\kappa/\sin i$ (cylindrical jet approximation), where i denotes the inclination angle of the jet to the line of sight. The jet gets optically thin around $\tau = 1$:

$$1 = \frac{2\kappa R_{j,SSA}}{\sin i}. \quad (2.34)$$

If we assume that the jet has a constant speed in the area of interest, we can rewrite the magnetic field (2.17) as

$$B = B_0 \frac{1}{R_j}. \quad (2.35)$$

Using this definition we can solve the equation for the $\tau = 1$ surface for the jet radius $R_{j,SSA}$ where the jets get synchrotron self-absorbed.

$$R_{j,SSA} = \left(\frac{2B_0^{\frac{p+6}{2}} C_\kappa}{\sin i} \right)^{\frac{2}{p+4}} \nu^{-1} \quad (2.36)$$

For the observers frame, this can be written as:

$$R_{j,SSA} = \left(\frac{2B_0^{\frac{p+6}{2}} C_\kappa}{\mathcal{D} \sin i_{\text{obs}}} \right)^{\frac{2}{p+4}} \left(\frac{\nu_{\text{obs}}}{\mathcal{D}} \right)^{-1} \quad (2.37)$$

Thus, the jet emission in the observers-frame can be approximated by

$$\begin{aligned} L_{\nu,\text{obs}} &\approx \mathcal{D}^2 \int_{Z_{SSA}}^{\infty} \epsilon_{\nu,\text{obs}} \pi R_j^2 dz \\ &\approx \pi \mathcal{D}^2 C_\epsilon \left(\frac{\nu_{\text{obs}}}{\mathcal{D}} \right)^{-\frac{p-1}{2}} B_0^{\frac{p+5}{2}} \int_{R_{j,SSA}}^{\infty} R_j^{-\frac{p+1}{2}} \frac{dz}{dR_j}, \end{aligned} \quad (2.38)$$

as long as the base of the jet is optically thick for the observing frequency. Using the jet geometry described in eq. (2.25) we can solve the integral ana-

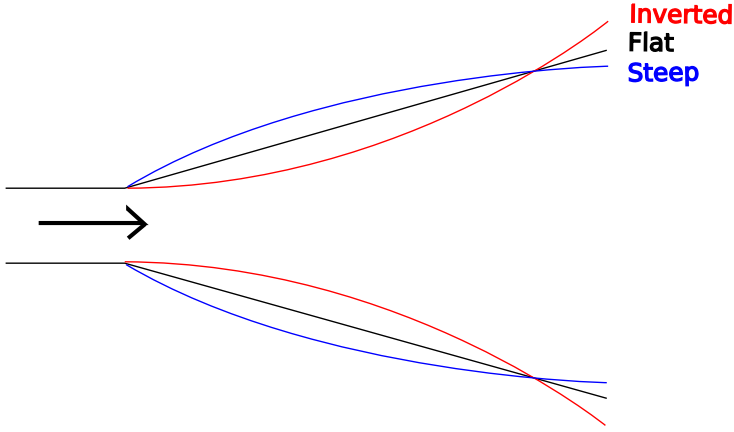


FIGURE 2.1— Sketch of the different jet geometries

lytically

$$L_{\nu, \text{obs}} = \frac{\pi \mathcal{D}^2 C_\epsilon B_0^{\frac{p+5}{2}} \xi_2^{-1} \xi_1^{-\frac{1}{\xi_2}} \left(\frac{\nu_{\text{obs}}}{\mathcal{D}}\right)^{1-\frac{1}{\xi_2}}}{\frac{p+1}{2} - \frac{1}{\xi_2}} \left[\left(\frac{2C_K}{\mathcal{D} \sin i_{\text{obs}}}\right)^{\frac{2}{p+4}} B_0^{\frac{p+6}{p+4}} \right]^{-\frac{p-1}{2} + \frac{1}{\xi_2} - 1}. \quad (2.39)$$

Under the assumption that the jet Lorentz factor is constant, the emission from the central part of the jet can either have a flat spectrum, inverted spectrum or steep spectrum depending on the jet geometry (see Fig. 2.1):

1. $\xi_2 = 0$: The freely expanding jet with $R_j = \frac{1}{\mathcal{M}}z$ or a similar linear expansion leads to a flat spectrum of the central core.
2. $\xi_2 > 0$ leads to an inverted spectrum. For high values of ξ_2 this can yield a spectral index of up to unity. It may well be, that in the central part of the jet, where the energy is magnetically dominated, such a confined, slower expanding than the freely expanding jet, jet can be found.
3. $\xi_2 < 0$ would lead to a steep spectrum. However, such a steep spectrum is normally not found in the core of an AGN or an XRB.

As we have seen the jet geometry can change the flat spectrum to an inverted spectrum. A similar effect can be obtained if the jet accelerates. We have seen in eq. (2.17) that $B \sim \sqrt{q_e}/(R_j \gamma_j)$. If γ_j changes with the distance

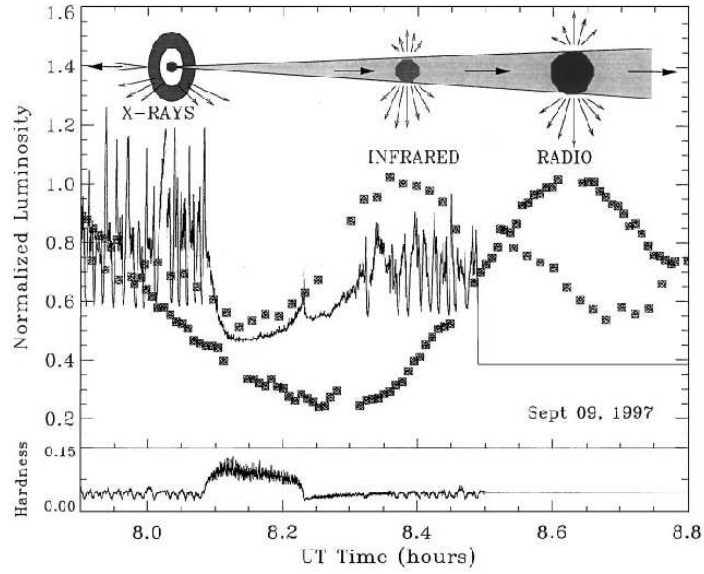


FIGURE 2.2— GRS 1915 in the Radio/Optical/X-rays, this plot has been reproduced from Mirabel & Rodríguez (1999)

from the black hole Z , \hat{q}_e will also depend on Z . Thus, an analytical treatment is hard to achieve. Qualitatively an increasing Lorentz factor with Z , will lead to the same situation as case 2 above: an inverted spectrum. This has already been noted by Falcke (1996).

The flat or inverted spectrum therefore arises from the superposition of self-absorbed synchrotron spectra originating from different positions in the jet. Higher frequency emission comes from a region nearer to the central black hole. This effect can be directly observed in GRS 1915 (Mirabel & Rodríguez 1999). In Fig. 2.2 we show an ejection of a jet component probably indicated by the small X-ray spike during the X-ray dip. The disturbance of the jet travels outwards and is seen in the optical and afterwards in radio frequencies.

In the case that the point in the jet, where the shock acceleration starts, becomes optically thin for the observing frequencies, the jet emission is given by:

$$L_\nu = \frac{\pi D^2 C \epsilon B_0^{\frac{p+5}{2}} \xi_2^{-1} \xi_1^{-\frac{1}{\xi_2}} \left(\frac{\nu_{\text{obs}}}{D}\right)^{-\frac{p-1}{2}+1-\frac{1}{\xi_2}} R_{\text{acc}}^{-\frac{p-1}{2}+\frac{1}{\xi_2}-1}}{\frac{p+1}{2} - \frac{1}{\xi_2}}, \quad (2.40)$$

where R_{acc} is the jet radius at the distance from the black hole where the particle acceleration starts. The transition frequency between the flat spectrum part and steep spectrum can be derived from eq. (2.37):

$$\nu_{\text{SSA,obs}} = \mathcal{D} R_{\text{acc}}^{-1} \left(\frac{2B_0^{\frac{p+6}{2}} C_\kappa}{\mathcal{D} \sin i_{\text{obs}}} \right)^{\frac{2}{p+4}}. \quad (2.41)$$

The synchrotron emission from a jet will therefore have a flat or slightly inverted spectrum for frequencies below the transition frequency. Above this transition we observe the optical thin synchrotron power law coming from the base of the jet.

Emission from the Nozzle

In some cases the electron acceleration may start already in the collimation phase of the jet, e.g., some emission may originate from a non-expanding part of the jet. The spectrum of the nozzle can be modeled by the emission from a plasma blob with the same parameters as the base of the jet. This will add a self-absorbed synchrotron feature to the overall jet emission.

2.4.2 Compton Emission

The population of relativistic particles will not only create synchrotron emission, but they will also scatter with photons leading to Compton emission. Thus, jet emission always consists of a mixture of the different emission types. Here we will only consider photons in the Thomson limit, e.g., where Klein-Nishima effects are negligible ($\epsilon_{\text{PH}} \ll m_e c^2$). For the current X-ray satellites Chandra and XMM-Newton this is a good approximation. For electrons distributed in a power law the inverse-Compton emissivity is given in Rybicki & Lightman (1979) or Shu (1991):

$$\epsilon_{\text{IC}}(\epsilon_1) = c\pi \frac{e^4}{m_e^2 c^4} \mathcal{N}_{e,0} A(p) \epsilon_1^{-\frac{p-1}{2}} \int \epsilon^{\frac{p-1}{2}} \nu(\epsilon) d\epsilon, \quad (2.42)$$

where $\nu(\epsilon)$ is the photon density per energy and volume, and $A(p)$ is defined as:

$$A(p) = 2^{p+3} \frac{p^2 + 4p + 11}{(p+3)^2 (p+5)(p+1)}. \quad (2.43)$$

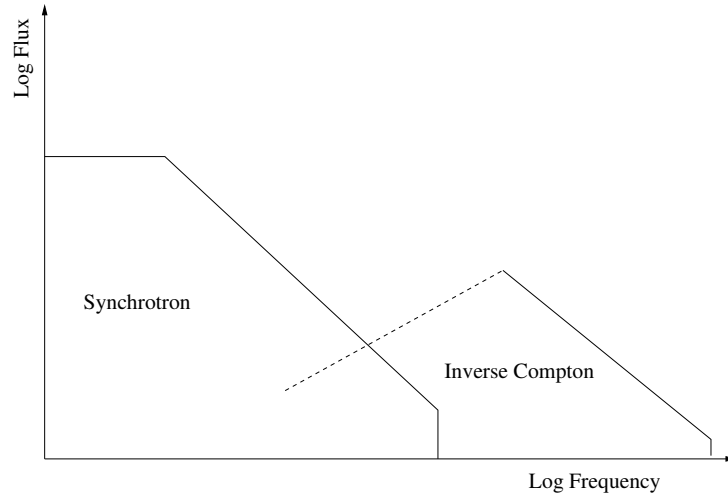


FIGURE 2.3— Sketch of the SED of a jet: synchrotron and inverse-Compton emission

The spectral power-law has the boundaries

$$4\gamma_{\min,e}^2 \bar{\epsilon} \leq \epsilon \leq 4\gamma_{\max,e}^2 \bar{\epsilon}, \quad (2.44)$$

where $\bar{\epsilon}$ denotes the mean seed photon energy. A schematic picture of the resulting spectral energy distribution is shown in Fig. 2.3. We will consider the cases where the seed photons originate from the synchrotron emission in the jet itself and from the accretion disk.

Synchrotron self-Compton emission

For the synchrotron self-Compton emission (SSC) the seed photons are created by synchrotron radiation. We can approximately derive the seed photon density from the synchrotron emissivity. Near the center of the jet, the photon density is slightly higher than $\nu(\epsilon) = \epsilon_{\text{sync}} R_j / (c\epsilon)$. Near the boundaries of the jet this density will be a bit less, but as the photon density only enters linearly in the SSC formula a small error will not have large impacts. The energy density of the photon field will be dominated by the optical thin power law part of the synchrotron spectrum. Thus, we will not consider optical depth effects here. For simplicity we will only consider the case of a freely expanding jet here. With these approximations we find for the SSC emissivity in the comoving-

frame

$$\epsilon_{\text{SSC}}(\epsilon_1) = c \frac{e^4}{8fm_e^3c^6} A(p) C_\epsilon \frac{R_j}{c} \epsilon_1^{-\frac{p-1}{2}} B_0^{\frac{p+9}{2}} \ln\left(\frac{\epsilon_{\text{max}}}{\epsilon_{\text{min}}}\right). \quad (2.45)$$

Similar to the derivation of the synchrotron emissivity of the whole jet, the total SSC emission from the jet in the observer frame is the integral of the emissivity over the jet cone. The emissivity has to be transformed into the observers frame as before. We find for the SSC emission:

$$L_{\nu,\text{SSC}}(\epsilon_1) = \pi \mathcal{D}^2 \frac{e^4}{8fm_e^3c^6} A(p) C_\epsilon \left(\frac{\epsilon_{1,\text{obs}}}{\mathcal{D}}\right)^{-\frac{p-1}{2}} B_0^{\frac{p+9}{2}} \ln\left(\frac{\epsilon_{\text{max}}}{\epsilon_{\text{min}}}\right) \frac{R_{\text{acc}}^{-\frac{p+1}{2}} \mathcal{M}}{\frac{p+1}{2} \gamma_j}. \quad (2.46)$$

In order to compare the energy loss due to SSC emission with those of external-Compton later on we also derive the total photon energy density of synchrotron photons:

$$U_{\text{Ph,Sync}} \approx \int_{\nu_{\text{min}}}^{\nu_{\text{max}}} \epsilon_{\text{sync}}(\nu) \frac{R_j}{c} d\nu \approx C_\epsilon \frac{B_0^{\frac{7}{2}}}{2cR_j^{\frac{5}{2}}} \nu_{\text{max}}^{\frac{1}{2}} \quad (2.47)$$

External Compton

In the central region of the accreting black hole the accretion flow will also provide seed photons for Compton scattering. As described in eq. (2.42) the spectrum of the external-Compton emission (EC) will also be a power law with spectral index $\frac{p-1}{2}$. Thus, we will only derive the energy loss rate for the electrons and compare this to the energy loss due to synchrotron radiation. The energy loss of a relativistic electron in the radiation field of the accretion disk in the Thomson limit is given by Dermer & Schlickeiser (2002). It can be decomposed in two components: the near field and the far field. In the far field approximation only the photons moving approximately in the same direction as the jet are considered. The photon energy will be 'deboosted' and the energy loss declines with increasing jet Lorentz factor. Near the central black hole, the photons also have a tangential velocity component, which will be enhanced. This is considered in the near field approximation. The near field loss rate is

$$-\dot{\gamma}_{\text{NF,e}} = \frac{4}{3} \frac{\sigma_{\text{T}} c}{m_e c^2} \frac{0.7 L_{\text{disk}} R_{\text{G}}}{4\pi R^3 c} \gamma_j^2 \gamma_e^2, \quad (2.48)$$

and the far field loss rate is

$$-\dot{\gamma}_{\text{FF,e}} = \frac{4}{3} \frac{\sigma_{\text{T}} c}{m_e c^2} \frac{L_{\text{disk}}}{4\pi R^2 c} \frac{\gamma_e^2}{\gamma_j^2 (1 + \beta_j)^2}. \quad (2.49)$$

The transition radius where the far field energy loss starts to dominate is at

$$r_{\text{tr}} \approx 3\gamma_j^4 = 1875(\gamma_j/5)^4. \quad (2.50)$$

In the same notation the energy loss rate for synchrotron radiation is given by:

$$-\dot{\gamma}_{\text{Sync,e}} = \frac{4}{3} \frac{\sigma_{\text{T}} c}{m_e c^2} \gamma_e^2 U_B, \quad (2.51)$$

where U_B denotes the comoving energy density of the B field.

Near the black hole, the near field loss rate dominates the external-Compton losses. Whether these losses dominate over the synchrotron losses depends on the jet parameters:

$$\frac{\dot{\gamma}_{\text{Sync,e}}}{\dot{\gamma}_{\text{NF,e}}} = \frac{\hat{q}_e 4R^3}{\Gamma \gamma_j^4 R_j^2 k_{\text{eq}} 0.7\eta R_G}, \quad (2.52)$$

where η describes the efficiency of the accretion flow ($L_{\text{disk}} = \eta \dot{M} c^2$) and $R_G = \frac{GM}{c^2}$. The jet radius is perpendicular to the jet velocity vector, thus it does not have to be transformed. In the observers frame we have $R_j = R/\mathcal{M}$ and find:

$$\frac{\dot{\gamma}_{\text{Sync,e}}}{\dot{\gamma}_{\text{NF,e}}} = 0.017 \frac{(\hat{q}_e/0.01)z}{(\eta/0.1)(k_{\text{eq}}/3)(\gamma_j/5)^2}, \quad (2.53)$$

where we assumed that $\mathcal{M} = \frac{\gamma_j \beta_j}{\beta_s \gamma_s}$ with $\beta_s^2 = 1/3$. The distance z from the black hole is measured in gravitational radii ($z = Z/R_G$). For very small distances from the central black hole the EC losses will therefore dominate over the synchrotron losses. This effect will be even stronger, if the jet is not so well collimated. The EC radiation will dominate the synchrotron radiation up to a transition distance z_t of

$$z_t = 59 \frac{(\eta/0.1)(k_{\text{eq}}/3)(\gamma_j/5)^2}{(\hat{q}_e/0.01)}. \quad (2.54)$$

Thus, this effect will only play an important role for high disc efficiencies and low jet power. It may for example play a role in high state XRBs.

The far-field Compton losses can usually be neglected compared with synchrotron losses:

$$\frac{\dot{\gamma}_{\text{Sync,e}}}{\dot{\gamma}_{\text{FF,e}}} = 30 \frac{(\hat{q}_e/0.01)(\gamma_j/5)^2}{(\eta/0.1)(k_{\text{eq}}/3)} \quad (2.55)$$

However, if these losses dominate at one point of the jet, external-Compton emission would dominate the overall emission from the jet and would probably quench the whole jet.

Finally an external isotropic radiation field like the cosmic microwave background or radiation scattered by surrounding gas e.g., in the broad line region will induce radiation losses according to:

$$-\dot{\gamma}_{\text{T,iso}} = \frac{4c\sigma_{\text{T}}}{3m_e c^2} \gamma_e^2 \gamma_j^2 U_{\text{Ph,iso}} \left(1 + \frac{\beta_j^2}{3} \right) \quad (2.56)$$

As we are interested in the jet near the central black hole, the cosmic microwave background will not contribute significantly to the overall energy density in the jet. However, if there is a medium that reflects the radiation from the accretion disk and creates an isotropic radiation field, it will lead to significant inverse Compton losses. To quantify this effect we assume that a fraction α_{ref} of the emitted light will be scattered and forms an isotropic radiation field. If the reflecting material is uniformly distributed the resulting radiation field will still decline quadratic with distance to the central black hole:

$$U_{\text{Ph,iso}} = \alpha_{\text{ref}} 1.2 \times 10^{38} \frac{\eta}{0.1} \frac{\mathcal{VM}}{4\pi R^2 c} \quad (2.57)$$

And we find for the fraction of energy loss due to synchrotron radiation compared to this kind of inverse Compton losses:

$$\frac{\dot{\gamma}_{\text{Sync,e}}}{\dot{\gamma}_{\text{T,iso}}} = \frac{U_B}{\gamma_j^2 U_{\text{Ph,iso}} (4/3)} = 9 \times 10^{-3} \frac{(\hat{q}_e/0.01)}{\alpha_{\text{ref}} (\eta/0.1) (k_{\text{eq}}/3) (\gamma_j/5)^2} \quad (2.58)$$

Thus, if some of the emitted disk radiation is scattered into an isotropic radiation field, external Compton emission can dominate the synchrotron emission. The crucial parameters governing this effect are the disk efficiency η and the fraction of the isotropic radiation field α_{ref} .

2.4.3 High Energy Cut-off

Here we consider acceleration of the radiating electrons themselves. If these relativistic particles are accelerated in shocks in the jet we can equate the acceleration time scale with the cooling timescale to get the maximal Lorentz factor. However, this value could be greatly enhanced if the particle acceleration could be mediated via hydronic processes (see e.g., Mannheim et al. 1991). The acceleration timescale is given in Jokipii (1987):

$$t_{\text{acc}}^{-1} = \frac{3}{4} \beta_{\text{sh}}^2 \frac{eB}{m_e c \zeta \gamma_e}. \quad (2.59)$$

The main cooling mechanism will be synchrotron and inverse Compton radiation. Adiabatic cooling will not play an important role in the vicinity of the black hole. The synchrotron cooling timescale can be written as:

$$t_{\text{sync}}^{-1} = \frac{4}{3} \sigma_T \gamma_e \beta_e^2 \frac{U_B}{m_e c}. \quad (2.60)$$

As discussed above, the inverse Compton time scales are similar to synchrotron time scales, if one exchanges the energy density of the magnetic field with the energy density in the photon field

$$t_{\text{IC}}^{-1} = \frac{4}{3} \sigma_T \gamma_e \beta_e^2 \frac{U_{\text{Ph}}}{m_e c}. \quad (2.61)$$

For the maximal Lorentz factors the acceleration and cooling times are equal:

$$\gamma_{\text{max}}^2 = \frac{9}{16} \frac{\beta_{\text{sh}} e B}{\beta_e^2 \sigma_T (U_B + U_{\text{Ph}})}. \quad (2.62)$$

The maximum synchrotron frequency is

$$\nu_{\text{max}} = 0.29 \frac{3 \gamma_{\text{max}}^2 e B \sin \alpha}{4 \pi m_e c}, \quad (2.63)$$

so we find for the maximal Lorentz factor:

$$\nu_{\text{max}} = 0.29 \frac{27 \beta_{\text{sh}} e^2 U_B \sin \alpha}{8 m e c \zeta \sigma_T (U_B + U_{\text{Ph}})} = 1.0 \times 10^{20} \text{ Hz} \frac{U_B}{U_B + U_{\text{Ph}}} \zeta_2^{-1} \beta_{\text{sh}}^2. \quad (2.64)$$

where $\zeta = 100 \zeta_2$ and isotropic pitch angles $\alpha \approx 54^\circ$. For the case of $\beta_{\text{sh}} = \beta_s = \sqrt{1/3}$ and that synchrotron cooling dominates the losses the maximal

frequency corresponds to an high energy cutoff of $140keV/\zeta_2$ – independent of the magnetic field or the black hole mass. The independence on the black hole mass does not seem to be realized in nature, as in low-hard state XRBs one often observes a cutoff around 80 keV, but even for TeV-blazars such high values have never been observed. For AGN the cutoff seems to be lower and but it depends on the energy density in the photon and the magnetic field (see e.g., Ghisellini et al. 1998). As expected one sees an anti-correlation between maximal synchrotron frequency and the ratio for inverse-Compton radiation to synchrotron radiation.

In the case that there is an isotropic photon field as described by eq. (2.57) the inverse Compton processes will dominate the cooling of the accelerated electrons. In this case the effective photon field can be over a factor 100 higher than the magnetic field density (see eq. 2.58). This will significantly reduce the synchrotron cutoff to around $1keV/\zeta_2$ for the parameters discussed above with $\alpha_{\text{ref}} \approx 1$ – again independent of the black hole mass. However, as this cooling mechanism will not only effect the population of relativistic particles in the jet, but will also act on the normal jet plasma. In principle this could quench the whole jet.

The cooling timescales (eq. 2.60) are extremely short for the magnetic fields and photon densities around active black holes. In the case that the relativistic electrons are accelerated only once, the electrons will loose energy with the distance from the acceleration zone. Thus, the maximal energy of the electron distribution decreases with distance. This leads to a steepening of the power law in the spectral energy distribution for frequencies above a break frequency. This break frequency depends on the spectral age of the particle distribution ($\nu_b \sim B^{-3}/t^{-2}$, see e.g., Pacholczyk 1970). The spectral index above this frequency is modified by -0.5 (see e.g., Carilli et al. 1991). If there is more than one acceleration zone, e.g., the electrons are repeatedly reaccelerated, the average distance between these zones define the spectral age of the relativistic particles. As no such break is observed in low-hard state XRBs, we conclude that the electrons are nearly continously reaccelerated.

2.5 Scaling of the Jet

As we want to emphasize the scaling of the jet emission with mass and accretion rate, we describe the system using dimension-less variables, which are

denoted by small letters. The black hole mass is measured in solar masses

$$m_{\bullet} = \frac{M}{M_{\odot}}, \quad (2.65)$$

and the total accretion rate \dot{M} in terms of the Eddington accretion rate

$$\mathcal{V} = \frac{\dot{M}}{\dot{M}_{\text{Edd}}}. \quad (2.66)$$

The numerical value used in the subsequent formulas is $\dot{M}_{\text{Edd}} = 1.28 \times 10^{39} \frac{\text{erg}}{\text{s}c^2}$. Lengthscales will always be measured in gravitational radii of the central black hole e.g., the radius of the jet R_j will be written as

$$r_j = \frac{R_j}{R_G} \quad \text{with} \quad R_G = \frac{GM}{c^2}. \quad (2.67)$$

In this section we choose the electron power-law index $p = 2$ and consider the freely expanding jet with $\xi_2 = 1$, and $\xi_1 = \frac{1}{M}$. The Adiabatic index is assumed to be $\Gamma = 4/3$.

In this section we give numerical values from stellar mass black holes and parameters we consider to be of the correct order of magnitude. For these parameter we find for the magnetic field (eq. 2.17):

$$B = 7.9 \times 10^6 \text{G} \sqrt{\frac{\hat{q}_{e,2} \mathcal{V}}{\Gamma k_{\text{eq}} m_{\bullet}}} \frac{10}{r_j} \frac{5}{\gamma_j}. \quad (2.68)$$

2.5.1 Synchrotron Emission

At low frequencies below the transition frequency ν_{SSA} the jet emission is given by (eq. 2.39)

$$L_{\nu} = 8.5 \times 10^{19} \left(\frac{(\hat{q}_e/0.01) \mathcal{V} m_{\bullet}}{k_{\text{eq}}} \right)^{\frac{17}{12}} \frac{\mathcal{D}^{13/6} \mathcal{M} \sin^{\frac{1}{6}} i}{(\gamma_j/5)^{\frac{17}{6}} (f/10)^{\frac{5}{6}}} \frac{\text{erg}}{\text{s cm}^3 \text{Hz}}. \quad (2.69)$$

As we are considering the freely expanding jet we find a flat spectrum. The transition frequency is (eq 2.41):

$$\nu_{\text{SSA}} = 3 \times 10^6 \mathcal{D} \left(\frac{(\hat{q}_e/0.01)^2 \mathcal{V}^2}{(f/10)(\gamma_j/5)^4 k_{\text{eq}}^2 m_{\bullet} \sin i} \right)^{\frac{1}{3}} \frac{10}{r_{\text{acc}}} \text{GHz} \quad (2.70)$$

Above this synchrotron self-absorption frequency the optical thin power law takes over up to the high energy cut-toff (eq. 2.40):

$$L_\nu = 3.2 \times 10^{23} \left(\frac{(\hat{q}_e/0.01)\mathcal{V}m_\bullet}{k_{\text{eq}}} \right)^{\frac{7}{4}} \frac{\mathcal{M}\mathcal{D}^{2.5}}{(f/10)(\gamma_j/5)^{\frac{7}{2}}m_\bullet^{\frac{1}{2}}r_{\text{acc}}^{\frac{1}{2}}} \left(\frac{\nu}{\text{GHz}} \right)^{-\frac{1}{2}} \frac{\text{erg}}{\text{s cm}^3\text{Hz}} \quad (2.71)$$

The synchrotron cut-toff is at

$$\nu_{\text{max}} = 6.8 \times 10^{10} \frac{(\gamma_{\text{max}}/1000)^2 \mathcal{D}}{(\gamma_j/5)(r_{\text{acc}}/10)} \sqrt{\frac{(\hat{q}_e/0.01)\mathcal{V}}{k_{\text{eq}}m_\bullet}} \text{GHz} \quad (2.72)$$

if we fix the maximal Lorentz factor of the relativistic electrons (1 keV = 2.4×10^8 GHz). As we know that the cut-off is much higher for XRBs than for AGN, we do not improve our model by using the cut-off itself as a parameter. If the maximal Lorentz factor changes with black hole mass or accretion rate the scaling has to be changed accordingly. Furthermore, we do not consider an evolution of the maximal lorentz factor along the jet, even though it depends on the magnetic field which evolves with distance z . The derived cut-off is therefore only an approximation.

To derive the total emitted synchrotron luminosity we only have to take the steep spectrum into account. If the low and high energy cut-off is well separated we can approximated the total emitted power (in the fluid rest frame) as

$$L_{\text{Sync,total}} = 5.3 \times 10^{37} \frac{(\gamma_{e,\text{max}}/1000)\mathcal{M}\mathcal{M}(\hat{q}_e/0.01)^2\mathcal{V}^2}{k_{\text{eq}}^2(f/10)(r_{\text{acc}}/10)(\gamma_j/5)^4} \frac{\text{erg}}{\text{s}}. \quad (2.73)$$

We will usually be interested in the total emission in the rest frame of the jet, thus we have set the Doppler factor to one here. For the total integrated luminosity of the jet in the observers frame, we have to integrate the included Doppler factors over all angles. For a bulk Lorentz factor of 5 and $\alpha = 0.5$ this gives an additional amplification of a factor 2. The emitted synchrotron power has to be less than the total injected power of the jet. This constraint will be used to limit the possible parameter-space.

2.5.2 Synchrotron Self-Compton Emission

For the parameters used above the SSC emission is given by

$$L_{\text{SSC},\epsilon} = 6.9 \times 10^{36} \left(\frac{(\hat{q}_e/0.01)\mathcal{V}m_\bullet}{k_{\text{eq}}} \right)^{\frac{11}{4}} \frac{\mathcal{M} \ln \left(\frac{\epsilon_{\text{max}}}{\epsilon_{\text{min}}} \right) \frac{\text{erg}}{\text{s} \times \text{cm}^3 \text{keV}}}{m_\bullet^{\frac{3}{2}} (f/10)^2 (r_{\text{acc}}/10)^{\frac{3}{2}} \gamma_j^{\frac{9}{2}}} \left(\frac{\epsilon}{\text{keV}} \right)^{-\frac{1}{2}}. \quad (2.74)$$

The lower energy cut-off is, assuming $\gamma_{\text{min}} = 4$,

$$\epsilon_{\text{low}} = 7.2 \frac{(\gamma_{\text{max}}/1000) \sqrt{(\hat{q}_e/0.01)\mathcal{V}}}{(\gamma_j/5)(r_{\text{acc}}/10) \sqrt{k_{\text{eq}}m_\bullet}} \text{keV}. \quad (2.75)$$

The lower cut-off of the Lorentz factor may depend on other parameters like the black hole mass as well. For AGN $\gamma \gtrsim 100$ has been suggested (Biermann et al. 1995) due to hadronic interactions. For XRBs this value may be as low as the assumed $\gamma_{\text{min}} = 4$.

The high energy cut-off is scaled for stellar mass black holes:

$$\epsilon_{\text{high}} = 450 \frac{(\gamma_{\text{max}}/1000)^3 \sqrt{(\hat{q}_e/0.01)\mathcal{V}}}{(\gamma_j/5)(r_{\text{acc}}/10) \sqrt{k_{\text{eq}}m_\bullet}} \text{MeV}. \quad (2.76)$$

Even though this high energy cut-off is well above the electron rest mass energy, the effects due to the Klein-Nishima cross section will not be extreme. The total cross-section for Compton scattering decreases for photon energies comparable with the electron mass. This cross section is defined in the rest frame of the electrons (c.f., Rybicki & Lightman 1979). For $\gamma_{\text{max}} = 1000$ the scattering photon will have an energy around 450 keV and the Klein-Nishima effects reduce the cross section roughly by a factor two.

The total luminosity is again given by the integral of the flux density. The derived value will be too large as we do not consider the Klein-Nishima effect.

$$L_{\text{SSC,tot}} \leq 4.6 \times 10^{39} \frac{(\gamma_{\text{max},e}/1000)^{1.5} \gamma_{\text{min},e}^{0.5} \ln \frac{\gamma_{\text{max},e}^2}{\gamma_{\text{min},e}^2} \mathcal{M} \mathcal{M} (\hat{q}_e/0.01)^3 \mathcal{V}^3}{(f/10)^2 (\gamma_j/5)^7 k_{\text{eq}}^3 (R_{\text{acc}}/10)^2} \frac{\text{erg}}{\text{s}} \quad (2.77)$$

For moderate Lorentz factors with a high energy cut-off of a few hundred MeV, the over-prediction will only be a factor two, not a magnitude. Furthermore, for very high photon energies pair production has to be included, which increases the total energy loss again. The total luminosity has to be corrected for Doppler

boosting as the synchrotron emission.

To get an estimate when the total SSC emission dominates over the external Compton emission we divide the synchrotron photon density (eq. 2.47) by the equivalent far field photon density (see eq. 2.49) $U_{\text{Ph,disk}} = 1.210^{38} \eta \frac{\text{erg}}{\text{s}} \frac{\mathcal{V}}{16\pi Z^2 c \gamma_j^2}$:

$$\frac{\dot{\gamma}_{SSC}}{\dot{\gamma}_{EC}} = 619 \frac{(\gamma_{\text{max}}/1000)(\hat{q}_e/0.01)^2 \mathcal{V}(\gamma_j/5)^{1/2}}{(f/10)k_{\text{eq}}^2 \sqrt{(r_{\text{acc}}/10)} \sqrt{(z/100)}(\eta/10)} \quad (2.78)$$

The far field component of the external Compton emission will become dominant only for strong departures from the equipartition or for very low accretion rates. As we have seen in eq. (2.58) the external Compton emission is strongly increased if the photon field is scattered in the surrounding medium, for example in the broad line region, to produce an isotropic radiation field. In this case we find:

$$\frac{\dot{\gamma}_{SSC}}{\dot{\gamma}_{T,iso}} = 0.25 \frac{(\gamma_{\text{max}}/1000)(\hat{q}_e/0.01)^2 \mathcal{V}}{(\gamma_j/5)^{7/2} (f/10)k_{\text{eq}}^2 \sqrt{(r_{\text{acc}}/10)} \sqrt{(z/100)}(\eta/10)} \quad (2.79)$$

For large α_{ref} and η the inverse Compton emission can dominate the overall emission. This dominance increases with decreasing \hat{q}_e and \mathcal{V} but is independent of the black hole mass.

2.5.3 The Assumption of Equipartition

To derive the relativistic particle density we assumed that the energy density of the relativistic particles is – up to a constant factor k_{rel} – in equipartition with the energy in the magnetic field. It is generally assumed that the relativistic particles are accelerated in shocks using magnetic fields, thus we have to demand $k_{\text{rel}} \leq 1$. Energy conservation demands that the jet radiates less power than has been injected into the jet. The total power injected into the jet is $q_e \dot{M} c^2$ from which the fraction $\gamma_j q_m \dot{M} c^2$ is contained in the bulk motion of the plasma, and can not be radiated away without disrupting the jet. Therefore, the total luminosity of the jet has to be less than $\hat{q}_e \dot{M} c^2$, e.g.,

$$L_{\text{jet,tot}} \leq 1.210^{37} (\hat{q}_e/0.01) m_{\bullet} \mathcal{V} \frac{\text{erg}}{\text{s}} \quad (2.80)$$

For a low luminosity object this condition is easy to fulfill, as \mathcal{V} enters quadratic in the total synchrotron luminosity and in the third power for the

SSC luminosity (eq. 2.73 and 2.77). Furthermore, in these slowly accreting systems the radiative efficient standard disk is thought to be truncated and turns into an ADAF or a similar inefficient accretion flow in the innermost regions. The total disk efficiency is low and external Compton cooling from disk photons will not play a significant role. For highly accreting systems EC and SSC losses will be of a similar order (eq. 2.79). As EC cooling needs one additional unconstrained parameter (α_{ref}) compared to SSC losses, we will focus on SSC emission here, which will dominate the synchrotron emission in this regime. Thus, we find for the ratio of the emitted and injected power:

$$\frac{L_{\text{SSC,tot}}}{Q_{\text{jet,tot}}} = 1150 \frac{(\gamma_{\text{max}}/1000)^{1.5} (\gamma_{\text{min}}/4)^{0.5} (\ln \frac{\gamma_{\text{max,e}}^2}{\gamma_{\text{min,e}}^2} / 10) (\hat{q}_e / 0.01 \mathcal{V})^2}{(f/10)^2 (\gamma_j/5)^5 (r_{\text{acc}}/10)^2 (k_{\text{eq}}/3)^3} \leq 1, \quad (2.81)$$

where we include a factor 1/2 to account for the over-prediction due to the used Thomson cross-section. The most uncertain parameters of this equation is the equipartition parameter k_{rel} which enters into the fudge-factor f . The other parameters are reasonably well constrained. For a low-hard state XRB the synchrotron cutoff is at roughly 80 keV, so the maximal electron Lorentz factor has to be around 2000 – 4000. The minimal Lorentz factor γ_{min} has only a minor effect. Both parameters enter into the ratio only in low powers, thus small changes will not have a big impact. As we do not want to overestimate eq. 2.81 we choose $\gamma_{\text{min}} = 4$. The logarithmic factor is therefore of the order of 10. The jet radius where the particle acceleration starts can also not be varied a lot as discussed in section 2.3.3. A parameter of $r_{\text{acc}} = 10$ corresponds to a distance from the black hole of $z \approx 86$ for an Mach number of 8.6. For the parameters used the acceleration jet radius has to be increased a factor of 30, which would correspond to a distance z_{acc} from the black hole of 2500 Schwarzschild radii – far more than usually found. The Lorentz factor γ_j has the largest impact, as it enters in the fifth power. At for XRBs Lorentz factors significantly larger Lorentz factors than 5 are usually not found, but see Fender et al. (2004). Only for blazars and some other AGN Lorentz factors of $\gamma_j = 20$ have been reported.

With $\gamma_j = 5$ the constraint can only be fulfilled for a strongly accreting system ($\mathcal{V} = 1$) by leaving equipartition or by changing the overall settings, for example by quenching the whole jet. The qualitative behavior is sketched in Fig. 2.4. The radiated energy decreases quadratically with the accretion power, thus, low power accreting black holes can reach equipartition. Another

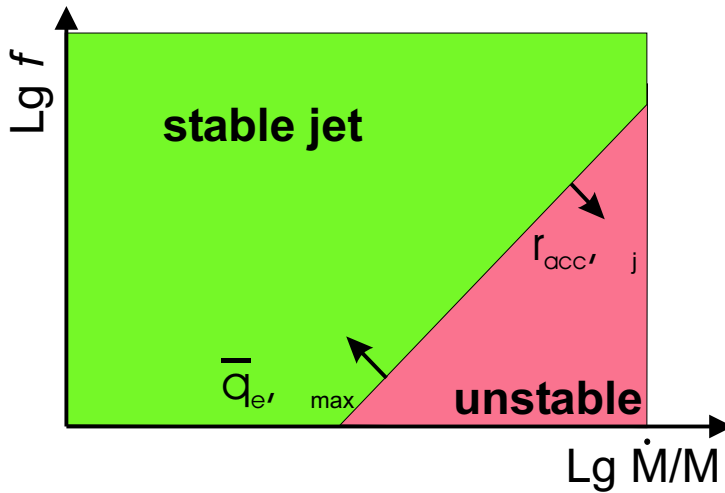


FIGURE 2.4— Stability of the jet: Qualitative dependence of the stability of the jet on the accretion rate and the fudge factor. The requirement that more energy is injected in the jet than radiated away is used to analyze whether the jet can be stable. The arrows indicate the displacement of the zone borders for an increase of the shown parameters, e.g., an increase of r_{acc} would enlarge the zone where the jet is stable. The term \dot{M}/M denotes the accretion rate divided by the Eddington accretion rate.

possibility for equipartition jets are fast jets with $\gamma_j = 20$, which are seen in BL Lac objects. Here the constraint is nearly automatically satisfied. As the jets of AGN tend to have higher Lorentz factors, AGN jets can stay in equipartition over a wider range of parameters than XRB jets.

2.5.4 Dependence on the Parameters

In this section we have given the emitted power of a jet for all major emission processes: synchrotron, SSC, and EC emission. Which one of these processes dominates the overall emission depends on the parameters of the jet. The projection of the parameter space to the accretion rate and reflection parameter α_{ref} is shown in Fig. 2.5, where the dominant emission process is indicated.

For $\alpha_{\text{ref}} \approx 0$ (no isotropic radiation field) only external Compton emission from the near and far field part is present and we have seen that synchrotron and SSC radiation dominates this effect (eq. 2.78). As the total SSC emission declines with \mathcal{V}^3 and the synchrotron emission only with \mathcal{V}^2 , synchrotron emission will be the dominant process for low accretion rates. For

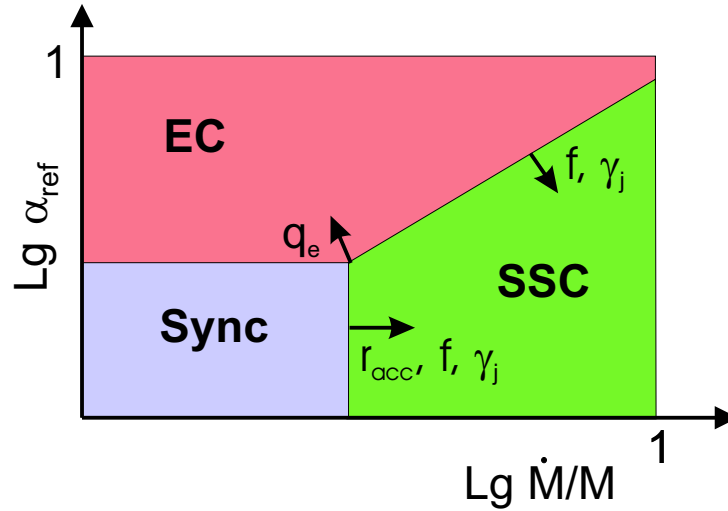


FIGURE 2.5— Dominant radiation process depending on the accretion rate and fraction of an isotropic radiation field (α_{ref}) for a constant disk efficiency $\eta \approx 0.1$. The arrows indicate the displacement of the zone borders for an increase of the shown parameters, e.g., an increase of r_{acc} would enlarge the zone where the synchrotron process is dominant and decrease the SSC zone. The other crucial parameters besides α_{ref} and \mathcal{V} are f , γ_j , \hat{q}_e , and r_{acc} .

higher accretion rate SSC emission will dominate. If the isotropic radiation field reaches a considerable fraction of the total radiation field emitted by the disk ($\alpha_{\text{ref}} > 0$) external Compton emission of an isotropic radiation field can dominate the overall emitted power.

The relative prominence of the different zones in Fig. 2.5 depends on the other jet parameters. Of main importance are the fudge factor f , which describes the equipartition of the jet, the Lorentz factor γ_j and the jet radius of the particle acceleration zone r_{acc} . An increase of any of these three parameters increases the parameter zone, where the synchrotron process is dominant in respect to the SSC zone. Similarly γ_j and f increase the EC zone. For a quantitative evaluation of the dominant process see Fig. 2.6. In this plot we present the dominant emission process for a set of usually used parameters. Furthermore, the effect of a change of the Lorentz factor is shown. It is important to note, that for the jet and the disk the black hole mass m_{\bullet} enters linearly in the total luminosities. Thus, the black hole mass has no influence which of the processes dominates.

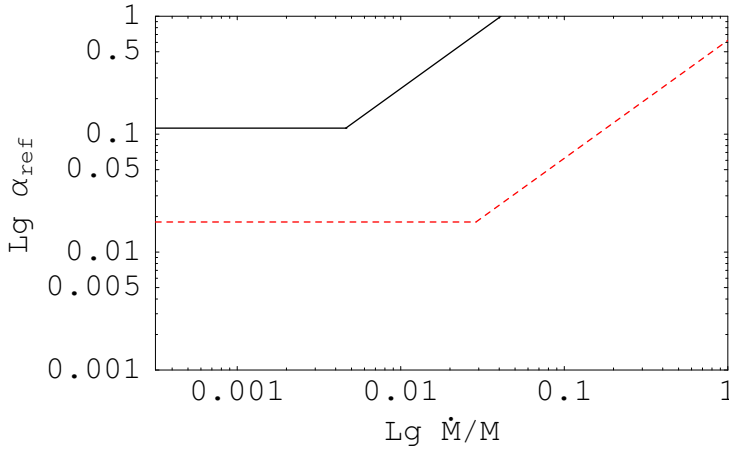


FIGURE 2.6— Quantitative analysis of the dominant radiation process similar to the sketch in Fig. 2.5. Above the lines, the system is EC dominated, while it is synchrotron or SSC dominated below. The dashed line is the result for $\gamma_j = 5$ and the solid line for $\gamma_j = 2$. The other parameters used are: $r_{\text{acc}} = 10$, $f = 10$, $k_{\text{eq}} = 3$, $\gamma_{\text{max}} = 1000$, and the SSC energy loss has been evaluated at the first acceleration region.

Up to now we have assumed that the total disk efficiency is a constant, however, this is probably not the case. It is usually assumed that only for high accreting systems the standard geometrically thin accretion disk (Shakura & Sunyaev 1973) reaches the innermost stable orbit. For slowly accreting systems the inner region ($\lesssim 100R_G$) of the accretion flow is probably an geometrically thick, optically thin inefficient flow (Esin et al. 1997). For larger radii this inefficient flow turns into a standard disk. The total power originating from an ADAF (Narayan & Yi 1994) or a similar solution changes with accretion rate as \dot{M}^2 . Once one reaches the critical accretion rate, where the ADAF turns into a thin disk, the disk efficiency will increase rapidly. In this regime the total luminosity scales with \dot{M}^1 . This behavior is shown in Fig. 2.7.

The luminosity of the jet depends on the square of the accretion rate for a synchrotron or external Compton dominated jet. In the SSC regime it even goes with the third power of the accretion rate. However, this at least quadratic dependence can not hold for the whole parameter space, as the jet can not radiate more power than injected (see the discussion in the last subsection). Once the jet radiates a significant fraction of its internal energy, the total emitted luminosity can depend at most linearly on the accretion rate. This has also been sketched in Fig. 2.7. Two possibilities are shown. As suggested by Maccarone

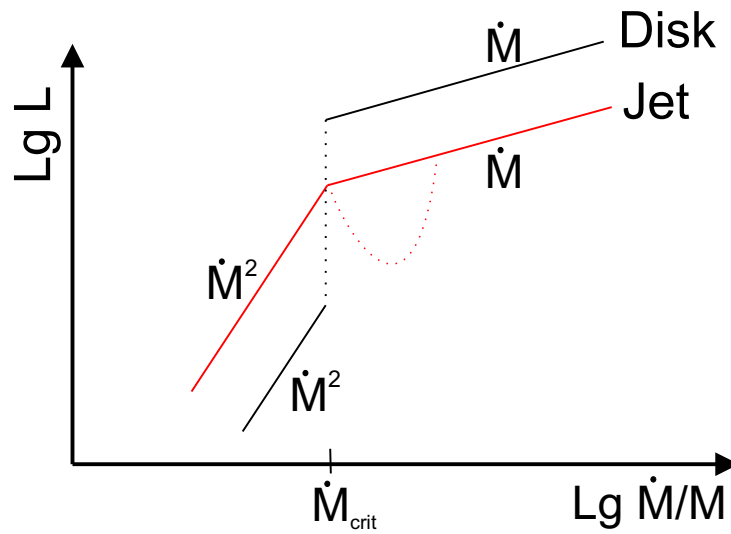


FIGURE 2.7— Scaling of the intrinsic jet and disk luminosities on the accretion rate if the jet synchrotron dominated.

et al. (2003) it may be that the jet is first quenched and reappears for very high accretion rates (very high state objects). The quenching may happen by EC cooling from scattered disk photons. The other possibility is that the jet is always there and just changes its scaling.

If one includes the scaling of the accretion flow in Fig. 2.5 we arrive at Fig. 2.8. If the disk efficiency declines fast for accretion rates smaller than the critical accretion rate, EC from scattered accretion disk photons will not contribute to the total jet emission. Thus, synchrotron emission is the dominant process for low accreting systems. For large enough α_{ref} parameters such that EC cooling plays a role, we find that for increasing accretion rate a jet is first synchrotron dominated, then EC dominated and finally for the highest accretion rates SSC dominated. It is suggestive to speculate: Jet emission with such α_{ref} values may explain the behavior of Galactic XRBs. In the low-hard state the system is dominated by synchrotron emission. For larger accretion rates the system changes its state into the high state. Due to the EC cooling the relativistic jet is quenched and no longer visible. Only when enough energy is inserted into the jet it reappears in the very high state as an instable SSC dominated jet.

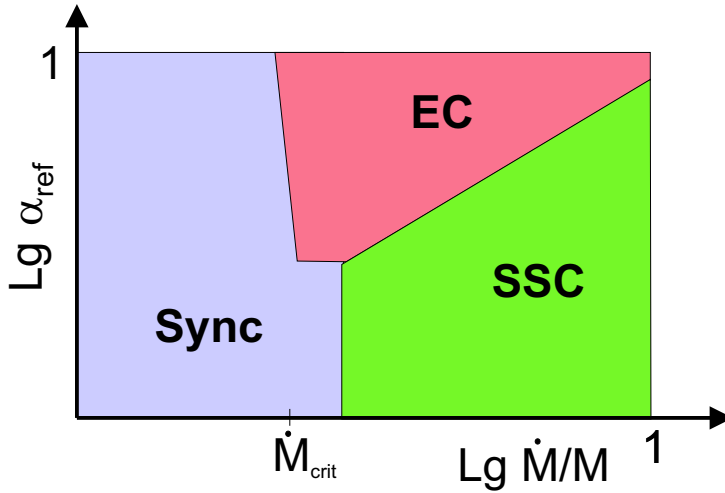


FIGURE 2.8— Dominant radiation process depending on the accretion rate and fraction of an isotropic radiation field (α_{ref}) if the disk turns into an inefficient flow for $\mathcal{V} < \mathcal{V}_{\text{crit}}$. For comparison see the similar plot in Fig. 2.5. The arrows indicate the variation of the zone boundaries for an increase of the given parameters.

2.6 Discussion

In the previous sections we have derived the emission of a simple jet model. As the process of launching relativistic jets is still under debate and there are no analytical models available, we treat the connection between the accretion flow and the jet ejection as a black box which we parameterize. Using these coupling parameters and the relativistic Bernoulli equation, we can derive the magnetic field and the relativistic particle density. The main parameters describing the jet are the black hole mass and the accretion rate. Further important parameters are the bulk Lorentz factor γ_j , the fraction of non rest-mass accretion power ejected into the jet \hat{q}_e , and the fudge-factor f , which describes if the jet is in equipartition. The magnetic field and particle density are used to derive the synchrotron and SSC emission from the jet. The formulas describing the emission have been formulated in a way that the scaling which jet power and black hole mass is apparent.

We have shown, that the total emitted power of the jet can either be dominated by synchrotron, SSC or EC emission. Which one of those dominates depends mainly on the accretion rate and the fraction of the isotropic radiation field α_{ref} . Besides these two, it also depends on the jet radius in the first par-

tion acceleration region r_{acc} , the Lorentz Factor γ_j and the fudge factor f . In the case that the external Compton emission dominates the emission from the jet, it may well be that the jet will be quenched, as the bulk motion will also be 'Compton cooled'. Such a behavior is for example seen in Galactic black hole XRBs. The radio emission of high state XRBs is quenched by at least a factor 100 compared to their low-hard state (c.f., Tanaka & Shibazaki 1996). Only for very-high state objects the jet reappears but is unstable.

The constraint that the total power of the jet has to exceed the radiated power has been used to argue that moderately fast jets ($\gamma_j \approx 5$) of strongly accreting systems can not be in equipartition. If there is a mechanism that transfers energy from the magnetic field to the relativistic particles, so that the jet approaches equipartition fast, it may be that the whole jet is unstable or quenched. This constraint of the total power is easily fulfilled for low accreting systems or very fast jets.

The optical thin part of the spectrum of a jet can always be described by a simple power law up to the synchrotron cut off. If the source varies, the power law can only vary in intensity and spectral index. This constrains the type of variability a jet-dominated source can have.

The above developed theory in the version of Falcke & Biermann (1995) has been tested for AGN in subsequent papers e.g., Falcke & Biermann (1999); Falcke et al. (1995b) and others. In this thesis we use the model to unify all low-power accreting black hole and further test the model for AGN and XRBs. In the next chapter we will establish the radio/X-ray correlation for AGN and XRBs. The beaming hypotheses contained in the model is explored for the phenomenon of ULXs. The strong constrains for the variability of this model will be tested as well.

3

A Scheme to Unify Low-Power Accreting Black Holes

3.1 Introduction

In the previous chapters we have developed the jet/disk connection for XRBs and AGN. Here we will use the scaling laws to argue for a unifying view of low power accreting stellar and supermassive black holes. This work has mostly been published in Falcke, Körding & Markoff (2004). While the signature of the accretion flow is usually a thermal component in the spectral energy distribution, the jet can contribute significantly over a broad energy range: from radio to Γ -rays (see e.g., von Montigny et al. 1995). For stellar mass XRBs accretion flow models (e.g., Shakura & Sunyaev 1973) accompanied by a hot corona correctly predict the soft X-ray emission (Sunyaev & Trümper 1979). These models can be scaled for the black hole mass and accretion power to AGN, where this thermal component is often called the “big blue bump” (Sanders et al. 1989; Sun & Malkan 1989). The jet emission scaling, which governs at least the radio cores, has been developed in chapter 2 or Falcke & Biermann (1995); Kaiser & Alexander (1997); Heinz (2002) and successfully applied to XRBs and AGN (Falcke et al. 1995b; Falcke & Biermann 1996, 1999).

The most important parameters of accreting black holes are probably the mass and the accretion rate, both of which can vary over many orders of magnitude. Additional parameters which likely impact the observable characteristics of black holes are the spin and the inclination angle of their spin axes.

Inclination-based unified schemes of AGN merge apparently different objects based on the angle between the spin axis and the line of sight (see e.g., Antonucci 1993; Urry & Padovani 1995a). The success of this scheme supports the evidence for angle-dependent obscuration and relativistic beaming.

However, the exact effect that changes in the accretion rate have on the appearance of their associated black holes systems is a matter of ongoing debate. A good understanding of this is crucial for modeling the cosmic evolution of black holes and for disentangling the different source classes.

A number of recent results suggest that the transition from a high accretion rate black hole to a low accretion rate one is not smooth, but rather accompanied by a “phase transition”. In the low-power phase, the optically thick disk emission is either dominated by emission from an optically thin corona, completely reduced to a radiatively inefficient inflow, or is truncated and an optically thin inner radiatively inefficient flow exists closer to the compact object (see Poutanen 1998 for a review of the various models). For XRBs Esin et al. (1997) estimate that this transition occurs once the accretion rate for a black hole of mass M_{\bullet} drops to less than a critical value ($\sim 10\%$ of the Eddington accretion rate, $\dot{M}_{\text{Edd}} \simeq 2 \times (M_{\bullet}/10^8 M_{\odot}) M_{\odot} \text{ yr}^{-1}$ for $\dot{M}_{\text{Edd}} = L_{\text{Edd}}/0.1c^2$). More recent work suggests that this transition could already occur around 2% \dot{L}_{Edd} (Maccarone 2003), and that there is a hysteresis in the critical accretion rate value depending on which direction the transition is going along (Maccarone & Coppi 2003). Regardless of the exact details, a crucial point for this chapter is a phase-transition as a function of black hole mass and accretion power.

We have suggested in chapter 2 that the contribution of jets and outflows on the spectral energy distribution (SED) of black holes can be significant in supermassive as well as stellar mass black holes (for earlier studies see, Falcke & Markoff 2000; Markoff et al. 2001a; Fender 2001; Yuan et al. 2002a) and that the jet contribution may in fact dominate the disk emission in a JDAG – a jet-dominated accretion flow. Jets are inherently broad-band, since they remain self-similar over many orders of magnitude in spatial scale and produce non-thermal particle distributions ranging over many orders of magnitude in energy. For this reason they should always be considered as potential contributors at every wavelength. This concept of jet domination has now been empirically demonstrated for XRBs, where below $L_{\text{Edd}} \approx 10^{-4}$ the kinetic energy output through radiatively inefficient jets (assumed to radiate only radio through IR) dominates the radiative output of the optically thin or thick disk (assumed to solely account for the X-ray emission; Fender et al. 2003). The same holds true for LLAGN (Nagar et al. 2004, in prep). If the jet contributes to the X-rays as

well, the jet domination may hold at even higher absolute luminosities.

The importance of jets to the emission of low-power accreting black holes may hold the key to understanding the relationship between stellar and galactic sized systems. In the next section we suggest how this concept can be used to provide a unified picture for AGN as a function of mass and power for a range of sources that may be operating at sub-Eddington accretion rates. This directly leads to a prediction of radio/optical/X-ray scaling which we test on data from several sources in Sect. 3.

3.2 Low-Power Unification

3.2.1 A Scheme for Sub-Eddington Black Holes

Our proposed scheme is based on three assumptions:

I) The accretion flow and disk form a coupled jet-disk system, with jet and disk always being present in some form (“jet-disk symbiosis”, see Falcke & Biermann 1995).

II) Below a certain critical accretion rate, $\dot{M}_c \simeq x \times \dot{M}_{\text{edd}}$ ($x \simeq 0.01 - 0.1$), the inner part of the accretion flow becomes radiatively inefficient (e.g., Esin et al. 1997, Fig. 2.7).

III) Below \dot{M}_c , or for face-on orientation (relativistic beaming), the jet emission dominates the emission from the accretion flow (e.g., Yuan et al. 2002a).

In short, the postulate is that *near-Eddington black holes are disk-dominated and distinctly sub-Eddington black holes are jet-dominated.*

Can we classify many of the various accreting systems we know of in terms of this scheme, based on observational evidence? Let us first consider X-ray binaries where time scales are short enough that individual sources can appear in a number of different states. The two most pronounced states are the high (soft) state, with a soft power-law spectrum dominated by a thermal “bump”, and the low (hard) state characterized by a dominant hard power-law and weak-to-absent thermal spectrum (e.g., Nowak 1995). The former is commonly interpreted as multi-color blackbody emission from a standard thin disk, while the latter is commonly attributed to an optically thin accretion flow or corona. However, Markoff et al. (2001a) have suggested that the hard power law could also be attributed to synchrotron emission from the jet in these systems. This is strengthened by the finding of a tight non-linear correlation between radio and X-ray luminosity in GX 339–4 (Corbel et al. 2003) and other X-ray binaries in the low state (Gallo et al. 2003, see Fig. 3.1), which exactly fits the non-

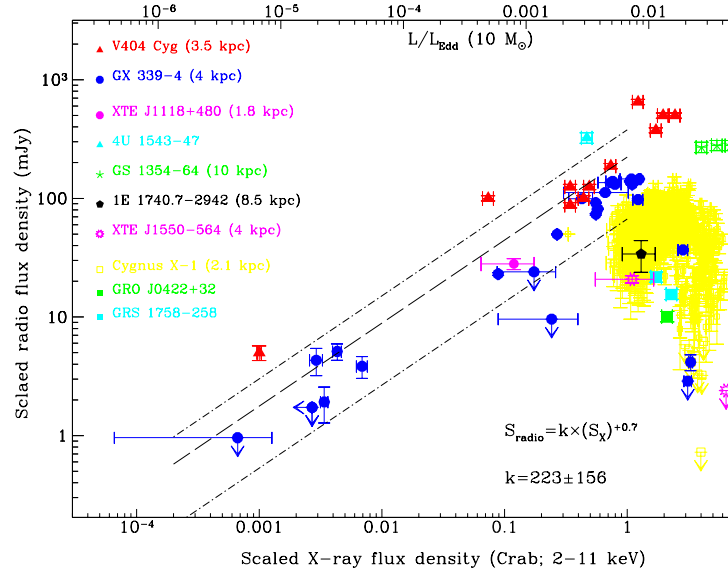


FIGURE 3.1— Universal radio X-ray correlation for low-hard state black hole XRBs. While the first five sources are typical low-hard state objects, the other objects like Cyg X-1 are never totally in this state and change states regularly. This plot has been reproduced from Gallo et al. (2003).

linear predictions of the jet model (e.g., Markoff et al. 2003, for GX 339-4). This correlation extends down into the quiescent state, which is therefore now interpreted as an extremely low luminosity hard state. It has also been argued that some of the ultra-luminous X-ray sources in nearby galaxies could be the beamed equivalents of the well-known Galactic XRBs (“microblazars”; Mirabel & Rodríguez 1999; Körding et al. 2002).

For AGN, the situation is more complicated since a large number of source classes exist. When considering higher luminosity sources with strong disk signatures, the supermassive black hole equivalents to soft state XRBs are FR II radio galaxies, radio-loud quasars, and blazars (with emission lines) among the radio loud objects. Within the standard “unified scheme” these are mainly related through different inclination angles. On the radio quiet side, Seyfert galaxies, radio-quiet quasars, and perhaps radio-intermediate quasars (Miller et al. 1993; Falcke et al. 1996) are the other analogs for high state XRBs. All of these AGN varieties show direct or indirect evidence for a soft ultraviolet bump that can be readily understood as emission from a standard

accretion disk (Sun & Malkan 1989). This emission also provides ample photons to produce the strong emission line regions seen in the optical spectra.

On the other hand, several low-power AGN classes seem to lack evidence of a blue bump and strong emission lines, and are therefore candidates for equivalents to the hard state XRBs. These are FR I radio galaxies, BL Lacs and LINERs. The Galactic Center (Sgr A*); see Melia & Falcke 2001) could also be in this category, but with its faint and soft spectrum it is not clear what state in XRBs it would correspond to. However, the almost-daily flares in Sgr A* (Baganoff et al. 2001) have a hard spectrum, so it may therefore occasionally achieve a state analogous to the hard state in XRBs.

In terms of radio power, FR I radio galaxies form a smooth continuum with FR II radio galaxies, but are comparatively underluminous in emission lines and lack a big blue bump (Falcke et al. 1995a; Zirbel & Baum 1995). While FR I sources do seem to have optical cores, their fluxes scale tightly with their radio flux (Chiaberge et al. 1999). This has been used to argue for a synchrotron nature of these optical cores rather than a thermal origin in the accretion disk. Interestingly, within the standard unified scheme FR I radio galaxies are coupled to BL Lac objects which are thought to be their relativistically beamed versions. BL Lacs – by definition – lack emission lines and there is no population intermediate in inclination angle between FR I and BL Lacs which does show a blue bump or evidence for a standard optically thick accretion disk.

Similarly, for low-luminosity AGN and LINERs, Ho (1999) argues that their SED precludes the presence of a blue-bump and of a standard accretion disk. On the other hand, radio observations of LINERs show a strong jet presence (Falcke et al. 2000; Nagar et al. 2001) and fits to individual objects indicate that the higher wavelengths may also be dominated by jet emission (Yuan et al. 2002b). Some of these LINERs are in big elliptical galaxies and may be the lower-luminosity continuation of FR I radio galaxies, while others sit in spiral galaxies and may be somewhere in between Seyferts and our own Galactic Center in terms of power.

Hence BL Lacs, FR Is, and LINERs are good candidates for sub-Eddington and jet-dominated AGN. Although this conclusion is already widely accepted for BL Lacs because of beaming arguments, and the case for FR Is is strengthening, the proposal for LINERs remains highly debated.

A sketch of the proposed scheme is shown in Fig. 3.2. Note that this is naturally very rough. In a number of cases the dividing lines between individual classes may be blurred. Also, in jet-dominated sources there may still be a

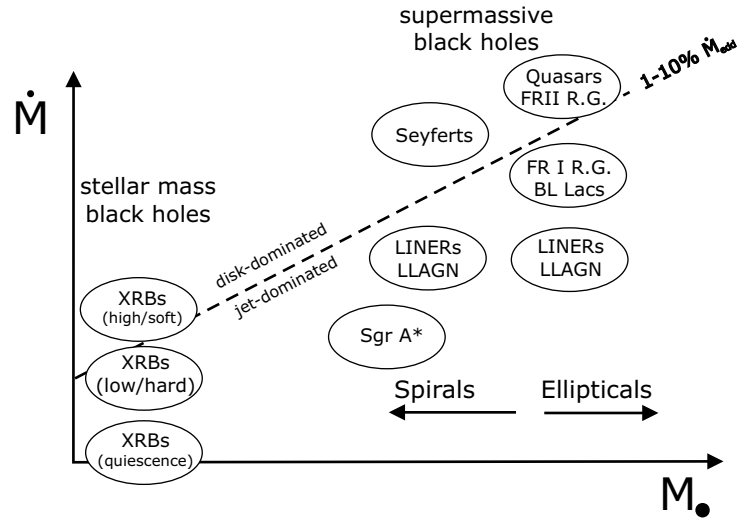


FIGURE 3.2— A proposed unification scheme for accreting black holes in the mass and accretion rate plane. Above a few percent of the Eddington accretion rate, the systems are proposed to be dominated by disk emission, while below they are inherently dominated by jet emission (RG=radio galaxy). Standard inclination-based unified schemes (Antonucci 1993; Urry & Padovani 1995a) are still assumed to be valid but are not explicitly shown here. Given a correlation between bulge mass and black hole mass, the AGN with the most massive black holes are supposed to reside in elliptical galaxies, while less massive black holes are predominantly in spirals. This is, of course, not applicable to XRBs.

sizeable disk contribution and vice versa. In addition, as is commonly known, inclination effects play an important role in unified schemes. For radio loud quasars, for example, a small inclination to the line-of sight (i.e., in a blazar) can lead to a significant jet contribution despite the fact that here we classify these sources as intrinsically disk-dominated. This is in contrast to BL Lacs objects, which we consider as *intrinsically* jet-dominated in addition to being beamed (with FR I radio galaxies as the parent population). This may have some analogy for XRBs, where some Ultraluminous X-ray sources might be affected by beaming as well (Körding et al. 2002). In general the selection of BL Lacs requires significant care (Landt et al. 2002; Marcha et al. 1996) and the application of the scheme is not always straightforward without good understanding of source properties and selection effects.

3.2.2 Consequences and Tests of our Proposed Unification Scheme

With such a scheme at hand, one wonders what the consequences are and how they can be tested. First of all, if indeed black hole engines make a qualitative transition with accretion power, a number of AGN diagnostics have to be considered with even greater care. One example is the ratio between radio and optical flux that is commonly used as a radio-loudness parameter (Kellermann et al. 1989; Falcke et al. 1996). In most interpretations it is supposed to represent the relative prominence of jet and disk in a source. This has been particularly useful for quasars, where one can well assume that the optical flux represents disk emission. If, however, in sub-Eddington AGN both wavelengths are coming from the jet, this parameter is physically no longer meaningful as a jet-strength parameter and other factors have to be taken into account.

This issue is particularly difficult when considering large samples of AGN. Within each luminosity bin one can expect a range of black hole masses to contribute and hence Eddington and sub-Eddington black holes may be mixed if there are no well-sampled SEDs and spectra in radio, optical, and X-rays. Moreover, mass itself can become a crucial factor. This can in principle enhance scatter and spoil any possible correlations or dichotomies. On the other hand, if the SED of black holes is jet-dominated, it may be possible to describe their evolution with accretion power in a unified way. In the following we will now concentrate on the expected scaling of radio, optical, and X-ray emission from a jet-only model and compare it to data from samples of sub-Eddington black holes.

3.3 The X-Ray/Radio Correlations

3.3.1 The Predicted Scaling

Here we want to concentrate on the AGN core itself, leaving out the extended emission. In the simplest picture (Blandford & Königl 1979; Falcke & Biermann 1995), the jet spectrum can be naturally described by a flat-to-inverted radio spectrum up to a turn-over frequency ν_t , which reveals an optically thin power-law (see Fig. 3.3). The flat spectrum is the sum of self-absorbed components along the jet, where higher frequencies correspond to smaller regions closer to the black hole. The power law results from optically thin emission from a power-law distribution of electrons at the smallest scale in the jet where particle acceleration exists. One can then roughly approximate the jet spectrum by a broken power law normalized to a monochromatic luminosity (energy per time and frequency) L_t at ν_t ,

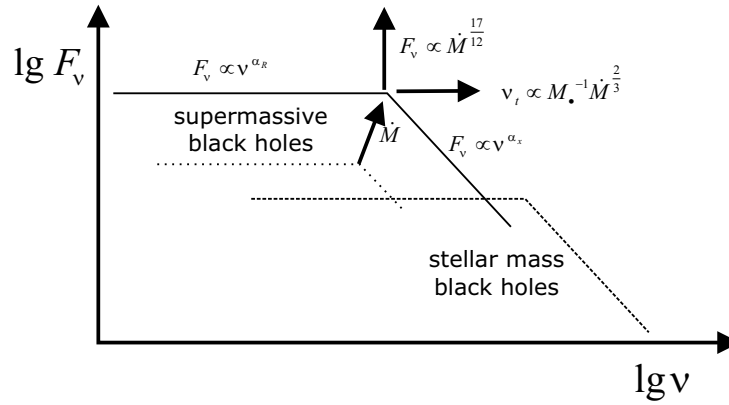


FIGURE 3.3— A schematic jet spectrum and its theoretically expected scaling with mass and accretion rate. The spectrum has a flat-to-inverted, optically thick part below a turn-over frequency ν_t and a steep optically thin spectrum above. For most sources the flat-to-inverted part of the spectrum will be in the radio/infrared while the steep part will be in the optical and X-rays. A change in the absolute accretion rate will shift the spectrum along a diagonal line from the bottom left to the top right. A change in mass will shift the spectrum horizontally only. Lowering mass *and* accretion rate (e.g., by keeping the accretion rate at a constant fraction of the Eddington accretion rate) will shift the spectrum towards the bottom right, where stellar mass black holes are found.

$$L_R = L_t \left(\frac{\nu}{\nu_t} \right)^{\alpha_R} \quad \text{for } \nu \ll \nu_t \quad \text{and} \quad (3.1)$$

$$L_X = L_t \left(\frac{\nu}{\nu_t} \right)^{\alpha_X} \quad \text{for } \nu \gg \nu_t, \quad (3.2)$$

where $\alpha_R \simeq 0.15$ and $\alpha_X \simeq -0.6$ are the typical optically thick (radio) and optically thin (optical and X-ray) spectral indices (e.g., Markoff et al. 2003). This spectrum can be mirrored to higher energies by inverse Compton processes, leading, for example, to the characteristic 'camel's back' SED of BL Lacs in a νL_ν representation.

Scaling laws for this type of jet spectrum as a function of jet power Q_j and mass have been described in chapter 2 (see also Falcke & Biermann 1995; Markoff et al. 2003). The main assumptions are that the jet expands freely (conical shape), maintains an (arbitrary but fixed) equipartition factor, and the distance of the first particle acceleration zone, z_{acc} , scales linearly with mass,

e.g., is always around some hundred to thousand R_g . $R_g = GM_\bullet/c^2$ is the gravitational radius of the black hole.

As we want to use a electron power law distribution with $p > 2$ and include an inverted radio spectrum we will not use the scaling laws of section 2.5 for the radio and X-ray emission, but only for the fairly robust radio core and the synchrotron self-absorption frequency. We know from eq. (2.69) and (2.70) that $L_t \propto Q_j^{17/12}$ and $\nu_t \propto Q_j^{2/3} M_\bullet^{-1}$. As described in Falcke & Biermann (1995) or eq. (2.39) the exponent of the radio power only changes by 3% if one uses $p = 2.5$ compared to $p = 2$, thus we will use the above mentioned $p = 2$ values. Hence we find:

$$L_R \propto Q_j^{\frac{17}{12} - \frac{2}{3}\alpha_R} M_\bullet^{\alpha_R} \left(\frac{\nu}{\nu_R}\right)^{\alpha_R} \quad \text{for } \nu \ll \nu_t \quad \text{and} \quad (3.3)$$

$$L_X \propto Q_j^{\frac{17}{12} - \frac{2}{3}\alpha_X} M_\bullet^{\alpha_X} \left(\frac{\nu}{\nu_X}\right)^{\alpha_X} \quad \text{for } \nu \gg \nu_t, \quad (3.4)$$

where ν_R and ν_X are two fixed reference frequencies. If we combine these equations we find the expected radio/X-ray correlation

$$L_X \propto L_R^m M^{\alpha_X - m\alpha_R} \quad (3.5)$$

where

$$m = \frac{\frac{17}{12} - \frac{2}{3}\alpha_X}{\frac{17}{12} - \frac{2}{3}\alpha_R}. \quad (3.6)$$

Thus, to correct for the different masses of the objects we define an equivalent optically thin (e.g., X-ray) luminosity

$$L'_X = L_X \left(\frac{\nu}{\nu_X}\right)^{\alpha_X} \left(\frac{M}{6M_\odot}\right)^{m\alpha_R - \alpha_X} \quad \text{for } \nu \gg \nu_t. \quad (3.7)$$

For the examples of $\alpha_R \simeq 0.15$ and $\alpha_X \simeq -0.6$ we get $m \simeq 1.38$ and the mass correction factor is predicted to go with $M^{0.81}$.

For relativistic steady jets, there will also be a dependency on the Doppler factor $\mathcal{D}^{2-\alpha}$ (Lind & Blandford 1985). However, since as a first-order approximation the monochromatic luminosity at both frequencies is beamed by the same amount, the correlation between L_R and L_X will only go as $L_R/L_X \propto \mathcal{D}^{\alpha_X - \alpha_R}$, i.e. less than linear for typical values. If there is a significant velocity gradient along the jet, radio and X-rays could be beamed by

different amounts and the effect would become stronger.

Further parameters may affect the correlation. For example, source-to-source variations in the equipartition factors or the turn-over frequency ν_t caused by different locations of the first acceleration zone z_{acc} can lead to different X-ray/radio ratios. However, since we have no good theoretical understanding of such plasma parameters we have to accept this uncertainty as a major source of scatter.

The scaling also only holds as long as a non-thermal power law is produced in the optically thin regime and α_X remains roughly constant. This may not always be the case for sources that approach quiescence, such as the Galactic Center in its non-flaring state.

At least for an individual X-ray binary, Markoff et al. (2003) showed that this scaling with accretion rate can exactly reproduce the tight non-linear radio/X-ray scaling of the X-ray binary GX 339–4. Such a scaling has now been found to be fairly representative for low-luminosity XRBs (Gallo et al. 2003). In the case of GX 339–4, the mass term and Doppler factor were not included in the formula, since only one source was considered. This is fine for XRBs, where the jet power and accretion rate in one object changes over many orders of magnitude within months and years. For AGN such changes take too long to be discovered in individual objects and hence statistical samples have to be used to cover a large range in instantaneous jet powers and accretion rates. In this case the mass becomes an important factor for the thermal *and* non-thermal spectrum.

An important additional point concerns which wavelength to use in such comparative studies of different source types and black hole masses. In the scaling law, we have been mainly comparing the optically thick flux (mainly radio) to the optically thin flux (mainly X-rays, see e.g. Fig. 2.3 for the synchrotron and inverse-Compton branch). But, it is important to know which wavelength belongs to which branch of the jet SED in a certain type of source. In essentially all sources the *compact* radio emission is safely on the optically thick branch of the jet core spectrum, however, since the turnover frequency scales inversely with mass, the useful wavelength range over which one can probe the optically thin branch of the SED may vary from one type of source to another. We know, for example, that in BL Lacs at least the optical part of the SED belongs to the synchrotron branch. In some cases this extends all the way into the X-rays in other cases, however, X-rays may already be affected by the inverse Compton components of the SED. Hence, optical flux measurements are a much safer region for BL Lacs (and FR I radio galaxies

for that matter) to probe the optically thin part of the SED (which we still parameterize by ν_X and L_X). On the contrary, X-ray binaries may have a very high turn-over frequency, so that the optical flux may still be on the optically thick branch (as discussed in Markoff et al. 2001a). Here, X-ray fluxes are the better choice, even though also here inverse Compton might contribute. Whatever one chooses, a proper comparison requires one to normalize the optically thin and optically thick fluxes to common reference frequencies. This is done in Eq. (3.7). Since we here use an X-ray frequency as the common reference frequency for the normalized optically thin flux, we stay with the term radio/X-ray correlation in the following, even though it could for a number of sources equally well be a radio/optical correlation.

3.3.2 The Scaling of Synchrotron Self-Compton Emission

Up to now we only considered synchrotron emission, but for high photon energies inverse Compton emission could also contribute. Especially for XRBs there are arguments that the X-rays could be created by Compton scattering. The external Compton emission created through upscattering of disk photons will scale similar to the synchrotron emission as we only have to exchange the magnetic field density U_B with the photon density U_{ph} in the emission formulas. However, synchrotron self-Compton emission will depend differently on the accretion rate. To derive its correlation coefficient let us first reconsider the synchrotron emission. For a flat radio spectrum and a spectral index of -0.5 we can use the equations from section 2.5 directly to derive the correlation. For the radio emission we find (eq. 2.69)

$$L_R \sim Q_j^{17} \quad (3.8)$$

and for the optical thin synchrotron emission (eq. 2.71):

$$L_X \sim Q_j^7 m_\bullet^{-\frac{1}{2}} \quad (3.9)$$

and we arrive at a correlation constant of $m = \frac{21}{17} = 1.24$. The correlation constant increases with increasing p (see 2.39 & 2.40). This and the inverted radio spectrum leads to the used value of $m = 1.38$. For SSC emission on the other hand, we have (eq. 2.74)

$$L_{SSC,X} \sim Q_j^{\frac{11}{4}} m_\bullet^{-\frac{1}{2}} \quad (3.10)$$

Thus we arrive at a correlation constant of $m = \frac{33}{17} = 1.94$. This constant will be further increased by the inverted radio spectrum and the steeper optical thin part. Thus, for SSC we find $m \gtrsim 2$, far more than found in the universal radio/X-ray correlation found for low/hard state XRBS (Gallo et al. 2003). We conclude that the X-ray emission in low/hard state XRBS cannot be dominated by SSC emission.

3.3.3 The Samples

To test finally our hypothesis that the radio/X-ray correlation can be traced from XRBS through LINERS, FR Is, to BL Lac objects, we use a number of different samples from the literature where mass estimates, radio and X-ray or optical fluxes have been published. For certain types of sources (e.g. LLAGN) we are naturally limited by the small number of well-defined samples that have been observed with the new generation of X-ray telescopes.

For the XRBS we include the above mentioned multiple epochs of GX 339–4 (Corbel et al. 2003). We scaled the 8.6 GHz radio flux to 5 GHz, assuming ($\alpha_R = 0.15$). Hynes et al. (2003) give a mass for GX 339–4 around $6M_\odot$. A distance of 4 kpc has been used to derive the luminosity (Zdziarski et al. 1998). We note that other methods may give somewhat different distances (e.g., Maccarone 2003) and that the mass is a strict lower limit. Nevertheless, the correlation for GX 339–4 seems to be representative for a large number of XRBS in the hard state (Gallo et al. 2003).

As the lowest luminosity supermassive black hole, we included Sgr A*. The 5 GHz radio flux was taken from the average spectrum in Melia & Falcke (2001). The X-ray luminosity in the quiet and the flaring state were taken from (Baganoff et al. 2001), which we scaled with the given photon indices to a 3-9 keV luminosity. The black hole mass is taken to be $3 \times 10^6 M_\odot$ (Schödel et al. 2002) and the distance of 8 kpc has been used.

For the LINERS we included the Chandra sample of Terashima & Wilson (2003). They selected 14 objects with radio cores from the Low-Luminosity AGN (LLAGN) sample of Nagar et al. (2000), with a flat or inverted radio core ($\alpha_R \geq -0.3$). Nagar et al. (2000) selected their sources from the Ho et al. (1995) sample (a magnitude limited sample) according to preliminary spectral classification as LINER or as transitional object. To compare the X-ray luminosity with GX 339–4, we scaled the 2-10 keV X-ray luminosity to a 3-9 keV luminosity assuming a power law index of $\alpha_X = -0.6$ for all objects.

For the FR Is, we took the radio and HST data given in Chiaberge et al. (1999) who selected their sample from the 3CR catalogue (Spinrad et al. 1985)

which have been morphologically identified as FR I radio sources. The 33 sources form a complete, flux limited sample. The optical cores have been extrapolated to a corresponding X-ray luminosity using Eq. (3.4) under the assumption that the synchrotron power law has a spectral index of $\alpha_X = -0.6$. We did not use actual X-ray data, as the HST observations had higher resolution and within the jet model for FR I and BL Lacs some of these high-mass sources could have their synchrotron cut-off already below the X-ray band, such that X-rays could be dominated by synchrotron self-Compton.

For the BL Lacs we took X-ray (XBLs) and radio selected (RBLs) BL Lacs from Sambruna et al. (1996). These originate from two complete samples: the Einstein Observatory Extended Medium-Sensitivity Survey (EMSS) XBL sample (Morris et al. 1991) and the 1 Jy RBL sample (Stickel et al. 1991). Similar to FR Is we calculate the corresponding monochromatic X-ray luminosity from the optical data assuming $\alpha_X = -0.6$. Since BL Lacs are thought to be strongly affected by beaming, we corrected the radio and the equivalent X-ray luminosity for Doppler boosting, assuming an average Doppler factor of $\mathcal{D} \simeq 7$ (Ghisellini et al. 1993). As mentioned above, for the X-ray/radio correlation the Doppler factor largely cancels out and enters less than linearly. Of course, the position *along* the correlation will be affected more strongly. For all source populations other than the BL Lacs, we assume a Doppler factor around unity.

For all sources we calculated the radio luminosity from the 5 GHz flux density. The distances of the sources were derived from the redshift with $H_0 = 75$ km/s/Mpc. We selected from these samples all sources, where we found black hole mass estimates in the literature or by using the bulge velocity and the bulge/black hole mass relation from Merritt & Ferrarese (2001). Central velocity dispersion values were taken from Prugniel et al. (1998) and its update in the ‘Hypercat’ database or from Woo & Urry (2002). The black hole masses and fluxes are tabulated in Table 3.1.

Type/Name	Distance [Mpc]	M_{BH} [M_{\odot}]	$F_{5\text{GHz}}$ $F_{2-10\text{keV}}$ [mJy]	$L_{5\text{GHz}}$ [erg/s]	$L'_{3-9\text{keV}}$ [erg/s]	[erg/s]
SGR A*						
Quiet	0.008	$3. \times 10^6$	600.	2.2×10^{33}	2.3×10^{32}	6.3×10^{37}
Flare	0.008	$3. \times 10^6$	600.	1.0×10^{35}	2.3×10^{32}	2.87×10^{39}
LLAGN						
NGC2787	13.3	1.7×10^8		2.5×10^{-14}	1.66×10^{37}	3.93×10^{44}
NGC3147	40.9	6.58×10^8		3.7×10^{-12}	1.02×10^{38}	1.65×10^{48}
NGC3169	19.7	6.21×10^7		2.45×10^{-12}	1.55×10^{37}	3.76×10^{46}
NGC3226	23.4	1.39×10^8		7.6×10^{-13}	1.58×10^{37}	3.15×10^{46}
NGC4143	17.	3.1×10^8		3.1×10^{-13}	1.45×10^{37}	1.3×10^{46}
NGC4278	9.7	4.5×10^8		8.1×10^{-13}	8.13×10^{37}	1.49×10^{46}
NGC4548	16.8	1.83×10^7		1.6×10^{-13}	2.04×10^{36}	6.66×10^{44}
NGC4565	9.7	2.15×10^7		3.2×10^{-13}	1.41×10^{36}	5.07×10^{44}
NGC6500	39.7	1.15×10^8		$3. \times 10^{-14}$	7.94×10^{38}	3.08×10^{45}
FR I						
UGC00595	181.	2.31×10^8	93.	5.8×10^{-18}	1.82×10^{40}	5.84×10^{48}
NGC0383	67.8	5.11×10^8	92.	1.5×10^{-17}	2.53×10^{39}	4.02×10^{48}
UGC01841	86.4	1.78×10^9	182.	4.93×10^{-17}	8.13×10^{39}	5.85×10^{49}
NGC1218	116.	5.45×10^8	964.	2.38×10^{-16}	7.75×10^{40}	1.96×10^{50}
NGC1275	70.7	4.4×10^8	42400.	1.5×10^{-15}	1.27×10^{42}	3.86×10^{50}
NGC3862	82.8	4.9×10^8	200.	1.14×10^{-16}	8.2×10^{39}	4.39×10^{49}
NGC4261	29.6	1.19×10^9	308.	5.1×10^{-18}	1.62×10^{39}	5.16×10^{47}
NGC4374	14.8	8.11×10^8	180.	5.9×10^{-17}	2.36×10^{38}	1.09×10^{48}

Type/Name	Distance [Mpc]	M_{BH} [M_{\odot}]	$F_{5\text{GHz}}$ [mJy]	$F_{2-10\text{keV}}$	$L_{5\text{GHz}}$ [erg/s]	$L'_{3-9\text{keV}}$ [erg/s]	[erg/s]
NGC4486	14.8	1.71×10^9	4000.		3.9×10^{-16}	5.24×10^{39}	1.32×10^{49}
NGC5532	95.3	8.67×10^8	77.		3.4×10^{-18}	4.18×10^{39}	2.75×10^{48}
UGC09799	138.	2.48×10^8	391.		9.6×10^{-18}	4.45×10^{40}	5.92×10^{48}
NGC6166	122.	1.06×10^9	105.		$1. \times 10^{-17}$	9.35×10^{39}	1.56×10^{49}
NGC7236	105.	1.22×10^8	2.		9.1×10^{-19}	1.33×10^{38}	1.85×10^{47}
UGC12064	72.7	4.05×10^8	37.		1.8×10^{-17}	1.17×10^{39}	4.59×10^{48}
NGC7720	121.	1.22×10^9	270.		1.9×10^{-17}	2.37×10^{40}	3.29×10^{49}
XBLs							
0158+001	1270.	1.13×10^8	11.3		0.047	1.1×10^{41}	8.93×10^{50}
0257+342	1040.	5.36×10^8	10.		0.25	6.49×10^{40}	1.12×10^{52}
0317+183	792.	8.12×10^7	17.		0.36	6.39×10^{40}	2.03×10^{51}
0419+194	2260.	4.73×10^8	8.		0.09	2.44×10^{41}	1.71×10^{52}
0607+710	1130.	5.27×10^8	18.2		0.09	1.39×10^{41}	4.68×10^{51}
0737+744	1350.	1.16×10^9	24.		0.64	2.6×10^{41}	8.92×10^{52}
0922+745	2860.	7.12×10^9	3.3		0.044	1.62×10^{41}	1.2×10^{53}
1207+394	2750.	1.78×10^9	5.8		0.1	2.63×10^{41}	8.22×10^{52}
1221+245	914.	8.33×10^7	26.4		0.42	1.32×10^{41}	3.23×10^{51}
1229+643	680.	4.17×10^9	42.		0.55	1.16×10^{41}	5.51×10^{52}
1407+595	2180.	3.08×10^9	16.5		0.07	4.68×10^{41}	5.62×10^{52}
1534+014	1330.	8.01×10^8	34.		0.15	3.61×10^{41}	1.52×10^{52}
1757+703	1770.	6.92×10^8	7.2		0.18	1.34×10^{41}	2.85×10^{52}
2143+070	998.	3.13×10^8	50.		0.32	2.98×10^{41}	8.53×10^{51}

Type/Name	Distance [Mpc]	M_{BH} [M_{\odot}]	$F_{5\text{GHz}}$	$F_{2-10\text{keV}}$ [mJy]	$L_{5\text{GHz}}$ [erg/s]	$L'_{3-9\text{keV}}$ [erg/s]	[erg/s]
RBLs							
1418+546	629.	1.46×10^9		1220.	2.72	2.89×10^{42}	$1. \times 10^{53}$
1807+698	206.	2.67×10^{10}		1710.	7.85	4.36×10^{41}	3.24×10^{53}
2005-489	289.	1.48×10^9		1210.	9.85	6.03×10^{41}	7.71×10^{52}
2200+420	280.	1.71×10^8		2140.	8.65	1.01×10^{42}	1.12×10^{52}
2254+074	792.	4.82×10^8		560.	0.6	2.1×10^{42}	1.43×10^{52}

Table 3.1: Sources used in this chapter. Column 1 lists the names of the sources and column 2 gives the distance used to derive the luminosities from the fluxes. The black hole mass was calculated from the velocity dispersion relation Merritt & Ferrarese (2001). Column 4 and 5 give the measured radio and X-ray fluxes. For the LLAGN sample we only list the radio luminosity as directly taken from the original paper. The last two columns give the radio luminosity and the equivalent X-ray luminosity as described in Eq. (3.7). This luminosity has also been corrected for the different observed energy bands assuming a photon index of 1.6.

3.3.4 Results

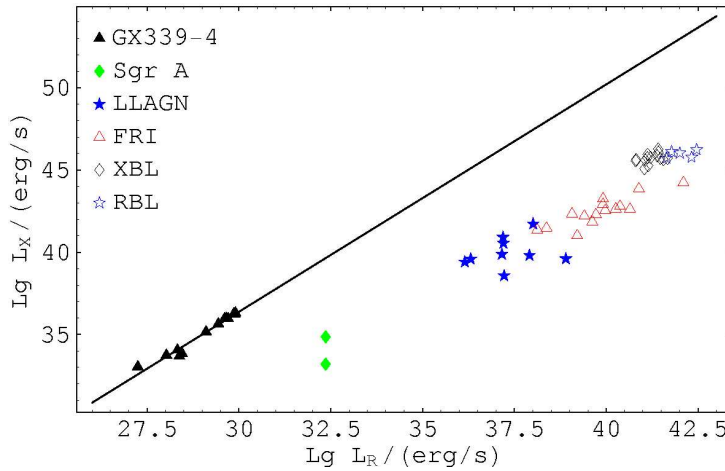


FIGURE 3.4— Radio/X-ray correlation for XRBs with our AGN sample. We only extrapolate the optical measurements of some AGN (FR I radio galaxies) to a corresponding monochromatic X-ray luminosity without a mass correction. For Sgr A* we show the quiescent and the flare spectrum. The solid line is the analytically predicted non-linear radio/X-ray correlation from the jet model, normalized for GX339-4. The supermassive black holes fall below the extrapolation from the X-ray binaries.

In Figs. 3.4 to 3.7 we show the radio and X-ray luminosities of the sources discussed above with various correction factors applied. Figure 3.4 shows the uncorrected data, with only optical luminosities extrapolated to corresponding X-ray luminosities. Clearly, the AGN fall well below the extrapolation of the radio/X-ray correlation of X-ray binaries. In other terms: by simply increasing the accretion rate in an X-ray binary one will never obtain the SED of an AGN.

In Fig. 3.5 we have included in the correlation the analytically predicted mass scaling (Eq. 3.7) but not yet the correction of the Doppler factor for BL Lacs. Surprisingly, with this simple scaling, all the source populations seem to be scaled by just the right amount to fall more or less on the predicted scaling with power from the XRBs with a relatively low scatter. This means that in the parameter space of X-ray luminosity, radio luminosity, and black hole mass, sub-Eddington black holes form a fundamental plane. It also suggests, that the theoretically motivated and predicted scaling seems to hold for stellar mass as well as supermassive black holes. We point out that two of the outliers (NGC6500 and NGC1275) are known from high-resolution VLBI

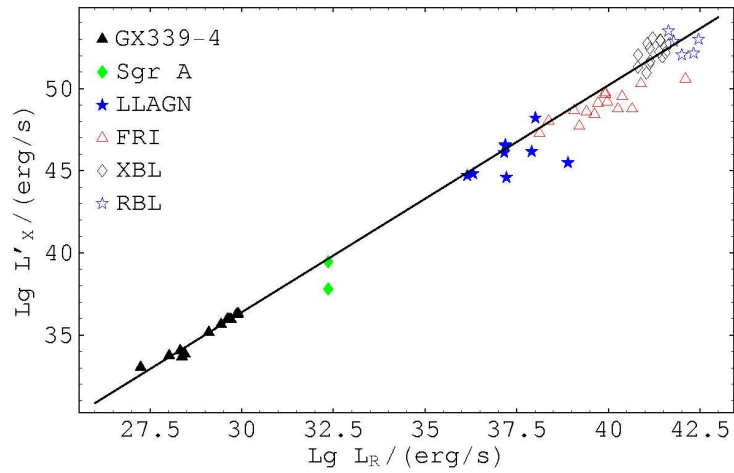


FIGURE 3.5— The same as Fig. 3.4 but for an equivalent X-ray luminosity, L'_X , which has been individually corrected for the mass factor and scaled to the value the X-ray luminosity would have for a central black hole of only $6 M_\odot$, as in GX339-4 (see Eq. 3.7). Corrections for Doppler factors have not been applied.

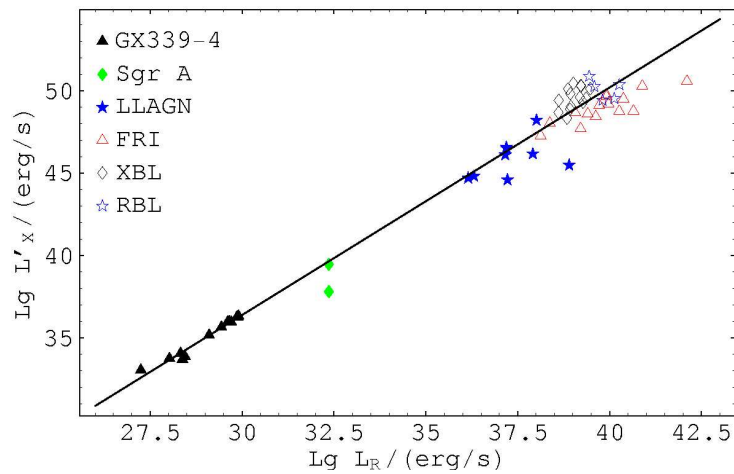


FIGURE 3.6— The same as Fig. 3.5 but the radio and X-ray luminosities of BL Lac objects have been corrected for Doppler boosting. As discussed in the text, this mainly moves BL Lacs along the correlation and they now occupy the same region as FR Is – their parent population within the inclination-based unified scheme.

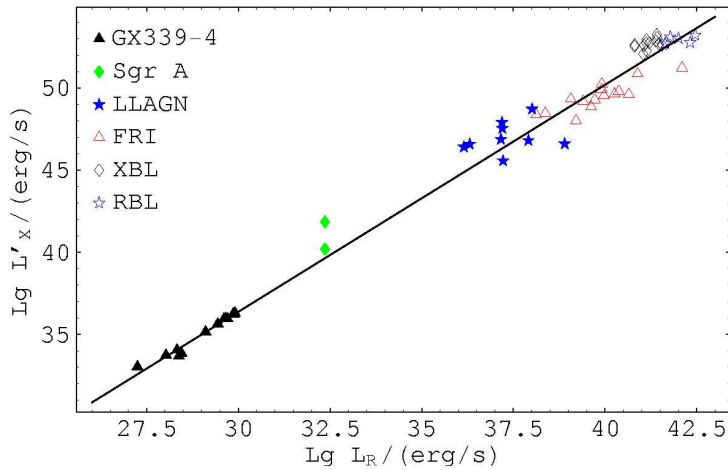


FIGURE 3.7— Radio/X-ray correlation for XRBs and AGN, where the X-ray flux of all AGN has been increased by a constant value of 10^7 , corresponding to an average AGN mass of $3 \times 10^9 M_{\odot}$.

observations to have radio cores that are significantly affected by extended emission (Falcke et al. 2000; Walker et al. 2000) and hence appear too bright in the radio. The same may be true to some degree for FR Is in general, but should be negligible for BL Lacs.

Figure 3.6 demonstrates the effect of a Doppler factor correction. As discussed in the previous section, the X-ray/radio-ratio is rather insensitive to the Doppler factor and sources will mainly move along the correlation. In our case the BL Lacs are pushed from the upper end of the correlation into the regime where FR I radio galaxies lie. Given that BL Lacs are supposed to be the beamed population of FR I radio galaxies within the inclination-based unified scheme, this seems to be an appropriate correction and provides further support for that scheme.

Finally, in Fig. 3.7 we show the radio and X-ray luminosities, where the X-ray flux has been corrected by a constant factor 10^7 , thus ignoring the individual mass estimates. With this factor the radio/X-ray correlation can also be continued to AGN. Scaling by 10^7 is identical to assuming a constant black hole mass of $\approx 3 \times 10^9 M_{\odot}$ for all objects. The black hole mass of FR I Radio Galaxies and BL Lac objects scatter around this value. LLAGN have an average mass of somewhat less than $10^9 M_{\odot}$, thus in comparison with Fig. 3.6, the LLAGN have higher X-ray fluxes. The Galactic black hole (Sgr A*) has a

mass of only $3 \times 10^6 M_{\odot}$ so the X-ray flux is increased too much and the X-ray flare state – which may in fact contain the here crucial non-thermal power law – lies above the extrapolation.

A better distinction of the mass effects might be possible with the inclusion of more low mass AGN. Another conclusion is that, for example, a linear dependency of the X-ray/radio-ratio with mass would not be appropriate and over-correct the data.

3.4 Mass Estimates from the Radio/X-Ray Correlation

Having established the radio/X-ray correlation from XRBs to AGN, it is tempting to use this as a tool to obtain crucial parameters like the black hole mass. Unlike many other possibilities to derive the black hole mass (like the bulge/black hole mass relation) we only need two parameters, the flat spectrum radio flux and the X-ray flux. If we assume that the correlation is exactly fulfilled we can derive the black hole mass from eq. (3.7). The result is shown in Fig. 3.8.

If one includes all datapoints (XRBs and AGN) the correlation of both mass estimations are correlated with a correlation coefficient of 0.95. According to a Student-T test the probability that such a correlation is random is less than 0.05 percent. However, if one excludes the XRBs and SGR A* from the sample, the correlation coefficient drops to 0.18 and the correlation is insignificant as it is only a 1σ result. A tight correlation for AGN can not be expected, as we have seen in Fig. 3.7 that the radio/X-ray correlation does not look very differently if one assumes a constant mass for all AGN. The scatter due to relativistic beaming or other effects is at least of comparable size as the mass dependence within the "small" range of AGN black hole masses considered here. A mass estimate through the radio/X-ray correlation for AGN is therefore not very promising. But it will probably be possible to distinguish between a stellar mass black hole of $10 M_{\odot}$ and an intermediate black hole of $10^4 M_{\odot}$ or an AGN. The mass differences are in this case so large, that they should be observable even with the unavoidable scatter. The method will be used later on to analyze Ultra-luminous X-ray sources.

3.5 Conclusion and Discussion

We have suggested that black holes operating at sub-Eddington accretion rates make a transition to a radiative inefficient state, where most of the emission is largely dominated by the non-thermal emission of a jet ("JDAFs"). In this

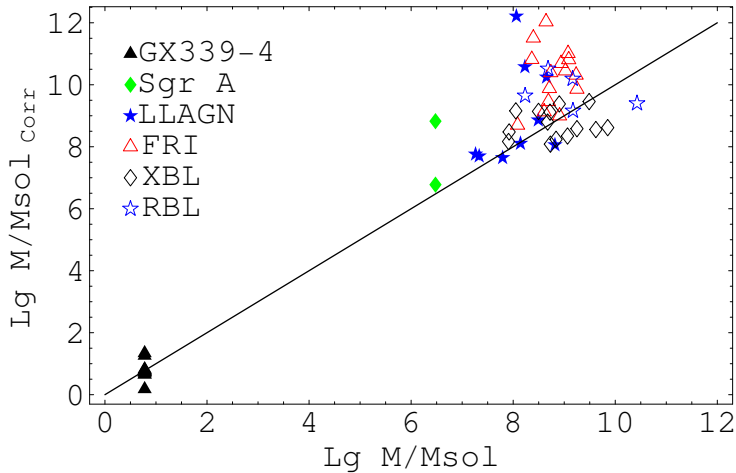


FIGURE 3.8— Black hole mass derived from the radio/X-ray correlation vrs. measured black hole mass. The solid line denotes that both methods yield the same result.

picture the radiative output of sub-Eddington black holes is non-thermally dominated, while near-Eddington black holes are thermally dominated. This scheme allows one to unify the radiative properties of black holes over a large range of accretion powers. At sub-Eddington accretion rates, the scaling between radio and optical or X-ray cores is then predicted to follow the scaling laws outlined in Falcke & Biermann (1995) and Markoff et al. (2003). This requires taking the black hole mass into account.

Near-Eddington black holes are presumably found in quasars, luminous Seyfert galaxies, and soft-state X-ray binaries which are considered to be in the high state. As pointed out elsewhere (Pounds et al. 1995; Maccarone et al. 2003) Narrow-Line Seyfert 1s may also be related to the very high state of X-Ray binaries.

On the other hand, candidates for sub-Eddington black holes are XRBs in the low-hard state, Sgr A*, LINERs, FR I radio galaxies, and BL Lac objects. In terms of beaming and inclination-based unified schemes, which we do not explicitly discuss but consider valid. It may be worth pointing out that ultra-luminous X-ray sources might be low-mass analogs to BL Lacs and blazars as discussed in the next section or (Körding et al. 2002).

Using various samples of sub-Eddington black holes, we are able to show that all these different types of sources seem to fall near the predicted radio/X-

ray correlation, if the scaling with black hole mass is taken into account.

The crucial underlying assumption is that all these latter sources are intrinsically jet-dominated and have essentially the same SED in common: a flat, optically thick radio spectrum and an optically thin power law beyond a turn-over frequency. Shape and scaling of the SED needed to explain the radio/X-ray correlation is just what one expects in a pure jet model and supports the notion of jet-dominated accretion flows (“JDAF”). On the other hand, some form of radiative inefficient accretion flows/corona is also clearly needed for this picture to work, since there is always a need for a power and matter source for the outflow. It may be possible to adapt the scheme for a situation where the X-ray emission is dominated by emission from optically thin accretion flows, if their X-ray flux follows a similar non-linear scaling as predicted in the jet case.

An interesting corollary for jets is that, in order to obtain the scaling with mass, one has to assume that the region of the onset of particle acceleration in the jet – producing the optically thin power law – is always around a fixed location in mass-scaled units ($\sim 100 - 1000R_g$).

With the large range of black hole powers and masses discovered the proposed picture may warrant further investigation and detailed tests. If solidified and further evolved it may help to predict the luminosity evolution of black holes at various wavebands over many orders of magnitude.

4

Ultra-Luminous X-ray Sources

4.1 Introduction

Ultra-luminous X-ray sources are among the most widely discussed objects, but their true nature is yet unknown. These objects have X-ray luminosities around $L_X \sim 10^{39-42}$ erg/s which seems too bright for normal black hole X-Ray binaries (BHXRBS) but far dimmer than normal Active galactic nuclei (AGN). The first hints to these intermediate-luminosity X-ray point sources have been found in the 1980s (Fabbiano 1989; Colbert et al. 1995). ROSAT and subsequent high resolution X-ray satellites confirmed these findings and showed that these intriguing sources are often not in the centers of the galaxies (Colbert & Mushotzky 1999; Roberts & Warwick 2000). More recent surveys (see e.g., Colbert & Ptak 2002) find approximately one ULX in every five galaxies confirming that ULXs are a common phenomenon.

The Eddington limit for an accreting object with mass M is $L_{\text{Edd}} \approx 1.25 \times 10^{38} \frac{M}{M_\odot} \text{erg s}^{-1}$, which implies that these sources are super-Eddington for stellar mass objects. Some ULXs show spectral transitions from a soft spectrum to a hard power law and luminosity variability (e.g. Mizuno et al. 2001; Kubota et al. 2001), ruling out supernova remnants and supporting the idea that ULXs can be attributed to accreting black holes.

To achieve the observed X-ray luminosities with isotropically radiating accretion disks should require a population of intermediate-mass black holes (IMBHs) of $50 - 500M_\odot$. The existence of IMBHs would be extremely exciting, as they could be the 'missing link' between stellar mass black holes and the supermassive black holes in the center of the galaxies (see e.g., Ebisuzaki

et al. 2001). Such objects would have important implications for Cosmology and arise in many theories on the collapse of primordial stars. There is also an ongoing discussion whether the inner disk temperatures of ULXs are too high for IMBHs, for high temperatures similar to the values found in XRBs (see e.g., Colbert & Mushotzky 1999; Mizuno et al. 1999; Makishima et al. 2000). However, recent XMM observations often find lower inner disk temperatures, compatible with IMBHs, than earlier ASCA observations (see e.g. Miller et al. 2003).

While there is some evidence that a few of these objects might indeed be intermediate mass black holes (IMBH, e.g., Strohmayer & Mushotzky 2003), the creation and feeding mechanisms for black holes of this size are totally unknown. The phenomenon seems to be connected to star formation, see e.g., the cartwheel galaxy (Gao et al. 2003). This galaxy would need hundreds to thousands of IMBHs feeding from a yet unknown non-stellar mass reservoir or the ULX phenomenon is connected to high mass XRBs (King 2004). Grimm et al. (2002); Gilfanov (2004) show the existence of a universal X-ray luminosity function that may extend up to ULXs, if one takes the star forming rate into account. There seems to be a dependence of the ULX abundance on the galaxy type, especially dwarf galaxies host many nearby ULXs.

These problems with isotropic emission models have already been discussed by King et al. (2001), where the authors propose some form of anisotropic emission as an alternative. A beaming factor of ten already reduces the required mass of the black holes to "normal" stellar values, but this is difficult to achieve with pure disk models. In this thesis we suggest that the spectrum of some XRBs could be explained by a coupled disk/jet model (see also Markoff et al. 2001a), where some of the X-ray emission is produced by synchrotron and inverse-Compton radiation in a jet. This emission would naturally be relativistically beamed. Mirabel & Rodríguez (1999) (see also Reynolds et al. 1997) have pointed out that a number of nearby galaxies should host microblazars - microquasars with relativistically beamed jets pointed towards the observer. In this chapter we will investigate whether such populations of microblazars or intermediate mass black holes can indeed explain current data on ULXs and constrain the basic parameters required for these models. This chapter is based on Körding et al. (2002). In the next chapter we will explore if these potential microblazars also show compact radio emission like Blazars.

4.2 Simple Models

4.2.1 The Jet/Disk Model

As discussed in chapter 1 & 3, black hole XRBs can exist in several states, the two most distinct of which are a high/soft state where the observed spectrum is soft and thermally-dominated, and a low/hard state dominated by a non-thermal hard power law spectrum (e.g. Nowak 1995). Which state an XRB is in seems to depend on the accretion rate. One scenario for the evolution of XRBs is that the inner part of the accretion disk consists of an optically thin, advection-dominated accretion flow (ADAF) existing up to a transition radius where the accretion flow turns into a standard (Shakura & Sunyaev 1973) optically thick disk (Esin et al. 1997). The low/hard state seems to be accompanied by persistent radio jets with optically thick synchrotron emission extending up to the optical and near-infrared (Fender 2001). Synchrotron and inverse Compton emission from the jet could also be produced in the X-rays for low/hard and high/soft states (Markoff et al. 2001a; Markoff et al. 2001b).

For a self-consistent population synthesis model, we will have to take the jet and the disk separately into account. For simplicity we make some assumptions in order to calculate the relative importance of the two processes for the overall distribution of XRBs. These are:

- We only consider two main populations: neutron stars of mass $1.4M_{\odot}$ and black holes within a mass range of 5-15 M_{\odot} , where we fix the amount of active black holes ($> 5 \times 10^{36} \text{erg s}^{-1}$) to 13% of the number of active neutron stars (e.g. Tanaka & Lewin 1995).
- While the spectral states are defined only for black holes, for simplicity we apply them also to neutron stars, and consider only the low/hard and soft/high states.
- The probability that a given XRB has the accretion rate \dot{M} is given by $\mathcal{W}(\dot{M}) \sim \dot{M}^{\xi}$ which we assume as a power law with a cutoff representing the Eddington limit.
- The distribution of accretion rates and basic jet parameters are assumed to be identical for neutrons stars and black holes.
- Soft X-ray emission is produced by an isotropically radiating disk and a relativistically beamed jet as discussed below.

The crucial point for a simple population synthesis model including jet emission is how a specific accretion rate translates into an X-ray luminosity. Here we assume that the transition between the low and the high state happens at a critical accretion rate \dot{M}_C and the luminosities scale as follows: above \dot{M}_C the disk luminosity increases linearly with \dot{M} as expected for a standard accretion disk. Below \dot{M}_C , the disk luminosity increases with \dot{M}^2 as expected for optically thin ADAFs (Narayan & Yi 1995; for a constant α -parameter). Assuming that the jet power scales linearly with \dot{M} , the optically thin jet synchrotron emission will scale roughly as $L_{x,\text{jet}} \propto \dot{M}^{1.8}$ (chapter 2 & 3). In the original paper K rding et al. (2002) we have assumed that the optically thin emission scales roughly like the optically thick jet emission, which scales with $\dot{M}^{1.4}$. This difference will not play an important role for the predicted ULXs population, as we will see below. At high accretion rates the scaling must break down when a significant fraction of the jet power is radiated away. In this phase we assume that the radiated power can only increase linearly with jet power (see Sect. 2.5.4). In the jet model of Markoff et al. (2001a) and Markoff et al. (2001b) this happens in the high state, roughly at $\dot{M} > \dot{M}_C$, where the jet is inverse-Compton cooled (radiating soft X-rays) by scattered photons from the accretion disk or a yet unknown mechanism for quenching the jet. However, since models for the contribution of jets to the high state of XRBs are not yet very well developed, we simply fix the luminosity of the jet at $L_{\text{jet}} = \eta_j L_{\text{disk}}$ at \dot{M}_C , where η_j is a free parameter.

Hence, we use the following simple parameterization for the soft X-ray luminosity of accretion disk and jet:

$$\begin{aligned} L_{\text{disk}} &= \begin{cases} \epsilon \left(\frac{\dot{M}}{\dot{M}_C}\right) \dot{M} c^2 & \text{if } \dot{M} < \dot{M}_C \\ \epsilon \dot{M} c^2 & \text{if } \dot{M}_C < \dot{M} < \dot{M}_{\text{Edd}} \end{cases} \\ L_{\text{jet}} &= \begin{cases} \eta_j \epsilon \left(\frac{\dot{M}}{\dot{M}_C}\right)^{0.8} \dot{M} c^2 & \text{if } \dot{M} < \dot{M}_C \\ \eta_j \epsilon \dot{M} c^2 & \text{if } \dot{M}_C < \dot{M} < \dot{M}_{\text{Edd}} \end{cases} \end{aligned} \quad (4.1)$$

In the following we set the radiative efficiency of the standard accretion disk to the canonical value of $\epsilon = 0.1$. For a given mass M the parameter \dot{M}_{Edd} has been chosen such that the luminosity of the disk and the jet integrated over all angles is equal to L_{Edd} . For simplicity, the mass distribution of black holes is given by $dN/dM = \mathcal{V}(M) = \text{const.}$

For a bulk Lorentz factor of the jet of $\gamma_j > 1$ the jet emission depends

on the angle to the line of sight as given by Lind & Blandford (1985). If the emission in the rest frame of the jet follows a power-law with spectral index α , the observed emission is proportional to $\delta^{2+\alpha}$, where the Doppler factor $\delta = \frac{1}{\gamma_j(1-\beta \cos \Theta)}$. The probability of seeing an object with an emission exceeding L when in the rest frame the jet emits L_{loc} is:

$$P(L, L_{\text{loc}}) = \frac{1-\beta}{\beta} \left(\left(\frac{L_{\text{max}}}{L} \right)^{\frac{1}{2+\alpha}} - 1 \right)$$

where $L_{\text{max}} = \delta^{2+\alpha}(\Theta = 0)L_{\text{loc}}$ is the maximum possible emission. To derive this we only consider the jet component pointing towards us and then integrate over all inclination angles. Since we only discuss jets with $\gamma_j > 2$, the emission of the counter-jet is largely negligible.

With this parameterization, the contribution of a single population of XRBs at a given accretion rate and mass has three parameters ($\gamma_j, \dot{M}_C, \eta_j$), which are reasonably well constrained by the underlying models. Observations of microquasars show that the typical Lorentz factors are in the range $\gamma_j \simeq 2 - 5$ (Mirabel & Rodríguez 1999; Fender et al. 1999). The typical values for the critical accretion rate discussed in the literature are around $\dot{M}_C \sim 0.1$ (Narayan & Yi 1995) and we keep this parameter fixed. The jet efficiency can in principle be fairly high, but probably $\eta_j \lesssim 0.3$ (Falcke & Biermann 1995 & 1999).

At high accretion rates, the jets emits a factor η_j less radiation in its rest frame compared to the disk, but beaming will lead to an amplification of the jet with respect to the disk for small inclination angles. Beaming is strongest for sources whose jets point within the beaming cone with half-opening angle of $1/\gamma_j$ towards the observer. For example, already $\gamma_j = 3$ will beam the jet component in a fraction of 5.5% of the binaries by a factor of 20. This is more than enough to make up for the less efficient emission mechanism. For $\gamma_j = 5$ a fraction of 2% binaries are beamed by a factor of 77. Therefore, in the low-luminosity regime ($\ll \epsilon \eta_j \dot{M}_C$) jets should dominate (because of low radiative efficiency of ADAFs), and again dominate in the super-Eddington regime due to beaming. In the intermediate regime up to L_{Edd} , the disk will be more prominent.

Now we can calculate a synthetic $\log N - \log L$ distribution for our model. The emission from the disk and the jet is described by Eq. (4.1). To reach a given luminosity L , only the difference $L - L_{\text{disk}}$ has to be reached by the jet due to boosting. The estimated number of sources with a luminosity greater

than L is given by:

$$N(L) = \sum_{i=N,B} \mathcal{N}_i \int dM \int d\dot{M} \mathcal{V}_i(M) \mathcal{W}_i(\dot{M}) \cdot P(L - L_{\text{disk}}(\dot{M}), L_{\text{jet}}(\dot{M})) \quad (4.2)$$

where the sum goes over the two populations.

4.2.2 The Disk-Only Model

Of course, with the model discussed above we can also investigate the alternative scenario, that the soft X-ray emission originates only from the accretion disk, by setting $\eta_j = 0$. In this case we have to leave the upper end of the black hole mass distribution and its power law index as a free parameter to obtain the high luminosities observed, and we have $dN/dM = \mathcal{V}(M) \propto M^\zeta$.

With the isotropic disk emission the estimated number of sources with a luminosity greater than L is given by:

$$N(L) = \sum_{i=N,B} \mathcal{N}_i \int dM \int d\dot{M} \mathcal{V}_i(M) \mathcal{W}_i(\dot{M}) \cdot \Theta(L - L_{\text{disk}}(\dot{M})) \quad (4.3)$$

where Θ is the usual step-function.

4.3 Data

To put meaningful constraints on a beaming model it is essential to compare the low-luminosity (un-beamed) parent population with the high-luminosity (beamed) population. However, the published X-ray population of a single galaxy has only marginal statistics in the high-luminosity regime. To get a more general X-ray population in the low-luminosity regime up to $\approx 5 \times 10^{38}$ erg/s, we combine data from the galaxies M101, M31 and M82 (Pence et al. 2001; Di Stefano et al. 2002; Griffiths et al. 2000). These are three close ($D < 10$ Mpc) galaxies with good published Chandra data. To get better statistics at higher luminosities, we used the luminosity function compiled by Roberts & Warwick (2000) from ROSAT data of 49 spiral galaxies from the XHFS-sample. The host galaxy types are spiral with the exception of the irregular M82. However this does not seem to make a significant difference (see Fig. 4.1).

To avoid incompleteness near the detection limit, for each data set we only use X-ray sources with a luminosity of ten times the respective detection threshold. Chandra has a different bandpass (0.3-10 keV) than ROSAT (0.1-2.2 keV), so we extrapolated the ROSAT-luminosities to the 2-8 keV band. If the photon index is not fitted directly we used a common powerlaw with $\Gamma_{\text{ph}} = 1.7$. In some cases different values for N_H were used which we did not correct. According to Di Stefano et al. (Di Stefano et al. 2002), variations of $N_H = 0.6 - 1.5 \times 10^{21} / \text{cm}^2$ and $\Gamma_{\text{ph}} = 1.2 - 2$ give differences in luminosity of about 20% which are not really significant in the log(N)-log(S) plots shown here and should be statistically distributed (for ROSAT data the differences are higher).

As a reference galaxy we take M101, to which we scale the populations of the other galaxies (i.e., the total number of sources in the overlapping luminosity bins). Combining these data sets assumes that the overall shape of the luminosity distribution is roughly universal, which has been shown by Grimm et al. (2002); Gilfanov (2004). Clearly, the overall number of XRBs in each galaxy can depend strongly on the age of recent star formation, but the average slope of the luminosity function should be less sensitive to this. Since M82 is irregular and has a much higher star forming rate than M101 or M31, we also show the data excluding M82, which is not significantly different.

To calculate errors we assume a standard deviation from the 'general population' of \sqrt{N} where N is the number of detected sources, and use normal error propagation. Because we are showing a cumulative distribution, the errors for each point are not independent.

4.4 Results

To compare our simple model with the data we evaluate the integrals in Eqs. (4.2 & 4.3) numerically. The absolute normalization and the parameter ξ , which are entirely free, have been fit to the data at $L_x \leq 10^{37} \text{erg s}^{-1}$. We obtain a best-fit value of the accretion rate index $\xi = 1.4$ (note that the luminosity scales as \dot{M}^2 in this regime). As we only model neutron stars and black holes, the model fits could be affected at lower luminosities by other source populations like accreting white dwarfs and supernova remnants.

Fig. 4.1 shows the result for our best-fit jet/disk model which requires $\gamma_j = 5$ and $\eta_j = 0.3$, for the combined data set discussed above. Additional to the XHFS sample we show recent chandra detections of ULXs by Swartz & Tennant (2003). Those new results are in agreement with the older sample. The Eddington limit for black holes (limited to $M < 15M_{\odot}$) and neutron stars

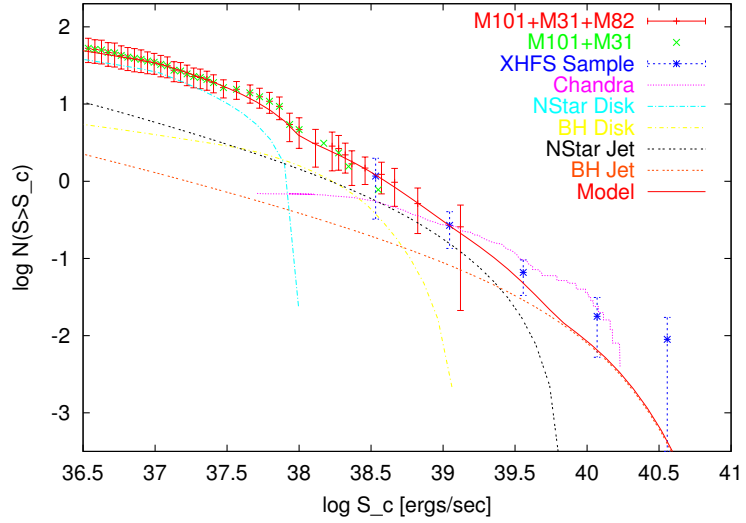


FIGURE 4.1— Comparison of our model of the luminosity function with the data. The parameters are $\gamma_j = 5$, $\eta_j = 0.3$, $\dot{M}_C = 0.1$, $\xi = 1.4$. Also shown are the individual contributions of the disk and the jet for neutron stars and black holes.

shows up as breaks at the respective luminosities, and jets with $\gamma_j = 5$ are able to produce emission up to $10^{40} \text{ erg s}^{-1}$ in significant numbers. The model is most sensitive to γ_j and η_j . Because the high luminosity domain depends linearly on η_j while its dependence on γ_j goes as $\gamma_j^{2.7}$, a slight decrease of γ_j can be compensated by an increase of η_j and vice versa. For $\gamma_j = 5.8$ or $\gamma_j = 7.5$ we can find $\eta_j = 0.2$ or $\eta_j = 0.1$, but the fit gets progressively worse at higher Lorentz factors. Demanding $\eta_j \lesssim 0.3$ for the radiative efficiency of the jet sets a lower limit for $\gamma_j \gtrsim 5$.

For the disk-only model, the sensitive parameters are the power law indices of the accretion rate and the mass distribution of the black holes. To fit the data, a mass distribution index of $\zeta \simeq 2$ is needed. The index of the accretion rate is the same as before (1.4), because the lower luminosities in the jet/disk model are also dominated by the disk. To explain the most luminous sources, the upper end of the black hole mass distribution must be extended at least up to $1000 M_\odot$. The results of the fit are shown in Fig. 4.2. For the lower luminosities the neutron stars dominate the luminosity function, while the black holes dominate at higher luminosities.

In Fig. 4.3 we show the contributions from low and the high state objects

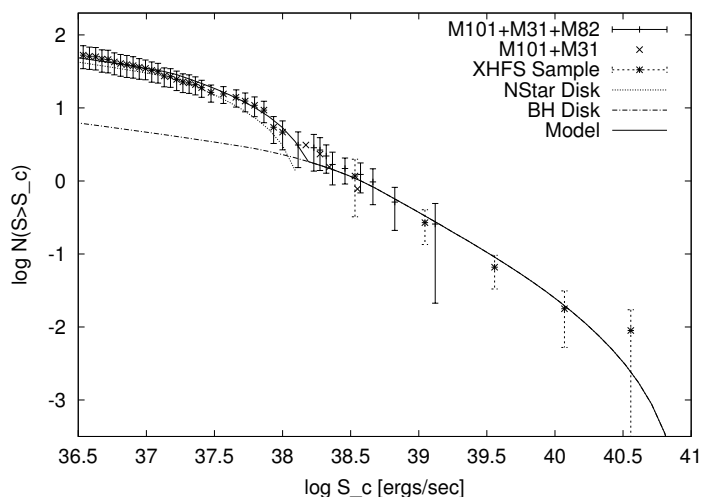


FIGURE 4.2— Model with intermediate-mass black holes up to $1000M_{\odot}$ and a mass distribution with power law index $\zeta = 2$.

separately. The ULX population is mainly created by beamed emission from high state objects. Thus, the explanation for ULXs due to beamed emission depends on the strength of the jet for very strongly accreting objects. For high state objects one usually finds no visible jet, in the very high state the jet often reappears (GRS1915+105: Mirabel et al. 1997). The jet emission from low/hard state objects does not contribute significantly to the overall XRB population for high luminosities ($> 10^{38}$ erg/sec). This finding also shows that the difference between the jet scaling for the low state used in Körding et al. (2002) and the scaling with $\dot{M}^{1.8}$ does not alter the conclusions of the paper.

4.5 Summary and Discussion

Using two very simple models for the evolution of XRBs, we calculate the luminosity distribution of X-ray point sources in nearby galaxies. We consider a jet/disk model based on Falcke & Biermann (1999) and Markoff et al. (2001a), which can give rise to relativistically beamed emission from microblazars. Alternatively we also consider a purely isotropically radiating disk model.

Both models can in principle reproduce a combined luminosity function compiled from X-ray point source catalogues of three close galaxies and the XHFS spiral galaxy sample. However, as expected, the isotropic disk model

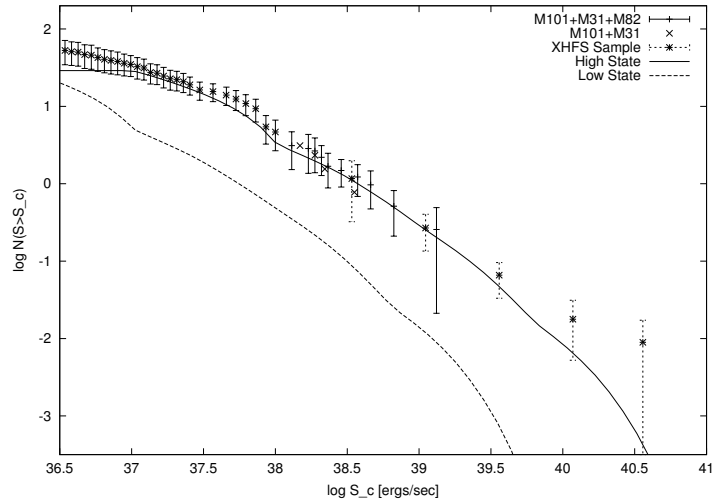


FIGURE 4.3— Contribution of the Low and the High state. This plot has been created using a jet scaling in the low/hard state of $\dot{M}^{1.4}$.

requires a mass distribution of black holes extending out to $1000M_{\odot}$ to explain the ULXs. On the other hand, a relativistic jet/disk model can fit the data with stellar mass black holes, if X-ray emitting jets with Lorentz factors $\gamma_j \simeq 5$ are present in XRBs. In addition, a fraction of $\eta_j = 10 - 30\%$ of the total soft X-ray emission has to come from the jet rather than the accretion disk for an un-beamed XRB in the high state. This requires rather powerful jets but is not completely unreasonable. If only a fraction of the XRBs have relativistic jets, a slightly higher Lorentz factor or jet efficiency is needed. Boosting a 10 mJy Galactic XRB by a factor $\sim 10^2$ (for $\gamma \sim 5$) and placing it at $D \sim 3\text{Mpc}$ would yield only a faint $10 \mu\text{Jy}$ source and make radio detections difficult. The possibility of radio detections will be further discussed in the next chapter.

With the current statistics it is not possible to distinguish between the two different models, but it seems that microblazars provide at least a sensible alternative to the often discussed intermediate mass black hole scenario. Monitoring the spectral variability of the most luminous sources and further developing the XRB jet model should eventually help to disentangle the two scenarios.

5

Radio Observations of ULXs

5.1 Introduction

In the previous chapter we have shown that the ULX phenomenon can – at least partially – be explained by emission from relativistic jets (microblazars). Besides this, other explanations have been proposed: anisotropic emission (King et al. 2001), and super-Eddington accretion flows (Abramowicz et al. 1988; King 2004). One possibility to distinguish between the microblazar model and the other possibilities is the detection of compact, luminous radio cores at the positions of ULXs. If the jets also emit in the radio regime like XRBs in the hard state (Markoff et al. 2001a) or the very high state (see e.g., GRS 1915 Rodriguez et al. 1995), the radio emission is also boosted and may be observable. This chapter is based on Körding, Colbert, & Falcke (2004, in prep).

XRBs in the very high state are probably the nearest sources to ULXs in our galaxy, of those GRS 1915+105 can be seen as the prototype of a very high state object. GRS 1915+105 shows bright radio flares of 1.5 Jy while the quiescent value is approximately 130 mJy (Rodriguez et al. 1995). An other highly variable XRB is Cyg X-3. While this source is also found in the low and high state, it shows major radio flares with a flux increase of a factor 10-100 on a time scale of a day which lasts for days or weeks (Ogley et al. 2001). Therefore, it has to be expected that also ULXs could be radio transients. These relativistically boosted radio flares could be detectable with the VLA. In addition, these observations can be used to estimate the number of radio flares created in a galaxy. Such estimates are important for the design of new digital radio telescopes such as LOFAR or the SKA, as they could easily

search for transients due to their multi-beam capabilities.

In this chapter we describe a systematic search for steady state radio emission or radio flares of a well defined sample of ULXs. In Sect. 2 we present our observation scheme and show our results in the next section. The theoretical implications are discussed in Sect. 4. Our conclusions are given in Sect. 5. Finally we discuss the low luminosity AGN NGC 4736 in the appendix of this chapter.

5.2 Observations

5.2.1 Sample Selection

The Chandra catalog of ULXs, created with the same pipeline as the Colbert & Ptak (2002) ROSAT catalog, contains all ULXs ($> 10^{39}$ erg/sec) found in the public Chandra and ROSAT data at the time when the observations were proposed. In order to find a sample, which is as unbiased as possible, we selected all sources of the catalog with $\text{DEC} > -20^\circ$ and restricted the distance to be < 5.5 Mpc. The distance limit was mainly used to reduce the sample size. A low distance also helps to give low limits on the total emitted radio power of the sources. This selection results in nine ULXs in seven fields of views (FOVs): M33, NGC 2403, M82 (3 ULXs), NGC 4736 (2 bright point sources, one may be the nucleus), NGC 5204, and two fields in NGC 5457 which is also known as M101. The positions of the ULXs are shown in Table 5.1. Besides M82, which is classified as dwarf/irregular, all other host galaxies are spirals.

5.2.2 Observing Scheme

The goal of these observations is the search for radio flares and continuous emission of ULXs. The seven selected fields were observed eight times for approximately four hours between June and October 2003 with the VLA. This results in 34 minutes per source and epoch including the calibration scans. After the last epoch the data of all epochs was combined to give deep observations to search for continuous emission. To avoid confusion the observations were obtained when the VLA was in A or B configuration.

The optimal receivers at the VLA to search for weak, flat spectrum point sources are the X-band receivers. They are more sensitive than the C and U Band receivers in the VLA, so they are preferable for a detection as long as the spectrum is flatter than a spectral index of 0.4. We expect that the ULXs have flat or even inverted spectrum which could be detectable if they are beamed. Thus, we typically observed at 8.4 GHz using the maximal bandwidth of 50

TABLE 5.1— Positions of the observed ULXs and their 2-10 keV X-ray Luminosities. In the fields with only one ULX, the radio observations have been pointed at the ULX. In M82 the center of the field was on the second source (M82-D), in field of NGC 4736 was centered at the middle of both sources.

Name	RA	DEC	Lum. $\left[\frac{\text{erg}}{\text{s}}\right]$
M33	01 33 50.9	+30 39 38.00	1.04×10^{39}
NGC 2403	07 36 25.5	+65 35 40.00	1.73×10^{39}
M82-A	09:55:51.03	+69:40:45.13	6.4×10^{39}
M82-D	09:55:50.15	+69:40:46.48	3.33×10^{39}
M82-F	09:55:46.59	+69:40:40.94	1.25×10^{39}
NGC 4736-1	12 50 53.1	+41 07 13.30	9.36×10^{38}
NGC 4736-2	12 50 53.3	+41 07 14.00	1.34×10^{39}
NGC 5204	13 29 38.6	+58 25 05.60	2.34×10^{39}
NGC 5457-1	14 03 32.4	+54 21 03.00	1.61×10^{39}
NGC 5457-2	14 04 14.3	+54 26 03.80	1.45×10^{39}

MHz. Due to the distribution of the right ascension of our sources we have to observe them in two time slots, for the exact dates see Table 5.2.

As we are searching for very weak radio emission, we obtained phase-referenced observations. For all sources VLA phase-calibrators could be found within 10° , typically within 5° of the target source. The cycle time between calibrator and source was approximately 7 minutes. The phase correction between subsequent calibrator scans was mostly below 40° on the longest baselines, while the phase corrections on the shorter baselines are normally below 10° . Therefore, the phase calibrated images should only be degraded by a few percent due to phase errors. Amplitude calibration has been done using either 3C286 or 3C48. The phase-calibrated data has then been imaged with natural weighting to achieve the maximal sensitivity. In each epoch every source was observed for approximately 21 minutes, excluding phase and amplitude calibrator observations.

For M82 we have also reanalyzed archival data from Kronberg & Sramek (1985), as they have reported a radio flare of 7.07 mJy in M82. Intriguingly, the position of the flare is near the brightest ULX in this galaxy. This flare was observed with the VLA in A-configuration using C-band receivers.

TABLE 5.2— Observing Dates of the different Epochs. In the first time slot we observe M33, NGC 2403, M82, and NGC 4736, in the second NGC 4736, NGC 5204, and the two FOVs in NGC 5457.

Epoch	First Slot	Second Slot	Configuration
1	2 June	4 Jun	A
2	3 July	3 July	A
3	28 July	5 July	A
4	18 Aug	17 Aug	A
5	7 Sep	30 Aug	A or AnB
6	15. Sep	15. Sep	AnB
7	03 Oct	07 Oct	AnB
8	16 Oct	18 Oct	B

TABLE 5.3— RMS flux values for the different FOVs. Besides the RMS of each epoch we give the RMS value for map of the combined dataset. All values are given in μJy .

Epoch	1	2	3	4	5	6	7	8	comb.
M33	37	36	37	37	60	41	71	54	17
2403	31	30	32	31	59	38	45	37	13
N5457I1	33	32	31	35	35	39	77	46	14
N5457I2	32	32	34	37	33	35	75	34	13
N5204	35	33	31	35	34	37	51	38	13
N4736	45	47	49	55	45	61	63	62	21

5.3 Observational Results

5.3.1 Error Limits

The root mean square (rms) flux values of the observed sources have been calculated from natural weighted maps. For fields with detected sources the largest possible rectangular field excluding the source has been used to calculate the rms. The theoretical rms value for a 21 minute observation is, according to the VLA Observational Status Summary (Taylor et al. 2004), $31 \mu\text{Jy}$. The rms flux values of the individual epochs and fields are shown in Table 5.3. In a single epoch the typical observed rms is about $35 \mu\text{Jy}$. If one combines all epochs the rms goes down to $\approx 15 \mu\text{Jy}$, while the theoretical limit is $11 \mu\text{Jy}$. To be able to interpret the radio images we have to ask when is a peak in the map significant. Chandra has a point spread function (PSF) of approximately one arc-second. Wrobel et al. (2001) report that astrometric error for phase referenced VLA observations (A-configuration) compared to the International Celestial Reference Frame as established by VLBI (Ma et al. 1998) is less than 10 mas for the X-band. The astrometric uncertainty of the VLA is therefore negligible compared to the Chandra position errors.

We know the positions of the ULXs with the accuracy of Chandra, which is approximately one arc-second. During the first five epochs the VLA was in A configuration and our beam width was ≈ 240 mas. The PSF of Chandra is covered by 24 beams. The probability that we detect a random peak in 24 independent beams is given by the error function. Under the assumption that these 24 beams are indeed independent, the chance that there is a random 3σ peak at the position of a given ULX is 6 %, the chance of a 4σ peak 0.15 %. We can therefore only accept peaks at the positions of the ULXs, if they exceed 4σ . To search for other radio flares in the whole map we have to increase the 4σ limit. We typically map $50''$ by $50''$, which corresponds to roughly 14000 'independent' beams, so there will usually be one 4σ peak in the map. Therefore point sources without known positions are not believable unless they have a higher signal-to-noise than $\approx 5\sigma$.

5.3.2 Non-Detections

There are no significant detections found in M33, NGC 2403, and NGC 5204 in the individual epochs or the full data with a signal to noise higher than 4 within $1''$ of the ULX Chandra X-ray position.

In NGC 2403 we found in the fourth epoch a peak in the map at RA 07 36 25.49 DEC 65 35 39.78 with a flux of $137 \mu\text{Jy}$ which is a 4.4 sigma detection.

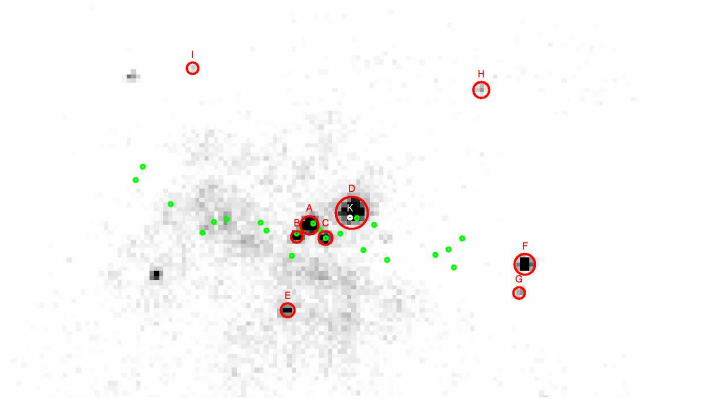


FIGURE 5.1— Map of M82 in the X-rays. The registered X-ray positions are shown in red, radio detections in green and the flare in white.

The VLA position coincides with the ULX position within the accuracy of Chandra. However, the emission seems to originate only from a short time period (5 of 21 minutes). If these times are omitted, the peak in the map vanishes. Some XRBs show such short time radio variability (Ogley et al. 2001). No second short flare was seen in our data. So, it is not possible to confirm such a short flare, especially as the significance is only marginally. We therefore do not consider this emission as a detection of a flare.

5.3.3 M82

In the starbursting galaxy M82 many super nova remnants (SNRs) have been found (see e.g., Kronberg & Wilkinson 1975). It also show diffuse radio emission increasing the achievable rms. The longer baselines are less contaminated by this emission, so we only use baselines exceeding $100 \text{ k}\lambda$. The rms values for a single epoch is still far from the theoretical value: $\approx 0.2 \text{ mJy}$.

The Chandra positions of the bright X-ray point sources have been obtained by registering the positions of the ULXs in different epochs, and the position of the detection with the highest signal to noise have been used. See table 5.4 for the X-ray positions and Fig. 5.1 for a X-ray map. The sources A and D are the well known ULXs (Matsumoto et al. 2001).

The FOV was centered at the ULX D of table 5.4. Thus, the bright X-ray point source F is $18.8''$ away from the phase tracking center. As we are observing in continuum mode, our sensitivity is already reduced for this ULX

due to bandwidth smearing. The distance corresponds to 72 beam widths, thus, the peak flux will be reduced by 5% (Taylor et al. 2004). We have not detected this ULX.

The brightest radio SNR in the FOV (09:55:50.69, +69:40:43.76) is in agreement with the position of a bright X-ray point source (C). The radio and X-ray positions coincide, there does not seem to be a shift in the Chandra and VLA astrometry.

Near the ULX D we have detected a known SNR with a continuum flux of 2 mJy in all epochs. As expected, the flux of the source is stable during the 8 epochs within 1σ of the rms. It has a distance of $0.58''$ to the ULX, well in agreement with the Chandra position.

For the ULX A we find two possible radio counterparts as shown in table 5.4. Both sources are stable and are also visible in the older observations by Kronberg & Sramek (1985). Thus, they are probably also SNR.

Besides the SNR near the reported positions of the ULXs we have not found any flare in M82. However, Kronberg & Sramek (1985) found a 7.07 mJy near the brightest ULX in M82. We have reanalyzed their data for direct comparison with our results. The position of the flare is RA 09:55:50.2 DEC 69:40:45.96, which is $0.98''$ away from the Chandra position of the ULX. It is already visible in the phase-referenced images. In our maps is the flux of the flaring source slightly higher: ≈ 9 mJy, while the brightest SNR at this time (RA 09:55:50.69 DEC 69:40:43.7) has a flux of 105 mJy (108 mJy in Kronberg & Sramek 1985). The flare is stable throughout the 7 hour observation, and is also visible if one divides the observation into 1 hour blocks.

NGC 4736

During all epochs we detect a double source similar to the map shown in Fig. 5.2. Their separation is about $1''$, which corresponds to 20 pc at the galaxy for a distance of 4.3 Mpc. The position of the stronger source coincides with the position of the LLAGN reported by Nagar et al. (2002) and is in agreement with the Chandra position of the first strong X-ray point source in this galaxy (see table 5.1). The other point source has not been detected. As one of the two X-ray sources is probably the nucleus, we assume that the stronger radio source of the two (source A) is the nucleus, while the other radio source is of unknown nature. As this double structure is probably not related with the ULX phenomenon we will discuss the findings in the appendix A.

TABLE 5.4— Radio detections near detected X-ray point sources in M82

Name	X-ray Position Radio Position	Radio F. [mJy]	Dist. arcsec
A	09:55:51.03, +69:40:45.13		
	09:55:50.95, +69:40:45.34	1.9	0.44
	09:55:50.82, +69:40:44.65	1.6	1.15
B	09:55:51.29, +69:40:43.90		
	09:55:51.29, +69:40:44.27	1.3	0.37
	09:55:51.22, +69:40:44.46	1.3	0.66
C	09:55:50.70, +69:40:43.78		
	09:55:50.69, +69:40:43.76	12.3	0.02
	09:55:50.39, +69:40:44.25	1.5	0.56
	09:55:50.82, +69:40:44.65	1.6	0.87
D	09:55:50.15, +69:40:46.48		
Flare	09:55:50.19, +69:40:45.96	9.0	0.52
	09:55:50.05, +69:40:45.91	1.8	0.58
E	09:55:51.48, +69:40:36.03		
F	09:55:46.59, +69:40:40.94		
G	09:55:46.71, +69:40:37.87		
H	09:55:47.48, +69:40:59.64		
I	09:55:53.43, +69:41:01.98		

NGC 5457 (M101)

In the galaxy NGC 5457, which is also known as M101, we detect a 4.2σ peak at the position RA 14 04 14.21 DEC 54 26 02.64 in the second FOV. This flux peak is $1.4''$ away from the Chandra position of the ULX. This distance is larger than the typical position accuracy of Chandra, but it is still possible that it is connected to the ULX. However, besides this peak there is another similar maximum another arcsecond away, and both maxima are found on a lobe of enhanced flux. As the flux peak is just marginally significant and $1.4''$ away from the ULX position, it is unlikely that this flux peak is real emission from the ULX. Besides this, we do not detect significant ($> 4\sigma$) radio emission from the ULXs in the individual epochs or the combined data. In the combined maps of both fields of view we find emission at a 5σ level, which is not at the positions of the ULXs. In the first field we find a source with position RA 14

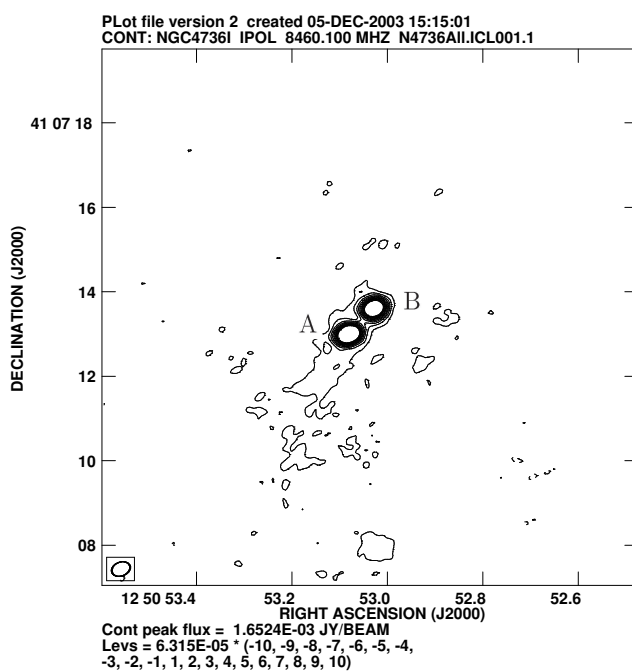


FIGURE 5.2— The double source in NGC 4736. The upper source is called source B and the lower and stronger source is called A.

03 31.31 DEC 54 21 14.93, which has a flux of $92.3 \mu\text{Jy}$ (6.5σ). At the same position is a 4σ peak in the eighth epoch. If one excludes this epoch from the map the source is still visible but has a reduced flux of $72.9 \mu\text{Jy}$. In the second FOV in NGC 5457 there seems to be a double source at RA 14 04 14.32 DEC 54 26 09.42 ($57.318 \mu\text{Jy}$) and RA 14 04 14.25 DEC 54 26 09.38 ($60.512 \mu\text{Jy}$). Both sources are 5σ detections. The nature of these sources is unknown. They could either be SNR in the galaxy itself or background sources.

5.4 Theoretical Interpretations

5.4.1 Flares

The nearest known Galactic cousins of ULXs are the highly accreting black hole XRBs. XRBs in the low hard or the high state are highly variable in the radio and X-ray regime (c.f., van der Klis 1989). The radio flux can vary

by a few hundred percent, for example Cyg X-1 has a typical 15 GHz radio flux of approximately 10 mJy and reaches up to 30 mJy (Pottschmidt et al. 2003). As already mentioned in the introduction stronger accreting objects like GRS 1915+105 or Cyg X-3 show more violent flares of a factor 10 to 100. During these flares GRS 1915+105 reaches 1.5 Jy (Rodriguez et al. 1995) and Cyg X-3 goes up to more than 15 Jy (Watanabe et al. 1994), while the 'steady' state emission is around 100 mJy for both sources. The brighter radio bursts of Cyg X-3 may be due to a higher Doppler factor, as the inclination of this source is only 14° (Mioduszewski et al. 2001). GRS 1915+105 on the other hand is seen nearly edge on (angle to the line of sight: 66°) (Rodriguez et al. 1995).

One possibility to estimate the luminosities of flares one could expect from beamed emission of ULXs is by taking the transients GRS 1915+105 and Cyg X-3 as an example. The average distance of our ULXs is approximately 4.6 Mpc. GRS 1915+105 has a distance of 11 kpc (Fender et al. 1999) while Cyg X-3 is 9 kpc away (Predehl et al. 2000). Without any relativistic beaming these sources would have a flux of $8.5 \mu\text{Jy}$ and $57 \mu\text{Jy}$, which is below our detection limit. However, already a mild beaming factor of 20 for GRS 1915 or an additional factor of 3 for Cyg X-3 would bring the flares into our detection limit (0.15 mJy). As GRS 1915 is seen with an inclination angle of 66° , its Doppler factor will be around one. Thus, a beaming factor of 20 can be reached with a moderate Lorentz factor of $\Gamma = 3$ (Lind & Blandford 1985), if the jet points roughly at the observer (inclination angle $< 15^\circ$). The Doppler factor of Cyg X-3 is uncertain, as the observed luminosity is probably already beamed. But an additional factor of 3 is easy to obtain if the jet is pointing directly to the observer. If the ULXs are flaring in radio we should be able to detect the beamed radio flares.

We have not found a single significant flare for all our sources in the monitoring campaign. In the individual epochs our 4σ sensitivity is on the average 0.15 mJy.

The distance of M33 is around 0.84 Mpc (Freedman et al. 1991). Besides this nearby galaxie all other observed galaxies have distances in the range from 3.6 Mpc to 5.4 Mpc. Thus, the detection limits of flares will only vary by a factor of two for those galaxies. For the average distance of 4.6 Mpc the upper limit on the radio power S_ν of flares is 3.8×10^{17} W/Hz. This corresponds to a 5 GHz radio luminosity (νS_ν) of 1.9×10^{34} erg/sec assuming a flat spectrum. For M33, however, the limit is reduced to a radio power of 1.1×10^{16} W/Hz and a radio luminosity of 5.7×10^{32} erg/sec.

The nondetection may be due to the unknown time scales of the flares in ULXs. We observed our sources once or twice a month. If the time scale of a radio flare is only a day, we are strongly under-sampling the radio light-curve. The time scale of the boosted flares is unclear and depends on the physical process creating the flare. If the flare is created inside the jet, e.g., similar to the shock in jet models used for blazars (see e.g., Marscher & Gear 1985), the observed time scale of the flare will be reduced by the Lorentz factor. For $\Gamma \approx 5$ the time scale could be as short as a few hours. However, it will be extremely bright, even a few mJys are possible. On the other hand, if the flare is created by enhanced injection of material into the jet by the disk for an extended time, the observed time scale will be the same as the intrinsic one.

The fact that we have not found a single flare in all our epochs can be translated to an upper limit for the probability that an average ULXs of our sample has a flare brighter than 3.8×10^{17} W/Hz, which should be detectable. If we assume that the probability that an ULXs is flaring at a given time is similar for all observed ULXs, and one flare is uncorrelated to earlier or later flares, the flares should be Poisson distributed. The probability distribution describing how many events we detect given the probability of a detection is

$$P(\lambda, n) = \frac{\exp^{-\lambda} \lambda^n}{n!},$$

where λ denotes the expectation value of the distribution and n is the number of events.

For this study we have to exclude M82 as the rms in the M82 maps is much higher than in the other fields. The other six fields have been observed for eight times which yields 48 samples. Let ρ denote the upper bound of the duty cycle of the ULX. Thus, it is an upper limit for the probability that one ULX flares at a given moment. ρ has to be chosen, such that we should have almost certainly detected at least one event if the probability that a given ULX flares is ρ . Here ρ will be chosen such that we should detect one or more flares with a probability of 95%. This leads to

$$0.95 = \sum_{n=1}^{n=\infty} P(48\rho, n) = 1 - \exp^{-48\rho}.$$

This results in $\rho = 0.06$, i.e. the duty cycle of radio flares exceeding our detection threshold in ULXs is $< 6\%$. The expectation value for the number of flares is 2.9, our detection of no flares is in agreement with this value at a 5 %

level.

If we know the time scale of a typical flare in an ULX we can convert the upper limit of the flaring probability to an upper limit of the number of flares a ULX can have in a year. Let δt_{Flare} denote an average length of a flare. As the radio flares of GRS 1915 have a time scale of days, we will use $\delta t_{\text{Flare}} \approx 2$ days as a reference. Thus, the upper limit of the probability to detect a flare in a single observation corresponds to an upper limit of $11 \frac{\delta t_{\text{Flare}}}{2 \text{days}}$ radio flares per year. This upper limit is still higher than the number of bright flares in GRS 1915+105.

Besides looking for radio emission from ULXs we can use these observations to derive upper limits on the amount of radio transients happening in a galaxy. Our galaxies have an average distance around 4.6 Mpc and we mapped an area of $51''$, this results in an observed area of 1.3 kpc^2 . We are searching for radio flares from unknown sources, therefore, it is also not known which is the quantity correlating with the number of flares. While for ULXs the star formation rate might be a good quantity it could simply be the number of stars or black holes for an other class of flaring objects. As we are observing a couple of small fields in different galaxies, it is very hard to derive the exact number of observed solar masses or even the observed star formation rate. As most of our observed galaxies (besides M82, which we exclude) are non starbursting galaxies, the star formation rate per solar mass will be of the same order of magnitude. In order to get a rough estimate how much mass we have actually observed, we assume a similar mass density as in our Galactic neighborhood. In our Galactic neighborhood the mass density of the disk is of the order of $200 M_{\odot}$ per pc^2 . Therefore one field of view observes a mass of approximately $3 \times 10^8 M_{\odot}$. Thus, we expect less than 0.2 flares in a single observation of $10^9 M_{\odot}$.

5.4.2 Background Sources

We have detected continuous radio sources only inside NGC 5457 (excluding M82). In all other fields there were no background sources visible. However, we only map an area of $51'' \times 51''$. According to the FIRST radio survey (Becker et al. 2003) there is approximately one radio source per 40 square-arc-minutes. Our observations have a better resolution ($0.2''$ compared to $5''$) and a four times better rms ($37 \mu\text{Jy}$ to 150 mJy). Our detection count in this survey is therefore two detection (NGC 5457) in 4.5 square-arc-minutes. Slightly higher source counts have to be expected especially as the sources could be within the observed galaxie. So the non-detections of background sources in most fields

are in agreement with the density of background sources.

5.4.3 Steady State Emission

In M82 two of the three reported Chandra ULXs positions are in agreement with the positions of radio SNR. For all other galaxies we have not detected any continuous emission near the ULXs. The upper flux limit for the observed sources is $\approx 60\mu\text{Jy}$ (4σ). For the steady state emission ULXs should lie on the radio/X-ray correlation (Falcke et al. 2004; Merloni et al. 2003) for XRBs and AGN. Simple jet scaling (Falcke et al. 2004) predicts that the X-ray and radio emission are correlated and scale according to:

$$L_X \propto L_R^{1.38} M^{0.81} \quad (5.1)$$

where L_X and L_R denote the X-ray and radio luminosities. The exact value of the exponents depends on the spectral indices of the radio and X-ray emission. In Fig. 5.3 we plot the 3–9 keV X-ray luminosity against the 5 GHz radio luminosity. The radio luminosity is always calculated assuming a flat spectrum, i.e., it is defined as $L_{5\text{ GHz}} = 5\text{ GHz} S_{5\text{ GHz}}$ where $S_{5\text{ GHz}}$ denotes the radio power at 5 GHz. The Chandra X-ray luminosities are corrected for the different energy band assuming a photon index of 1.6. Besides a sample of low hard state XRB (GX339-4, V404 Cyg, XTE J1118+480, 4U 1543-47, GS 1354-64) we show the two XRBs used to extrapolate to the expected radio flare luminosities: GRS1915 and Cyg X-3. The datapoints have been taken from Gallo et al. (2003). The brightest 1.5 Jy flares of GRS1915 are not included in the plot. Additionally we present a sample of AGN consisting of low luminosity AGN, FR-I radio galaxies (Fanaroff & Riley 1974), and radio and X-ray selected BL Lac objects. This figure is similar to Fig. 3 in Falcke et al. (2004). Furthermore, we show the theoretical radio/X-ray scaling for Black holes of different black hole masses.

A strict radio/X-ray correlation will only be valid for the steady state emission of low/hard state, jet-dominated sources. For high state objects the radio emission will be quenched (see, e.g., Maccarone et al. 2003). Thus, we can not expect that the correlation holds for the flares of the transient sources. Those flaring sources are only included for comparison.

The empirical correlation can be used to compare the upper limits (4σ) of this radio monitoring campaign with the expectations. The radio flux of high or very high state objects may be reduced compared to the low/hard state objects. The correlation gives an upper bound for the expected radio flux. Only

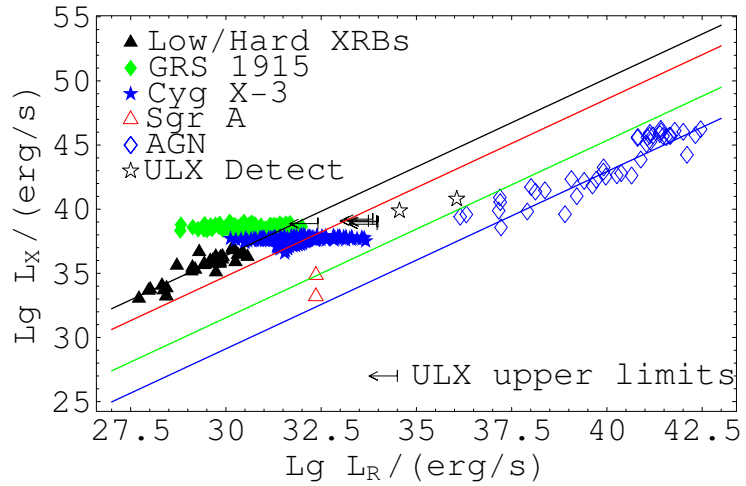


FIGURE 5.3— The upper limits of the ULXs in respect to the XRB and AGN population. The lines correspond to different black hole masses. From Top to bottom $6, 6 \times 10^2, 6 \times 10^6, 6 \times 10^9 M_{\odot}$. The left ULX radio detection represents NGC 5408, while the right is the flare in M82. The correlation should not hold for fares, it is just plotted for comparison. Thus, as GRS 1915 and Cyg X-3 are both radio transients, they are not expected to follow the correlation.

the upper limit for M33 is close to the value expected from the correlation for stellar mass black holes. All other upper limit are far above the expected radio flux from microblazars with stellar mass black holes. The non-detections are in agreement with beamed or unbeamed radio emission from stellar or intermediate mass black holes $\lesssim 10^3 M_{\odot}$.

5.4.4 Other Radio Detections of ULXs

Up to now there are two radio detections mentioned in the literature, here we discuss their interpretation within the microblazar model. Kaaret et al. (2003) have detected radio emission from an ULX with an X-ray luminosity 1.1×10^{40} erg/sec in NGC 5408. They find a 4.8-GHz radio flux of 0.26 ± 0.04 mJy and give an upper limit for the X-band flux of 0.12 mJy (3σ). The spectral index is therefore larger than $\alpha > 1.0$. We would expect that the radio cores of microblazars have a flat to inverted spectrum, by far flatter than the observed steep spectrum. As we have the radio and X-ray luminosity we can use the radio/X-ray correlation to compare the ULX in NGC 5408 with XRBs and AGN. The source seems to be too radio loud for a stellar mass black hole,

as shown in Fig. 5.3. Under the assumption that the source should lie on the correlation, we can derive a mass for the object of $\approx 500M_{\odot}$. Otherwise, the observed emission could be explained by a flare, or by extended emission like a radio supernova.

Kronberg & Sramek (1985) found a 7.07 mJy flare in M82, which we also confirmed by reanalyzing their data. The flare position is within the errors of the brightest ULX in M82 which has up to 9×10^{40} erg/sec. This flare is bright compared with GRS 1915, which we expect to show boosted 0.4 mJy flares. However, the value does not seem to be unrealistic for a major flare and the uncertainty of the flux estimate. Up to now no second event has been reported, even though M82 has been frequently observed. Thus, these events seem to be extremely rare. For comparison we have also shown the flare in Fig. 5.3. However, the radio/X-ray correlation is only valid for steady state emission.

5.5 Conclusions

We have monitored nine ULXs during five months with the VLA. Our limiting sensitivity of the individual epochs is around 0.15 mJy (rms $\approx 36\mu\text{Jy}$), with the exception of M82. We have not found any significant flare in the sample. Unfortunately the expected time scales of the radio flares are very uncertain. If they last only a few days, we are heavily under-sampling the light-curve. However, we can give an upper bound of 6% for the probability to find a flare in a given observation of an ULXs. This translates to an upper bound of $11 \frac{\delta t_{\text{flare}}}{2\text{days}}$ flares per year with a time scale δt_{flare} . This is much more than observed for example in GRS 1915. Thus this monitoring campaign can not rule out or strengthen the idea of relativistically beamed flares in ULXs.

The search for flares has lead to the detection of a flux peak within the uncertainties of the position of the ULX in NGC 2403 at a significance of 4.4σ . As this peak originates from only a 5 minutes interval and is not seen in the rest of the scan, we do not consider this as a detected flare. We have reconfirmed the 7 mJy flare near the brightest ULX in M82 in archival data from Kronberg & Sramek (1985).

We have detected a yet unreported variable double source in NGC 4736. As the positions of the stronger source coincides with the position of the nucleus of the LLAGN as reported in Nagar et al. (2002), we assume that this double source is probably connected to the LLAGN and not to the phenomenon of ULXs.

The search for continuous emission from ULXs was only successful for M82. Here two SNR could be associated with ULXs. However, it has be shown

that the current upper limits are in agreement with the radio/X-ray correlation even if the sources are radio loud. The search for a radio loud ULXs is therefore still open and detections will be extremely hard for current telescopes. Therefore, the investigations of these intriguing sources have to continue.

5.6 Appendix: The LLAGN in NGC 4736

As we have already mentioned in Sect. 5.3.3, we have detected a double source in NGC 4736 show in Fig. 5.2. One of these sources is stronger (2.2-1.2 mJy, source A) and variable while the other source seems slightly extended and is fairly stable in flux (1 mJy, source B). The positions are RA 12 50 53.08 DEC 41 07 13.00 and RA 12 50 53.03 DEC 41 07 13.61 respectively. The peak fluxes and the ratio of the two sources is shown in Table 5.5, for a light-curve of the peak fluxes see Fig. 5.4. Due to the low fluxes of both sources it is not possible to self-calibrate the data itself. The fluxes can therefore be reduced by phase errors. They can furthermore be changed by amplitude calibration. However, the flux-ratio of the two sources should be independent of these effects. In the radio the variability can also be seen, it varies between 2 and 1.2 on a time scale of months as also shown in the table. We therefore conclude, that at least the stronger source A is variable. This indicates that source A is a compact object, probably the nucleus of the low-luminosity AGN. It has the position that was previously published by Nagar et al. (2002). Source B is not mentioned in earlier publications, but Nagar et al. (2002) rms value was significantly higher (0.34 mJy). We have reanalyzed their data, and detect a 4σ peak at the position of source B (1.4 mJy). Source B was therefore already visible in March 1998.

For the discussion of the other source we have to consider that the array configuration of the VLA changed between the epochs five and eight from A-configuration to B-configuration, increasing the beam size from 260 mas to 840 mas. Extended emission will therefore contribute more to later epochs than to the first. This explains the increasing peak fluxes of the source 2 from 1 mJy to 1.7 mJy in the last epochs. The effect that the peak flux increases with the beam-size can be seen if one uses a uv-taper of $400 k\lambda$, which roughly doubles the beam-diameter. The peak flux increases from 1.1 to 1.3 mJy in epoch one. The extension of source B is also visible in the difference between the peak and the integrated flux. For source A these two values are usually similar, while for source B the integrated value is higher by approximately 30 %. It is puzzling that the integrated fluxes are more variable (1.1 – 1.8 mJy) than the peak fluxes. We checked that this effect is not due to phase errors, epoch one

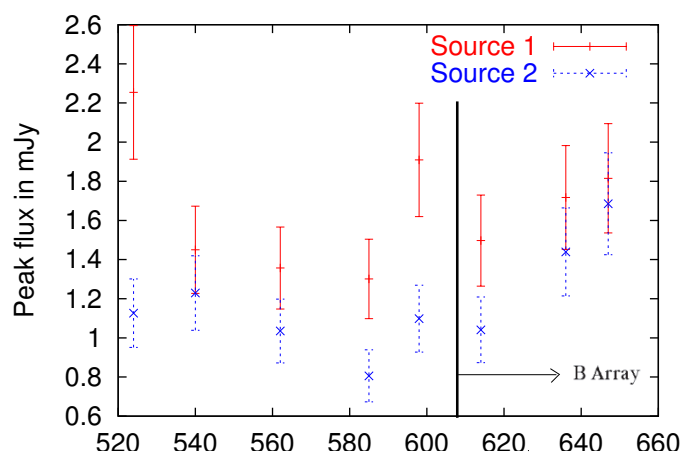


FIGURE 5.4— Light-curve of NGC 4736. Note that the VLA array configuration changed from A to B during the last epochs.

and two have phase jumps between successive calibrator scans of less than 40° , usually less than 10° . This would result in only a few ($< 6\%$) amplitude loss. One problem of the integrated flux is that the integration boxes are small, as both point sources are less than an arc-second away. Another possibility could be that source B is barely resolved, small changes in the beam size and the atmosphere could then lead to the observed variability. An extended (> 200 mas) source which is variable on time scales of months at a distance of 4 Mpc is not possible, as its size would be larger than 5 pc. However, there could be a compact substructure in the second source which is varying.

During the last epoch we also obtained a C-band map of NGC 4736. As the VLA was already in B-configuration the two sources could not be separated. Both sources combined give a peak flux of 4.1 mJy and an integrated flux of 7.3 mJy.

To check the spectrum of the two sources we have also obtained U-band images during the last epoch. Source A has a peak and integrated flux flux of 1.7 mJy. The weaker source two has a peak flux of 1.1 mJy and 0.95 mJy integrated flux. The missing integrated flux is probably due to the small integration box around the peak needed to avoid source A. The diameter of the beam was 480 mas. We have reanalyzed the old data from Mar 1998 to check for the

second source. Both peaks are visible in the map with fluxes of 2.235 mJy and 1.403 mJy respectively. However, the rms was 0.34 mJy making accurate flux measurements impossible.

We can not compare the U-band flux directly to the X-band flux, as the beam size of the X-band observations is about twice the U-band beam size. As the flux of the second source is roughly constant during the first epochs, we compare the U-band flux with the last epoch in A-configuration and taper the data to get a beam-size of 480 mas. The flux of the second source increases to 1.41 mJy. This results in a spectral index between 15 and 8.4 GHz of $\alpha = 0.42$.

No other low-luminosity AGN (LLAGN) in 2 cm survey of Nagar et al. (2002) shows such a double structure. The nature of the second source is unknown. It could either be a hotspot or a jet feature of the LLAGN. However the spectral index is fairly flat, thus the hotspot has to be self-absorbed. If this source would be observed at a greater distance and the two components unresolved, the spectrum would peak at a few GHz, as source A has a flat spectrum. This source could therefore be a close-up of a GHz peak source (GPS). An other explanation is that inside the extended emission there is a compact flat spectrum source. If confirmed, this would be spectacular as this could either be a second nucleus or the radio core of an ultra-luminous X-ray source. Thus, this double source could be the nucleus of the galaxy together with a microblazar, a double nucleus or the nearest GPS source.

TABLE 5.5— Radio flux and beam size of the double source in NGC 4736

Julian Date	Peak 1 [mJy]	Integ. 1 [mJy]	Peak 2 [mJy]	Integ. 2 [mJy]	Ratio Peak	Beam size [mas]
59524	2.25	2.1	1.13	1.4	2.0	251
59540	1.45	1.7	1.23	1.8	1.2	279
59562	1.36	1.4	1.04	1.3	1.3	261
59585	1.30	1.3	0.81	1.1	1.6	268
59598	1.91	2.0	1.10	1.7	1.7	260
59614	1.50	1.6	1.04	1.3	1.4	414
59636	1.72		1.44		1.2	504
59647	1.82		1.69		1.1	827

6

Short Time Variability of XRBs

6.1 Introduction

Up to now we have tested the jet model by looking at the spectra (chapter 3) and the phenomenon of relativistic beaming (chapter 4). However, to constrain the models and physical parameters of accreting black holes it is important to access all observable quantities. Besides the spectra the variability is of high importance as it can reveal information about the central engine and its dynamics. In this chapter we will check, whether the variability is in agreement with our jet model. The arguments in this chapter have also been published in K rding & Falcke (2004).

Strong variability is a common phenomenon for XRBs (see e.g., van der Klis 1989). The jet/synchrotron model (see chapter 2) predicts a rigid power law that can only vary in amplitude and in spectral index. Variability in Comptonization models can lead to a power law X-ray spectrum as well (see e.g., Kylafis & Klimis 1987). Here we will investigate whether the short term variability of active black holes can be explained with a rigid pivoting power law model. We will concentrate on BHXRBs as detailed light-curves are available, but applications to AGN are as well possible.

Usually BHXRBs appear in two distinct states: the hard state (low flux levels accompanied with a hard power law spectrum) and the soft-state (normally higher flux and a soft X-ray spectrum, see e.g., van der Klis 1994). In the hard-state a relativistic jet can usually be seen in radio observations (e.g., Fender 2001). We will focus our studies on the hard state, where the X-ray spectrum is dominated by a power law.

A BHXRB in the hard state shows significant short time (0.1–100 Hz) variability with a root mean square (rms) around 20% (see e.g., van der Klis 1995). It is therefore possible to make a detailed statistical analysis of the observed light curves. The light curves at different photon energies are well correlated as the cross-correlation function peaks nearly at unity. Furthermore, the coherence function (Vaughan & Nowak 1997) is nearly unity for a wide range of Fourier frequencies. However, one often observes hard lags, e.g. the hard photons lag behind the soft photons up to a few milliseconds (e.g., see Nolan et al. 1981, Miyamoto & Kitamoto 1989, Miyamoto et al. 1991, or Pottschmidt et al. 2000, for a definition of phase lags see below, Eq. 6.13). The existence of hard lags has been explained using Comptonization models. Soft photons will be repeatedly up-scattered in a large corona, as the harder photons need more inverse Compton processes to reach their energy this results in hard lags. For studies using coronae see e.g., Miyamoto et al. (1991), Nowak et al. (1999), Malzac & Jourdain (2000), Poutanen (2002), or Böttcher et al. (2003). As already noted by these authors, this explanation has the problem that one needs huge coronae and the Fourier frequency dependence of the X-ray time lags cannot be reproduced.

Additionally the observed auto-correlation is not reproduced well (see e.g., Maccarone et al. 2000). A different approach has been made by Kotov et al. (2001), where the authors explain the phase lags with the response of the accretion disk to perturbations and present a short discussion of the effects of a pivoting power law.

By the term pivoting power law we mean that the X-ray spectrum at different times can always be described by a power law, which only varies in the power law index and the overall intensity. We mostly consider the case where the amplitude and the power law index are correlated.

The idea of a pivoting power law model arises from recent theoretical and observational results. The spectrum of BHXRBs can be well described using a coupled jet/accretion disk model (see Markoff et al. 2001a). Here the disk (possibly a optically thin accretion disk, e.g., such as ADAFs and related solutions, Narayan & Yi 1995, plus a standard disk) is only visible as an additional component in the UV, while the flat spectrum at radio and optical wavelength and the power law in the X-rays is created by synchrotron and inverse Compton emission from the jet. In particular, the hard X-ray power law is explained as optically thin synchrotron emission from a single region at a few hundred Schwarzschild radii from the black hole. The power law index depends on plasma parameters (e.g., electron temperature, adiabatic index), and

may therefore respond to changes of the jet power and the accretion rate. As the total intensity depends on these parameters as well, the flux and the power law index should be correlated. The jet/synchrotron model therefore suggests that the X-ray emission behaves like a pivoting power law.

Within the jet/disk picture of chapter 1 - 3, TeV Blazars like Mrk 421 or Fanaroff-Riley class I radio galaxies (Fanaroff & Riley 1974, the unbeamed parent population of BL Lacs within the unified scheme, Urry & Padovani 1995b) show many features of BHXRBS in the low/hard state, namely a domination of the spectral energy distribution by jet emission. Mrk 421, for example, shows hard lags and a positive hardness/flux correlation (Zhang 2002). The hardness seems to show a hysteresis effect, e.g. the power law index seems to respond slightly after the variation of the total intensity. If BHXRBS also have a power law from their jets, a similar pivoting power law could play an important role. Hard lags and positive or negative hardness-flux correlations have also been found in Seyferts and other AGN (see e.g., Chiang et al. 2000 or Lamer et al. 2003).

A pivoting power law may also be applicable for Comptonization models. Analyzing long term variability (timescales of days) of BHXRBS Zdziarski et al. (2003) suggest the existence of a pivoting power law with a pivot point around 50 keV and explains the behavior using Comptonization in a corona. They find a negative correlation between flux and hardness. These long term variations arise probably from a different source of variability (e.g., the accretion rate or an other unknown parameter, see Homan et al. 2001) than the short term variations studied here (maybe created by magnetohydrodynamic instabilities, see Psaltis & Norman 2002, or other unknown sources). Thus, it is yet unclear if such a correlation holds for fast variations and the true hard state.

In this chapter we will analyze in a general way the effects of a pivoting power law model, where the power law index is correlated with the flux. We calculate the effect on the phase lags and the auto- and cross-correlation functions, and present a Monte Carlo simulation of the coherence function. In addition to the work by Kotov et al. (2001), who also discussed the possibility that the power law index is directly correlated with the flux, we include a response time for the change of the power law index as a function of intensity.

In Sect. 2 we describe our parameterization and model. With these definitions we derive a general analytic solution for phase lags and cross-correlation functions for a pivoting power law in Sect. 3. In Sect. 4 the analytic result is compared with a Monte Carlo simulation. In the last two sections we discuss our model in the context of data from Cygnus X-1 and present our conclusions.

6.2 Parameterization of the Pivoting Power Law Model

As we try to calculate the time lags with an analytical approximation it is important to parameterize our pivoting power law model around a reference photon energy ϵ_0 near the observed energies. Let the flux S of our source be a function of photon energy ϵ and time t

$$S(\epsilon, t) = A(t) \left(\frac{\epsilon}{\epsilon_0} \right)^{-\alpha + \beta(t)}, \quad (6.1)$$

where α represents the constant part of the spectral index while $\beta(t)$ accounts for the variations. The function $A(t)$ describes the flux at the reference energy ϵ_0 . As we will consider the case that $A(t)$ and $\beta(t)$ are correlated, the reference energy ϵ_0 will not be the pivot point defined by the minimum of the rms.

If the changes in spectral index are small and we are observing photon energies near the reference energy ($\ln \left(\frac{\epsilon}{\epsilon_0} \right) \beta(t) \ll 1$) we can expand the equation

$$S(\epsilon, t) = A(t) \left(\frac{\epsilon}{\epsilon_0} \right)^{-\alpha} \left(1 + \beta(t) \ln \left(\frac{\epsilon}{\epsilon_0} \right) \right), \quad (6.2)$$

and find in Fourier space, denoted by \hat{S} :

$$\hat{S}(\epsilon, \omega) = \left(\frac{\epsilon}{\epsilon_0} \right)^{-\alpha} \left(\hat{A}(\omega) + \widehat{\beta A}(\omega) \ln \left(\frac{\epsilon}{\epsilon_0} \right) \right). \quad (6.3)$$

As we are interested in phase lags, depending on the coherence features of $A(t)$, it is inappropriate to use red noise for the light curve. Information on the coherence of the light curve can be guessed from the power spectral density (PSD) defined as $\text{PSD}(\omega) = \hat{A}^*(\omega) \hat{A}(\omega)$, where the star denotes complex conjugation. We note that the PSD of many BHXRBs can be well described by a sum of a few broad Lorentzians

$$\text{PSD}(\omega) = \sum P_{\omega_i, R_i, Q_i}(\omega), \quad (6.4)$$

with

$$P_{\omega_i, R_i, Q_i}(\omega) = \frac{4R_i^2 Q_i \omega_i}{\omega_i^2 + 4Q_i^2 (\omega - \omega_i)^2}, \quad (6.5)$$

where one Lorentzian can be centered around $\omega = 0$ (see Nowak 2000, Pottschmidt et al. 2003, or Belloni et al. 2002). This definition of a Lorentzian follows Belloni et al. (2002). The quality factor Q is a measure of the full width

half maximum (FWHM) $Q = \frac{\omega}{2\pi\text{FWHM}}$. The normalization factor R describes the amplitude of the Lorentzian. It is connected to the total rms amplitude as

$$\text{rms}_i = R_i \sqrt{\frac{1}{2} - \frac{\tan^{-1}(-2Q_i)}{\pi}} \quad (6.6)$$

(see e.g., Pottschmidt et al. 2003). Lorentzians usually arise from damped oscillating systems, for example they are used to describe the spectral shape of a laser. The quality factor Q describes how strong the oscillator is damped, a high Q denotes a nearly undamped system with a strongly peaked PSD, while a low value for Q yields a highly damped system with an asymmetric, weakly peaked PSD. Usually around four Lorentzians with a quality factors $Q \lesssim 1$ are needed to fit the PSD of XRBs in the low/hard state. As the origin of these broad Lorentzians is still unknown we assume that each Lorentzian is created by a strongly damped oscillator excited at random times. For example, these oscillators could be due to excitations at different locations on the accretion disk with a Fourier frequency defined by the Keplerian rotation that may or may not be transferred into the jet. Other possible explanations include magnetohydrodynamic instabilities (Psaltis & Norman 2002) or jet precession.

To simplify the discussion we first look at only one broad Lorentzian centered around ω_0 . We assume that the variability is created by a damped oscillator. To generate our light-curve we use a simple shot noise model (for shot noise models see e.g., Terrell 1972, Lochner et al. 1991 or Negoro et al. 2001). Let us first assume that the light curve of the BHXRb can be described as $F(t)$, if this oscillator has only been excited at $t = 0$ with a unit excitation. The overall light curve will be a superposition of many excitations at random times and amplitudes. If λ_i describes the amplitude of the excitation at the time t_i we can write

$$A(t) = A_{\text{DC}} + \sum_i \lambda_i F(t - t_i), \quad (6.7)$$

where A_{DC} describes the constant offset of the flux. The amplitudes λ_i and the excitation times t_i are random variables. We choose the normalization of $F(t)$ such that $\langle \lambda^2 \rangle = 1$. Using this process we create a light curve that has the observed PSD and the coherence properties given by the oscillator.

It is unclear whether such simple shot noise models can describe the light-curves of XRBs (see e.g., Lochner et al. 1991). However, we have to disentangle the contributions of the different broad Lorentzians to apply our model, so it is very hard to test a pivoting power law model using observed light curves.

Shot noise is therefore one of the best possibilities to create artificial light curves available. Furthermore, this approach enables us to give an analytic solution for the phase lags and the cross-correlation function. We discuss below the effect of different coherence properties. The main result is likely to be independent of the shot noise assumption.

Transferred into Fourier-space we find

$$A(\omega) = A_{\text{DC}}\delta(\omega) + \sum_i \lambda_i \hat{F}(\omega) e^{i\omega t_i}. \quad (6.8)$$

The PSD of a complex damped oscillator is a Lorentzian, but as we are interested in real solutions for the light curve we have to use a linear combination of the real and the imaginary part of the damped complex oscillator. The two fundamental real solutions are the instantaneously excited oscillator (cosine)

$$\hat{F}_c(\omega) = \frac{1}{2} (\hat{H}_+ + \hat{H}_-) \quad (6.9)$$

and

$$\hat{F}_s(\omega) = \frac{1}{2i} (\hat{H}_+ - \hat{H}_-) \quad (6.10)$$

the sine combination, where $\hat{H}_\pm = \frac{2R\sqrt{Q\omega_0}}{\omega_0 - 2iQ(\omega \pm \omega_0)}$ is the Fourier transform of the complex oscillator with frequency $\omega = \pm\omega_0$. We note that the spectral form of the cosine combination F_c declines with ω^{-2} like the Lorentzian, while the sine term drops with ω^{-4} .

Given the light curve $A(t)$ we have to choose a physical response of the power law index $\beta(t)$. Whatever model one uses for the X-ray emission (Comptonization or jet model) the spectral index depends on physical properties near the accreting object. It is therefore likely that $\beta(t)$ will respond to changes of the accretion rate. As the region of emission has a characteristic size, β may not follow $A(t)$ directly, but may respond a bit later. It is also possible that the emission mechanism has a response time itself (e.g., for the jet model how fast is the particle acceleration mechanism responding). We will take this into account by introducing a response time τ . The first order approximation of β will therefore depend linearly on $A(t - \tau)$. We assume that τ will be a small fraction (a) of the period of the center frequency of the Lorentzian, i.e. $\tau = a2\pi/\omega_0$ with $0 \leq a < 1$.

The first order approximation form of β and the simplest form with the

described properties is

$$\beta(t) = \gamma A_{\text{AC}}(t - \tau), \quad (6.11)$$

where the subscript AC marks the contributions to the light curve from the damped oscillators. The constant part of a variable will be marked with a subscript DC throughout this chapter. In the case of a positive hardness/flux correlation, as seen in Mrk 421 and other Blazars, the parameter γ is positive. For a negative correlation, seen in long timescale variability of some BHXRBs, one has to use $\gamma < 0$. For illustrative purposes we first use a positive hardness/flux correlation ($\gamma > 0$) in our calculations and discuss the other case in a separate subsection.

In Fourier representation one finds for β

$$\hat{\beta}(\omega) = \gamma e^{i\omega\tau} \hat{A}_{\text{AC}}(\omega) \hat{D}(\omega), \quad (6.12)$$

where we included an additional damping factor $D(\omega)$. It should take into account the damping of the system creating the power law, i.e. if ω is too big, the oscillations are so fast that they average out, and the power law index $-\alpha + \beta(t)$ does not change anymore.

6.3 Analytic Results

6.3.1 Definition and Energy Dependence of Phase Lags

The phase lag measures the phase change (corresponding to a time delay) between the light curves at two photon energies in phase space. The Fourier phase lag $\phi(\omega)$ is defined as the argument of the average cross power spectrum

$$\phi(\omega) = \arg \langle \hat{S}^*(\epsilon_1, \omega) \hat{S}(\epsilon_2, \omega) \rangle \quad (6.13)$$

see e.g., Nowak et al. (1999). The Fourier phase lag can be translated to time lags by dividing through ω . The time lags have a simple interpretation in the time domain, as they measure the time difference between an outburst at two different photon energies at a given Fourier frequency. To calculate the phase lag from a light-curve we start from

$$\sin \phi = \frac{\Im \left[\hat{S}^*(\epsilon_1, \omega) \hat{S}(\epsilon_2, \omega) \right]}{|\hat{S}(\epsilon_1, \omega)| |\hat{S}(\epsilon_2, \omega)|}. \quad (6.14)$$

Using the linear approximation (Eq. 6.8) the phase lag can be evaluated

analytically (see also Kotov et al. 2001):

$$\begin{aligned} \sin \phi &\approx \frac{\Im \left[[\hat{A}^* + (\widehat{\beta A})^* \ln \left(\frac{\epsilon_1}{\epsilon_0} \right)] [\hat{A} + (\widehat{\beta A}) \ln \left(\frac{\epsilon_2}{\epsilon_0} \right)] \right]}{\hat{A}^* \hat{A}} \\ &\approx \frac{\Im \left[\hat{A}^* (\widehat{\beta A}) \right]}{\hat{A}^* \hat{A}} \ln \frac{\epsilon_2}{\epsilon_1}. \end{aligned} \quad (6.15)$$

So, if $\hat{A}^* (\widehat{\beta A})$ has a nonzero imaginary part, the phase lag will vary with $\ln \epsilon$ as seen in the observations of BXRBs. The photon energy dependence of the phase lag is therefore independent of the response $\beta(t)$ of the power law index, but the overall magnitude and the phase lag dependence on Fourier frequency ω depends on the choice of β .

6.3.2 Fourier Frequency Dependence of the Phase Lag

To derive the phase lag we start with Eq. (6.15). In our linear approximation the only unknown component is the Fourier transform of βA . Using the convolution theorem and the Fourier transform of β from Eq. (6.12) we get:

$$\begin{aligned} \widehat{\beta A} &= \gamma \int e^{i\omega' \tau} \hat{A}_{AC}(\omega') \hat{A}(\omega - \omega') \hat{D}(\omega') d\omega' \\ &= \gamma \int e^{i\omega' \tau} \hat{A}_{AC}(\omega') \hat{A}_{AC}(\omega - \omega') \hat{D}(\omega') d\omega' \\ &\quad + \gamma A_{DC} \hat{A}_{AC}(\omega) \hat{D}(\omega) e^{i\omega \tau}. \end{aligned} \quad (6.16)$$

For the case $\hat{D}(\omega) = 1$ it is possible to give an analytic calculation of the phase lag. The calculation is described in Appendix 6.7 and we just give the result for an instantaneously excited oscillator:

$$\sin \phi = \gamma \ln \frac{\epsilon_2}{\epsilon_1} \left(A_{DC} \sin(\tau \omega) + \frac{\langle \lambda^3 \rangle}{\langle \lambda^2 \rangle} \Im \left(e^{i\tau \omega} f_1(\omega) \right) \right), \quad (6.17)$$

where $f_1(\omega)$ is given in the appendix. The λ denote the random excitation power of the oscillators. It is important to note that the calculations show that one can treat each excitation of the oscillator separately – the contributions of different excitations average out.

The first term in Eq. (6.17) is the result of the pivoting power law acting on the constant flux, while the second term represents the pivoting power law acting on the pulse itself. So the second term depends on $\frac{\langle \lambda^3 \rangle}{\langle \lambda^2 \rangle}$ and will therefore

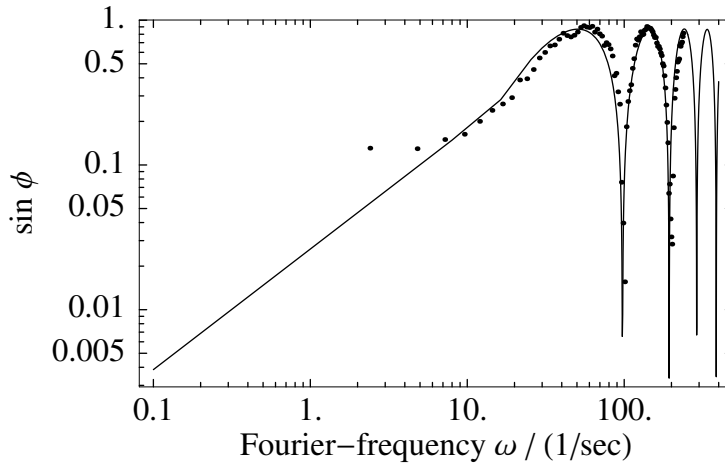


FIGURE 6.1— Phase lag dependence on the Fourier frequency. The solid line represents the analytic approximation, the dots are the results of a Monte Carlo simulation. The deviation of the Monte Carlo simulation at lower frequencies is a numerical effect.

vanish if the λ are distributed symmetrically around zero. In that case only the first term will contribute in that order of the perturbation series, but higher orders can be nonzero.

The behavior of the phase lag is illustrated in Fig. 6.1 (solid line). For small $\omega\tau$ the phase lags increase linearly with frequency. This means that the time lags are constant for small frequencies. Once $\omega\tau \approx \frac{\pi}{2}$, the phase lags start to oscillate. If τ is of the order of $\frac{2\pi}{\omega_0}$ this will happen roughly at $\omega > \omega_0$.

The result that the phase lag starts to oscillate is at least partly due to our deterministic law of a fixed look-back time τ . A more realistic approach would be that τ is itself a random variable, e.g., Gaussian distributed around a mean value. As the sine is linear for $\omega\tau \ll 1$ the phase lags for low Fourier frequencies will not change. However, for $\omega\tau \gtrsim 1$ the contributions to the phase lags for different τ will average out. The oscillation will be further reduced as the PSD of a real system is described by several Lorentzians, i.e. for $\omega \gg \omega_0$ a second Lorentzian will dominate the first one. It is therefore likely that one will never observe the oscillating part of the phase lag.

To take the probably statistical nature of τ and additional damping of the response of the power law into account, we choose a damping term $\hat{D}(\omega) \neq 1$, for example $\hat{D}(\omega) = e^{-\delta\left(\frac{\omega}{\omega_0}\right)^2}$, which will cut off the phase lags at a given fre-

quency. With an appropriately chosen damping the phase lag will not oscillate but stay at zero for higher Fourier frequencies.

Hence, we conclude that the phase lag in the case $\tau > 0$ can be approximated by

$$\sin \phi \sim \gamma \sin(\omega\tau) \hat{D}(\omega) \ln \frac{\epsilon_2}{\epsilon_1} \quad (6.18)$$

and is independent of the exact shape of the pulses. We find hard lags for a positive hardness flux correlation and a positive look-back time. If one changes the parameters, e.g., negative hardness flux correlation and positive look-back times, soft lags can be obtained.

We can now verify that our simplification made in Eq. (6.7) was appropriate. We assumed that all excitations are identical and only vary in amplitude and excitation time. In a real system each excitation will have a different shape. But as the contributions to the phase lags from different excitations average out, each pulse contributes as if there are no other excitations (the sum in Eq. 6.29 only runs over the diagonal part). The overall phase lag will be the average of all pulses or the phase lag of an average shaped pulse. In the zeroth order approximation the coherence does not play a role for the phase lags (as long as there is a constant flux component). Thus the shot noise assumption is not a crucial ingredient for the model. The important assumption is only that the PSD can be decomposed into different Lorentzians, which do not interact with each other.

In the case that the power law index responds instantly to a change in the accretion rate, the first term of Eq. (6.17) will vanish and the phase lag depends to first order in γ linearly on $\langle \lambda^3 \rangle$. The lags would therefore vanish in the case of a symmetric distribution of the λ (many systems show asymmetric excitations, for one example see Spruit & Kanbach 2002). Furthermore, they depend strongly on the linear combination used for the pulse shape. The lags created by the sine and cosine term are shown in Fig. 6.2. Nevertheless, if the power law index Γ is varying by $\Delta\Gamma \approx 0.2$, as will be used here later on, the phase lags due to the pivoting power law will contribute significantly to the observed phase lags. The sign of the lag changes with frequency as mentioned by Kotov et al. (2001), who evaluated an instantly changing power law for a real light curve.

6.3.3 Cross-Correlation Function

The phase lags depend only on the phase of the Fourier-transform and contain no information on the amplitude. To gain information also on the amplitudes

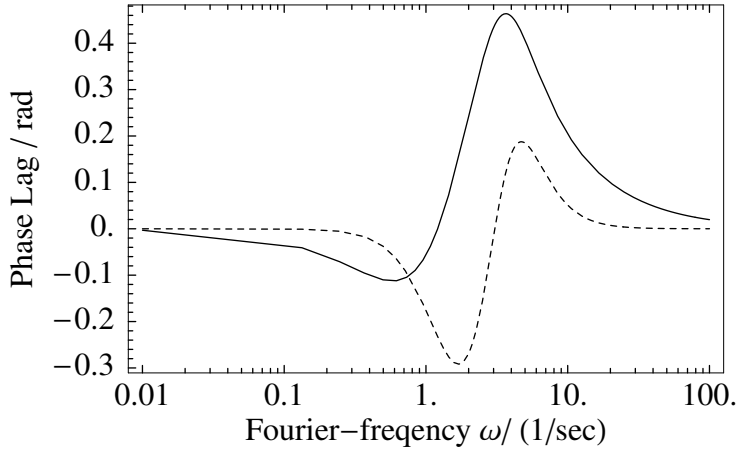


FIGURE 6.2— Difference between the sine and cosine part. The magnitude of the sine lags (dashed) have been magnified by a factor of ten.

we consider the auto-correlation and cross-correlation functions. The cross-correlation function is defined as:

$$C(\epsilon_1, \epsilon_2, \bar{\tau}) = \int (S(\epsilon_1, t) - \langle S(\epsilon_1) \rangle) (S(\epsilon_2, t + \bar{\tau}) - \langle S(\epsilon_2) \rangle) dt. \quad (6.19)$$

We have chosen the signs such that the cross-correlation function between a lower and a higher photon energy peaks to the right if we observe hard lags. Expressed in Fourier-space we find:

$$C(\epsilon_1, \epsilon_2, \bar{\tau}) = \int \hat{S}_{AC}(\epsilon_1, \omega)^* \hat{S}_{AC}(\epsilon_2, \omega) e^{-i\omega\bar{\tau}} d\omega. \quad (6.20)$$

If we insert the expanded expression (6.3) for $\hat{S}(\epsilon, \omega)$ and only consider terms up to $O(\gamma^2)$ we find:

$$C(\epsilon_1, \epsilon_2, \bar{\tau}) = \int \hat{A}_{AC}^* \hat{A}_{AC} d\omega + \int (\hat{A}^* \widehat{\beta A} \ln \epsilon_2 + \widehat{\beta A}^* \hat{A} \ln \epsilon_1)_{AC} e^{-i\omega\bar{\tau}} d\omega. \quad (6.21)$$

For simplicity we have set the reference energy $\epsilon_0 = 1$.

The first component of the integrand represents the auto-correlation func-

tion of the light curve at the reference energy:

$$\int \hat{A}_{AC}^* \hat{A}_{AC} e^{-i\omega\bar{\tau}} d\omega = \int \sum_i \lambda_i^2 \hat{F}^2(\omega) e^{-i\omega\bar{\tau}} =: P(\bar{\tau}). \quad (6.22)$$

The second component takes a longer calculation using the results for $\widehat{\beta A}$ of Appendix 6.7 and is described in Appendix 6.8. With the function $\mathcal{S}(\tau, \bar{\tau})$ defined in the Appendix we find for the cross-correlation function

$$C(\epsilon_1, \epsilon_2, \bar{\tau}) = P(\bar{\tau}) + \gamma (\ln \epsilon_1 P(\bar{\tau} - \tau) + \ln \epsilon_2 P(\bar{\tau} + \tau) + \ln \epsilon_2 \mathcal{S}(\tau, \bar{\tau}) + \ln \epsilon_1 \mathcal{S}(\tau, -\bar{\tau})). \quad (6.23)$$

As described in the Appendix \mathcal{S} peaks at $\bar{\tau} = \tau$ and decays faster than $P(\bar{\tau})$.

Whether the auto-correlation function has a steeper peak for higher photon energies ϵ depends on the parameters. While the terms in the first line of Eq. (6.23) makes the auto-correlation function broader for higher energies ($\sim \log \epsilon$) the terms in the second line have the opposite effect. For small Q and τ the peak is steeper for higher photon energies while for larger values of τ and Q the opposite effect is found.

If the excitations of the oscillator are symmetric, i.e. $\langle \lambda^3 \rangle = 0$, \mathcal{S} vanishes, and only higher order terms contribute to the cross-correlation function. The feature that the cross-correlation function can have a steeper component for higher energies remains in this case as seen in the Monte Carlo simulation.

A numerical evaluation of the cross correlation function with a damping factor of unity is shown in Fig. (6.3). The calculated auto-correlation function is, for the parameters used, steeper for higher energy photons. The cross-correlation function between two energies lies in between and is slightly asymmetric. It is important to note that whether the auto-correlation function is steeper for higher photon energies depends strongly on the parameters, e.g. the look-back time τ .

If one includes a damping factor $\hat{D}(\omega)$ that damps higher frequencies in the response of the power law index, the light curve itself will have less power in high Fourier frequencies for higher energies. Therefore the auto-correlation function will have a flatter peak for higher energies than without a damping factor. The effect described above (steeper auto-correlation function for higher energies due to the \mathcal{S} -term) and the effect of the damping factor can cancel each other partly.

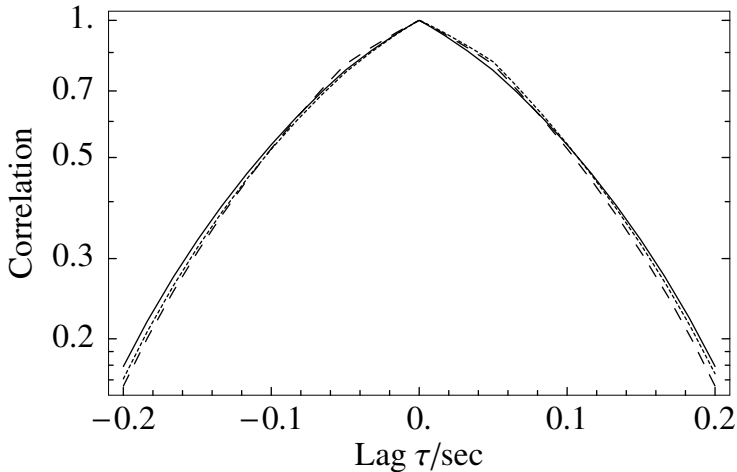


FIGURE 6.3— Numerical evaluation of the calculated cross-correlation function for one Lorentzian only. solid line: low energy auto-correlation function. dashed: higher energy ; dotted: Cross-correlation function

6.3.4 Negative Correlation of Hardness and Flux

In the previous sections we have considered a pivoting power law model with a positive hardness flux correlation ($\gamma > 0$) and a positive look-back time τ . However Zdziarski et al. (2003) observed a negative hardness flux correlation and a pivot point around 50 keV for Cyg X-1 in long term variability (timescale of days). On shorter timescales Li et al. (1999) and Feng et al. (1999) report a negative correlation as well. Therefore a negative correlation can also be present on the short timescales discussed here. A negative hardness/flux correlation ($\gamma < 0$) and a positive look-back time ($\tau > 0$) leads to soft lags. Soft lags have for example been observed in X-ray burst oscillations (Ford 1999). However, the observed lags are approximately 1 rad, much larger than the lags discussed here. So this effect may be due to other mechanisms.

In order to create hard lags with a negative hardness/flux correlation ($\gamma < 0$) one has to use negative look-back times τ . This means that the power law index is changed slightly before the flux changes. Now the pivot point defined by the rms is at higher photon energies as the reference frequency ϵ_0 . If $\epsilon_0 \approx 3$ keV pivot points around 50 keV can be reached. In this case two signs are changed in Eq. (6.18) resulting in hard lags as in the case of $\gamma > 0$. If one changes the sign of τ we have to consider that the analytic behavior of

Eq. (6.16) changes as well. The first term of the phase lag ($\sin \phi \sim \gamma \sin(\omega\tau)$) is the same for negative and positive correlation. However, the second term does not depend on $\Im e^{i\omega\tau}$ as before (Eq. 6.34, see Appendix 6.7). We find instead

$$\sin \phi = \gamma \ln \frac{\epsilon_2}{\epsilon_1} \left(A_{\text{DC}} \sin(\tau\omega) + \frac{\langle \lambda^3 \rangle}{\langle \lambda^2 \rangle} \Im (f_2(\omega)) \right), \quad (6.24)$$

where f_2 is a rational function in ω . If the constant flux A_{DC} dominates the overall flux the non oscillating second term will only be a minor correction. The phase lag from a pivoting power law with negative look-back times τ and negative correlation will therefore yield similar phase lags as before.

Even though the second term of the phase lags has a different structure, the auto-correlation function has the same analytic structure as in the case $\tau > 0$ (Eq. 6.23). Only the function \mathcal{S} has to be changed. As γ is now negative, the first line of Eq. (6.23) already yields a steeper auto-correlation function for higher photon energies ϵ . As the second line depends on γ as well, it can broaden the auto-correlation function. Which one of these effects dominates depends on the parameters used. Compared to the case with a positive hardness flux correlation, the auto-correlation function has a steeper decline for small values of $\bar{\tau}$ (see Fig. 6.4) and a slower one for larger $\bar{\tau}$.

In summary, the two cases positive hardness/flux correlation and positive look-back time and the case with a negative hardness/flux correlation and a negative look-back time have similar hard phase lags. Only the parameters have to be adjusted somewhat differently. However, while in the first case the auto-correlation function is flatter for small lags and steepens for larger lags, the opposite effect happens in the other case. With appropriately chosen parameters both possibilities seem to be able to reproduce the qualitative behavior seen in the observations of Cyg X-1 by Maccarone et al. (2000).

6.4 Monte Carlo Simulations

The analytic results have used a linear approximation for the response of the power law. For observations near the reference photon energy $\frac{\epsilon}{\epsilon_p} \lesssim 1$ and small responses of the power law index $\gamma \ll 1$ this approximation will be valid. However, as one often observes photon energies with $\frac{\epsilon_{\text{high}}}{\epsilon_{\text{low}}} \gtrsim 10$ we created a Monte Carlo simulation. This will also enable us to consider a system with more than one broad Lorentzian. The light curve for one Lorentzian was generated as described by Eq. (6.7). The random variables λ_i are chosen to

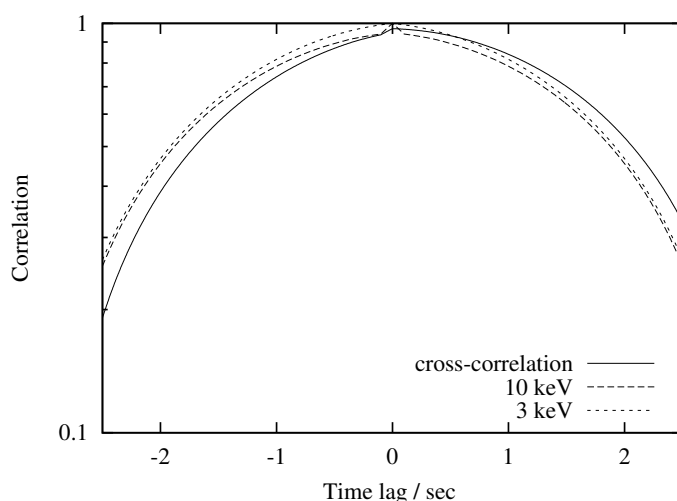


FIGURE 6.4— Monte Carlo simulation of the calculated cross-correlation function for a negative hardness/flux correlation and a negative look-back time.

be the absolute value of a Gaussian distribution and the excitation times t_i are uniformly distributed. Each individual pulse is described by the sum of the cosine and sine damped oscillator ($F = F_c + F_s$). Once the light curve at the reference photon energy is created we can calculate light curves at other photon energies using Eq. (6.1) and derive the phase lags. The comparison between the numerical results and the analytic calculation is shown in Fig. 6.1. We find that the analytic first order approximation and the Monte Carlo simulation are in good agreement.

If one assumes that the different oscillators creating the broad Lorentzians do not interact with each other one can calculate a light curve for a system described by multiple Lorentzians by creating light curves for each Lorentzian separately and then superpose these light curves to get the overall light curve. This is used in the application to Cyg X-1, in Sect. 6.5.

Besides the phase lags we can calculate the cross- and auto-correlation functions of the light curve. The Monte Carlo simulation reproduces the effect seen in the analytic calculations: for the parameters used the auto-correlation function is steeper for higher energy photons than for the low energetic once. In Fig. (6.4) we show the result of the Monte Carlo simulation with a negative look-back time. The cross-correlation function is asymmetric as expected for

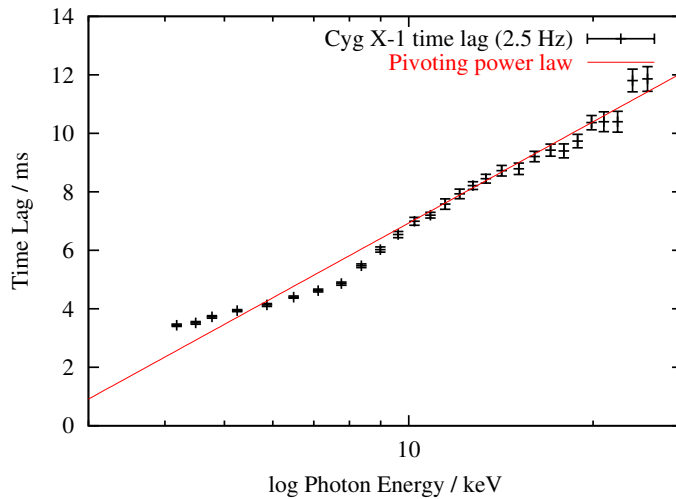


FIGURE 6.5— Time Lags versus photon energy at a Fourier frequency of 2.5 Hz. The solid curve represents the analytic solution for the pivoting power law model with a reference energy of 2.0 keV.

hard lags.

6.5 Applications to BHXRBs

We are now able to apply the model to the BHXRB Cygnus X-1. Throughout this section we use data for Cyg X-1 which was taken from Nowak et al. (1999) and Kotov et al. (2001) for the photon energy dependence of the phase lag.

6.5.1 Photon Energy Dependence of the Phase Lags

The pivoting power law model predicts that the energy dependence of the phase lags is logarithmic (Eq. 6.15). In Fig. 6.5 we show the phase lags measured with a constant Fourier frequency of 2.5 Hz (dots). The solid line represents the pivoting power law model. The reference energy ϵ_0 used for the fit is 2.0 keV. For lower photon energies the accretion disk will become increasingly important and will start to dominate over the power law component. In this regime a simple pivoting power law will not be sufficient to describe the behavior and deviations from the logarithmic energy dependence of the lags are likely.

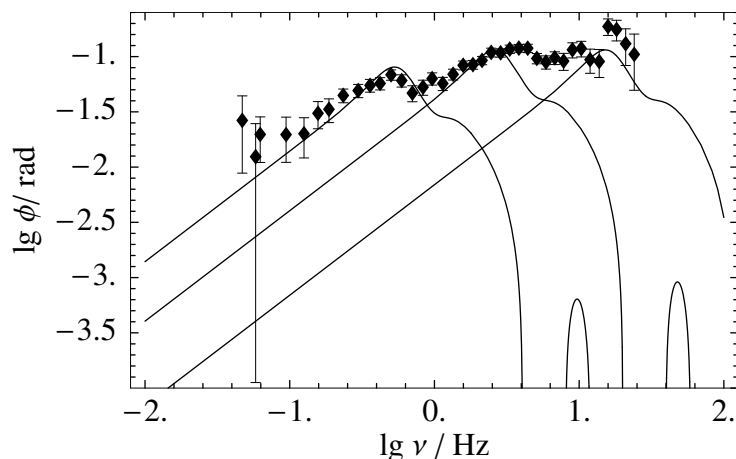


FIGURE 6.6— Illustration for the superposition of the different broad Lorentzians. In the superposition every Lorentzian should dominate the phase lag around its center frequency.

6.5.2 Fourier Frequency Dependence of the Phase Lags

The PSD of Cyg X-1 can be well fitted with four broad Lorentzians (see e.g., Nowak 2000, Belloni et al. 2002 and Pottschmidt et al. 2003). The phase lag from each Lorentzian will dominate the overall phase lag around its center frequency. The idea is illustrated in Fig. 6.6 where we calculated the phase lags for each Lorentzian separately. The look-back time τ is always the same fraction of the center frequency of the Lorentzian, which reduces the number of free parameters. In this plot we assumed that the excitations are similar to those of an instantaneously excited oscillator and used as damping factor a Lorentzian with $Q = 0.25$ (Center frequencies $f = 0.25, 1.2, 7.3$ Hz, $\tau = 0.03 f^{-1}$).

If we assume that the different broad Lorentzians do not interact with each other we can do the superposition with our Monte Carlo simulation. First we generate a separate light curve for each Lorentzian. In this way we have the possibility to consider that each broad Lorentzian has a different look-back time τ , which we assumed to be a fixed fraction of the period of that Lorentzian. The overall light curve is the superposition of the four light curves. The PSD of the artificial light curve is shown in Fig. 6.7. The parameters of the Lorentzians are given in Table 6.1. The pulse of the shot noise is a superposition of the damped sine and cosine oscillator, so its PSD is not exactly a

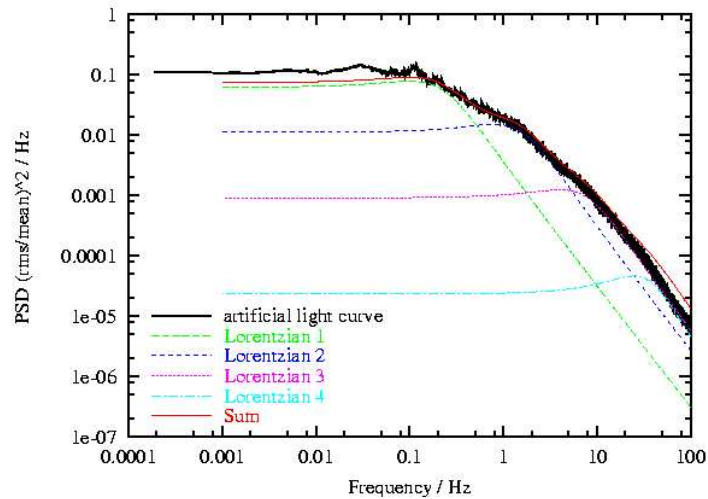


FIGURE 6.7— The PSD of the artificial light curve together with the four broad Lorentzians. For their parameters see Table 6.1.

Lorentzian, but this only leads to small deviations of the overall PSD. The PSD has been used to find the overall normalization of the shot noise.

The damping factor $D(\omega)$ used in the Monte Carlo simulation is a Lorentzian centered around the center-frequency of oscillator creating the broad Lorentzians with the half quality factor as the oscillator itself. The constant power law index α has been fixed to 1.7, and the correlation factor $\gamma = 0.26$. The look-back time was chosen to be $\tau = 0.04f^{-1}$, where f denotes the center frequency of the Lorentzian. In Fig. 6.8 the phase lags from this Monte Carlo simulation are plotted in comparison with the observed values from Nowak et al. (1999). The parameters are summarized in Table 6.1. The peak frequencies, where the Lorentzians contribute mostly to the rms, are also given in this table. The peak frequency ($f_{\text{peak}} = f \sqrt{1/(4Q^2) + 1}$) is often used for frequency correlations (see e.g., Nowak 2000). The parameters of the Lorentzians are within the range of the values given by Pottschmidt et al. (2003). The effect of the fourth Lorentzian on the phase lags is rather small, as this Lorentzian does not dominate the overall PSD at its center frequency.

The used parameters are not unique. For example, a small change of the hardness/flux correlation parameter γ can be compensated by a change of the look-back time τ . Furthermore, the central frequencies of the Lorentzians

TABLE 6.1— The parameters used for Cyg X-1

Lorentzian	1	2	3	4
f_c in Hz	0.1	0.8	4.0	25.0
Q	0.25	0.3	0.3	0.5
R	0.22	0.25	0.16	0.06
f_{peak} in Hz	0.22	1.55	7.7	35.0

needed to fit the phase lags depend on the damping factors and the positions of the other Lorentzians. These parameters were chosen to give a steeper auto-correlation for higher photon energies (see below). If one would choose different fractions of the center frequency of the Lorentzian for the look-back time τ and allows for a different hardness/ flux correlation factor γ for each Lorentzian better fits would be possible.

A similar result for the phase lags can be obtained using a negative hardness flux correlation and a negative look-back time. One possibility would be to choose $\gamma = -0.16$ and $\tau = -0.06f^{-1}$ and to center the Lorentzians given in Table 6.1 at slightly different positions ($f = 0.15, 1.2, 6.0, 25$ Hz).

6.5.3 Auto- and Cross-Correlation Function

In addition to the phase lags we evaluated the auto- and cross-correlation function for the simulated light curves at different photon energies. In Fig. 6.9 we show the auto- and cross-correlation function for the parameters used in Fig. 6.8, here with a positive hardness/flux correlation and a positive look-back time. With these parameters the auto-correlation function is steeper for higher photon energies and the cross-correlation is slightly asymmetric. The plot shows qualitatively the same behavior as the observed correlation shown in Maccarone et al. (2000). However, this behavior depends strongly on the parameters, such as the look-back time τ or even the relative prominence of the different Lorentzians.

6.5.4 Coherence Function

The coherence function measures the linear correlation of the two light curves at different photon energies. For an introduction and a discussion of its prop-

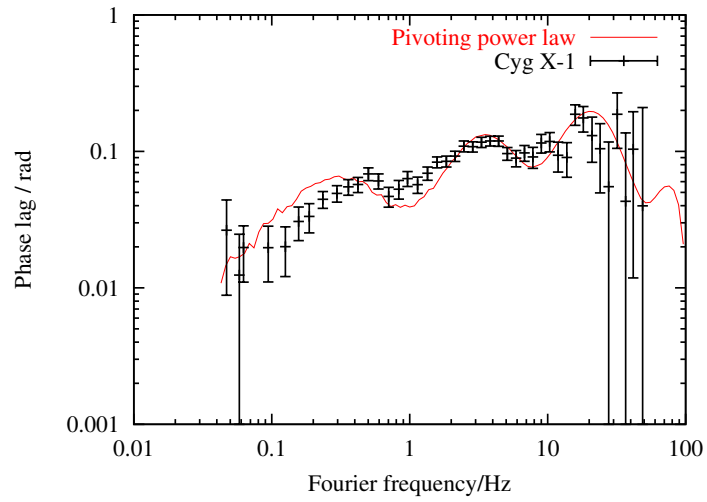


FIGURE 6.8— Phase-lag dependence (0–3.9 keV to 8.2–14.1 keV) on frequency. Four Lorentzians with parameters given in Table 6.1 have been superposed with our Monte Carlo Code. The data were taken from Nowak et al. (1999)

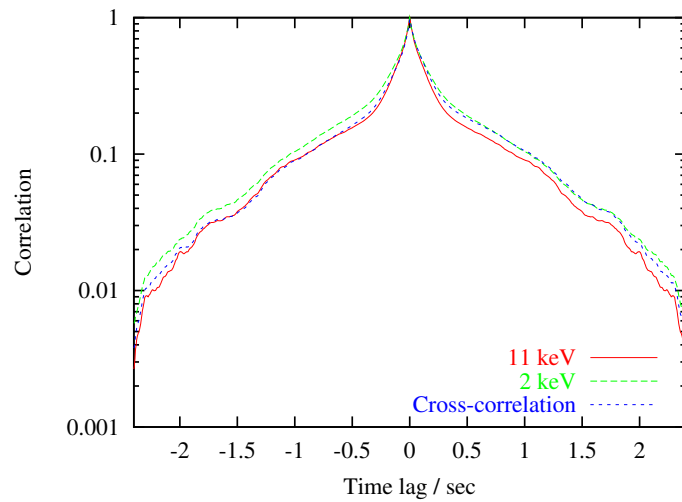


FIGURE 6.9— Auto- and cross-correlation function created by the Monte Carlo simulation. See the Table 6.1 for the used parameters.

erties see Vaughan & Nowak (1997). It is defined as

$$\gamma_I^2(\omega) = \frac{|\langle \hat{S}^*(\epsilon_1, \omega) \hat{S}(\epsilon_2, \omega) \rangle_d|^2}{\langle |\hat{S}(\epsilon_1, \omega)|^2 \rangle_d \langle |\hat{S}(\epsilon_2, \omega)|^2 \rangle_d} \quad (6.25)$$

where $\langle \cdot \rangle_d$ denotes an average over different realizations of the statistical process, e.g. different light-curves. If the coherence function is unity the light-curves at different photon energies are connected by a linear transformation. To evaluate the coherence function for the pivoting power law model we simulated 100 different 5000 second light curves with a time resolution of 5 ms. The result is shown in Fig. 6.10 together with the measured coherence function of Cyg X-1. The highest frequency Lorentzian included in our calculation is centered around 25 Hz. Due to our damping factors the two light-curves are therefore perfectly correlated at higher Fourier frequencies. This leads to the rise of $\gamma_I^2(\omega)$ for higher Fourier frequencies to one. The rise is therefore an artifact of our choice of the damping factors and probably missing higher Lorentzians. In the low Fourier frequency domain (≤ 0.01 Hz) the PSD is usually dominated by a power law noise component (Nowak 2000), which may be responsible for the lower coherence function in this regime. We conclude that the model is consistent with the data in the Fourier frequency regime where the model is valid.

6.5.5 Failed State Transitions

Pottschmidt et al. (2000 & 2002) identified some flares of Cyg X-1 as ‘failed state transitions’. During these flares the X-ray spectrum softens and that the rms amplitude decreases. The PSD is then usually dominated only by the second Lorentzian (peak frequency ≈ 3 Hz) and to some extent the third Lorentzian (peak frequency ≈ 9 Hz). The phase lags during the ‘failed state transitions’ increases significantly in the 3–10 Hz regime, while it stays nearly constant compared to a normal hard state below 1 Hz and above 10 Hz. The third and second Lorentzian dominate the PSD between 3 and 10 Hz. This leads these authors to the conclusion that the increased phase lag can be attributed to these Lorentzians. It has already been pointed out by Nowak (2000) and Pottschmidt et al. (2003) that the phase lags could be reduced due to the superposition of the different Lorentzians. If one Lorentzian starts to dominate the overall PSD the phase lags will therefore increase. For example in Fig. 6.11 we reduced the strength of the first and third Lorentzian ($R = 0.1$) while leaving all other parameters unchanged. This leads to an increase of the phase

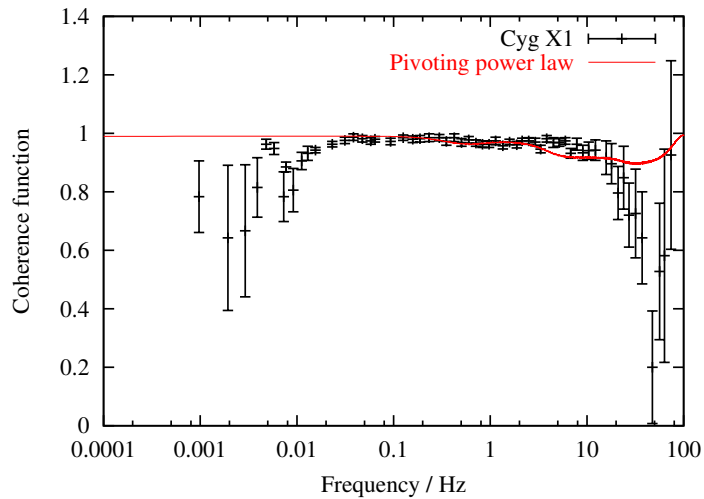


FIGURE 6.10— Coherence Function for a pivoting power law model. See the Table 6.1 for the used parameters.

lags, where the second Lorentzian dominates, but decreases the lags further away. The increase and decrease of the phase lags depend on the other model parameters as well. While increasing lags in the 3–10 Hz regime are observed (Pottschmidt et al. 2003), the decrease can not be found in their plot. However, during state transitions other model parameters may change. It may be that the look-back time τ or the hardness flux correlation increases, resulting in larger lags. To fully understand this intriguing phenomenon a more detailed study is needed.

6.6 Summary and Conclusions

In this chapter we have discussed the effect of a variable pivoting power law in the spectrum of an astrophysical source on its timing behavior, particularly for the Fourier phase lags (see e.g., Miyamoto & Kitamoto 1989), the cross/auto-correlation and coherence function. This model is applied to black hole X-ray binaries. From this approach follows immediately that the Fourier phase lag dependence on photon energy is logarithmic (see also Kotov et al. 2001), which is observed in Cyg X-1. This result is independent of the choice for the response of the power law and the coherence features of the light curve.

To derive the Fourier frequency dependence of the phase lags, the coher-

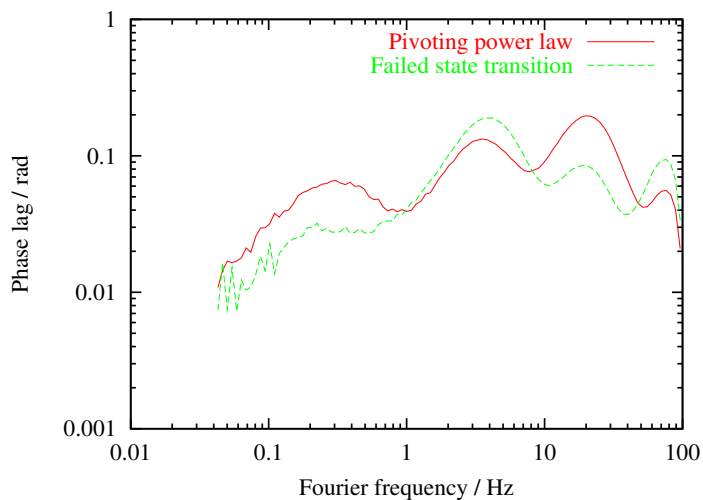


FIGURE 6.11— Comparison of the phase lags from a normal set of Lorentzians and a 'failed state transition', where the Lorentzian two dominates.

ence properties of the light curve are needed. Hints to the coherence of XRBs can be found in the PSD, which can be fitted by a few broad Lorentzians (Nowak 2000, Pottschmidt et al. 2003 or Belloni et al. 2002). A Lorentzian normally arises from a damped oscillator. Therefore, we assume that the variations of the light-curve are generated by randomly excited damped oscillators, i.e. we use a simple shot noise model (see e.g., Lochner et al. 1991) to generate our light curve. The power law index was chosen to respond linearly to flux changes including a response time (τ), i.e. the power law index responds slightly after or before total intensity changes.

The analytic calculations reduce the Fourier phase lags to a simple expression, $\sin \phi \sim \gamma \sin(\omega\tau) \ln \frac{\epsilon_2}{\epsilon_1}$ for one Lorentzian, where γ is the flux/hardness correlation parameter and ω is the Fourier frequency. This law will break down around the center frequency of the Lorentzian, due to an included damping of the response of the power law and stochastic variations of the look-back time τ . The phase lag will therefore simply drop to zero for Fourier frequencies much higher than the center frequency of the Lorentzian.

To obtain hard lags one has to use a positive hardness/flux correlation and a positive response time (response after the change of the flux) or a negative hardness/flux correlation and a negative response time. If the power law index

changes by $\Delta\Gamma \approx 0.2$ around $\Gamma = 1.7$ and the look-back time is of the order of 10% of the period of the excitation we can account for the observed magnitude of the phase lags in Cyg X-1. Soft lags can be achieved by using a negative hardness/flux correlation and a positive response time – or vice versa.

The result for the phase lags of one Lorentzian is fairly independent of the exact shape of the excitations. However, the coherence properties of the light curve become more important if one superposes different Lorentzians, as needed for Cyg X-1. Using four Lorentzians we were able to reproduce the observed hard lags of Cyg X-1 (Nowak et al. 1999) using parameters of the Lorentzians within the published range. Similar hard lags are observed for BL Lacs (Zhang 2002), where the pivoting power law model may be applicable as well. The superposition of the Lorentzians is likely to play an important role in the 'failed state transitions' found by Pottschmidt et al. (2000). During these events one Lorentzian normally dominates the overall PSD, the effect of the superposition is reduced resulting in larger lags.

If one does not allow for a look-back time, a pivoting power law will nevertheless create phase lags of the order of magnitude of the observed values. However, these phase lags change their sign with Fourier frequency, which is not seen in the data. However, when using a pivoting power law model as sometimes used to explain the rms behavior (see e.g., Zdziarski et al. 2003), one has to take these lags into account.

Besides the phase lags we also calculated the auto- and cross-correlation function (see e.g., Maccarone et al. 2000). They show the qualitative correct behavior seen for Cyg X-1. It is important to note, that while the result for the phase lags is fairly independent of the parameters and the form of the damping factor, the auto-correlation function can change its qualitative behavior. For example, if one uses large look-back times and large quality factors Q the higher energy auto-correlation function will have a broader peak than the one for lower energy, the opposite of what observations suggest for XRBs.

The coherence function, which measures the linear correlation between the light-curves at different photon energies (Vaughan & Nowak 1997), has been calculated and compared with observations of Cyg X-1. The model is in agreement with the observations, for Fourier frequencies where the numerical model is valid.

Both models (the jet/synchrotron model and the disk/corona models) predict the existence of a pivoting power law. At least the jet/synchrotron model developed in this thesis creates a rigid power law without spectral breaks (see chapter 2). We have shown that such a rigid power law model is consistent

with the data of Cyg X-1. A more detailed analysis using probably an original light-curve and physical parameters for both models is needed. We also point out, that Cyg X-1 cannot be described by a simple power law (see e.g., Di Salvo et al. 2001), indicating contributions from different emission regimes that most certainly will also complicate the timing behavior.

We conclude that with a rather simple ansatz for a pivoting power law model we can explain many of the complex features in the phase lags, cross-correlation function and coherence function seen in the hard power law emission of XRBs.

6.7 Appendix: Derivation of the phase lags

The Fourier transform of a damped oscillator is a sum of two similar terms. To simplify the calculation let us first consider only the first term

$$F_1(\omega) = \frac{2R\sqrt{Q}\omega_0}{\omega_0 - 2iQ(\omega - \omega_0)}. \quad (6.26)$$

In order to evaluate the equation for the phase lags (6.15) we have to calculate the convolution needed for $\widehat{\beta A}$ (Eq. 6.16):

$$\begin{aligned} \widehat{\beta A} = & \gamma \int e^{i\omega'\tau} F_1(\omega') F_1(\omega - \omega') \sum \lambda_i \lambda_j e^{i(t_i - t_j)\omega' + it_j\omega} d\omega' \\ & + A_{\text{DC}} F_1(\omega) \sum \lambda_j e^{it_j\omega}. \end{aligned} \quad (6.27)$$

The excitation times t_i are random variables, therefore the sum over the non-diagonal elements will yield zero as the random phases average out.

The integral can be solved using complex analysis. It has two poles: one from $F_1(\omega')$ at $\omega' = \omega_0 - i\frac{\omega_0}{2Q}$ and the other from $F_1(\omega - \omega')$ near $\omega' = \omega - \omega_0 + i\frac{\omega_0}{2Q}$. If τ is positive, we could close the integral path with a half circle for positive imaginary parts. This path only includes the pole at $\omega' = \omega - \omega_0 + i\frac{\omega_0}{2Q}$. Now we can apply the residual theorem, and find for the integral

$$\frac{2\pi R^2 \omega_0}{\omega_0 - iQ(\omega - 2\omega_0)} e^{-\tau\frac{\omega_0}{2Q} + i\tau(\omega - \omega_0)}. \quad (6.28)$$

Inserting this expression in Eq. (6.15) we get

$$\sin \phi = \gamma \ln \frac{\epsilon_2}{\epsilon_1} \left(A_{\text{DC}} \sin(\tau\omega) + \frac{\Im \left(\frac{2\pi R^2 \omega_0}{\omega_0 - iQ(\omega - 2\omega_0)} e^{-\tau \frac{\omega_0}{2Q} + i\tau(\omega - \omega_0)} F_1^*(\omega) \sum \lambda_i^3 \right)}{\sum \lambda_i^2 F_1^* F_1(\omega)} \right). \quad (6.29)$$

The real instantaneously excited, damped oscillator is a sum of two terms like $F_1(\omega)$. The result will therefore consist of four terms, which can be calculated in analogy. We find for a positive look-back time τ :

$$\sin \phi = \gamma \ln \frac{\epsilon_2}{\epsilon_1} \left(A_{\text{DC}} \sin(\tau\omega) + \frac{\langle \lambda^3 \rangle}{\langle \lambda^2 \rangle} \Im \left(e^{i\tau\omega} f_1(\omega) \right) \right), \quad (6.30)$$

with

$$f_1(\omega) = \frac{\pi R^2 \omega_0 F^*(\omega) e^{-\tau \frac{\omega_0}{2Q}}}{2F^* F(\omega)} \left(\frac{e^{-i\tau\omega_0}}{\omega_0 - iQ(\omega - 2\omega_0)} + \frac{e^{i\tau\omega_0}}{\omega_0 - iQ(\omega + 2\omega_0)} + \frac{(e^{i\tau\omega_0} + e^{-i\tau\omega_0})}{\omega_0 - iQ\omega} \right). \quad (6.31)$$

The other real solution for the damped oscillator is the sine term (see Eq. 6.9). For this solution one has to change the two last signs and include a factor $-i$. The only fast changing part of the second term of Eq. (6.30) is $e^{i\tau\omega}$. Therefore, the dominant part will be $\sin(\tau\omega)$ as the first term.

In the second case, $\tau < 0$ we have to close the integral path in Eq. (6.27) with a half circle in the negative imaginary plane. The integral path now includes the pole at $\omega' = \omega_0 - i\frac{\omega_0}{2Q}$ and the residual theorem yields:

$$\frac{2\pi R^2 \omega_0}{\omega_0 - iQ(\omega - 2\omega_0)} e^{\tau \frac{\omega_0}{2Q} + i\tau\omega_0}, \quad (6.32)$$

and we find for the phase lags:

$$\sin \phi = \gamma \ln \frac{\epsilon_2}{\epsilon_1} \left(A_{\text{DC}} \sin(\tau\omega) + \frac{\Im \left(\frac{2\pi R^2 \omega_0}{\omega_0 - iQ(\omega - 2\omega_0)} e^{\tau \frac{\omega_0}{2Q} + i\tau\omega_0} F_1(\omega) \sum \lambda_i^3 \right)}{\sum \lambda_i^2 F_1^* F_1(\omega)} \right). \quad (6.33)$$

The real instantaneously excited oscillator yields for this case:

$$\sin \phi = \gamma \ln \frac{\epsilon_2}{\epsilon_1} \left(A_{\text{DC}} \sin(\tau\omega) + \frac{\langle \lambda^3 \rangle}{\langle \lambda^2 \rangle} \mathfrak{J}(f_2(\omega)) \right), \quad (6.34)$$

with

$$f_2(\omega) = \frac{\pi R^2 \omega_0 e^{\tau \frac{\omega_0}{2Q}}}{2F^* F(\omega)} \left(\frac{e^{i\tau\omega_0} F(\omega)}{\omega_0 - iQ(\omega - 2\omega_0)} + \frac{e^{-i\tau\omega_0} F(\omega)}{\omega_0 - iQ(\omega + 2\omega_0)} + \frac{(e^{-i\tau\omega_0} + e^{i\tau\omega_0})F(\omega)}{\omega_0 - iQ\omega} \right). \quad (6.35)$$

6.8 Appendix: Derivation of the cross-correlation function

In order to evaluate the second integral of the cross-correlation function (Eq. 6.21)

$$\int \left(\widehat{A}^* \widehat{\beta A} \ln \epsilon_2 + \widehat{\beta A}^* \widehat{A} \ln \epsilon_1 \right)_{\text{AC}} e^{-i\omega\bar{\tau}} d\omega, \quad (6.36)$$

we start with Eq. (6.27) for $\widehat{\beta A}$. Using this result it is possible to evaluate the integral with the same arguments as used for $\widehat{\beta A}$. We define three supplementary functions

$$\mathcal{H}_1(\tau, \bar{\tau}) = \frac{e^{-i\bar{\tau}\omega_0}}{3\omega_0 + i2Q\omega_0} + \frac{e^{-i(2\tau-\bar{\tau})\omega_0}}{3\omega_0 + 6iQ\omega_0} + 2\text{Cos}(\tau\omega_0) \frac{e^{i(\tau-\bar{\tau})\omega_0}}{3\omega_0 - 2iQ\omega_0} + \text{cc}. \quad (6.37)$$

$$\mathcal{H}_2(\tau, \bar{\tau}) = \frac{e^{i\tau\omega_0 - 2i\bar{\tau}\omega_0}}{3\omega_0 + 2iQ\omega_0} + \frac{e^{i\tau\omega_0 - 2i\bar{\tau}\omega_0}}{3\omega_0 + 6iQ\omega_0} + 2\text{Cos}(\tau\omega_0) \frac{1}{3\omega_0 - 2iQ\omega_0} + \text{cc}, \quad (6.38)$$

where cc denotes the complex conjugate, and

$$S(\tau, \bar{\tau}) = R^3 \omega_0^{3/2} Q^{-1/2} \pi^2 e^{-\tau \frac{\omega_0}{2Q}} \left(\Theta_{\tau-\bar{\tau}} e^{-(\tau-\bar{\tau}) \frac{\omega_0}{2Q}} \mathcal{H}_1(\tau, \bar{\tau}) + \Theta_{\bar{\tau}-\tau} e^{2(\tau-\bar{\tau}) \frac{\omega_0}{2Q}} \mathcal{H}_2(\tau, \bar{\tau}) \right) \sum \lambda^3, \quad (6.39)$$

where Θ_x is the step function. It is defined as $\Theta_x = 0$ for $x < 0$ and $\Theta_x = 1$ otherwise. We find for the cross-correlation function:

$$C(\epsilon_1, \epsilon_2, \bar{\tau}) = P(\bar{\tau}) + \gamma(\ln \epsilon_1 P(\bar{\tau} - \tau) + \ln \epsilon_2 P(\bar{\tau} + \tau)) + \gamma(\ln \epsilon_2 S(\tau, \bar{\tau}) + \ln \epsilon_1 S(\tau, -\bar{\tau})). \quad (6.40)$$

The first line of this equation will broaden the auto-correlation function ($\epsilon_1 = \epsilon_2$) for higher photon energies, positive look-back times τ , and positive hardness flux correlation $\gamma > 0$. However, $S(\tau, \bar{\tau})$ peaks at $\bar{\tau} = \tau$ and will decline faster for higher $\tau > \bar{\tau}$ than $P(\tau)$ (falls with $e^{-\bar{\tau}}$) due to the factor $e^{2(\tau-\bar{\tau})}$. This leads to steeper auto-correlation functions for higher ϵ . Which effect dominates depends on the parameters used.

For negative look-back times τ and $\gamma < 0$ we have to use Eq. (6.32) for the integral of Eq. (6.27) resulting in a different cross-correlation function. The overall form will stay the same, as Eq. (6.32) differs from Eq. (6.28) only by the argument in the exponential function – the analytic behavior (poles) is the same. Here the first line of Eq. (6.40) leads to a steeper auto-correlation function ($\gamma < 0$) while the second line has the opposite effect.

7

Conclusions

In this thesis we have extended the coupled disk/jet model of Falcke & Biermann (1995) and explored the implication of our model for AGN and black hole XRBs. As the process of the jet-launching is still under debate, we have parameterized the connection between the jet power and the accretion rate. Once the jet power and its speed and geometry are known, we can derive the jet emission and its dependence on the main parameters of the system: the black hole mass and accretion rate.

The model can be used to unify all jet-dominated sources. For very low accretion rates (a few percent Eddington) it has been suggested that the inner parts of the accretion flow turn into an optically thin, geometrically thick accretion flow (e.g., Esin et al. 1997). As this flow is probably radiatively inefficient, the jet emission can dominate the total emitted power, and the jet can be observed nearly unperturbed. Thus, this class of sources is the natural testbed for the developed model. In the zoo of all accreting black holes we classify the low/hard state XRBs, low luminosity AGN, FR-I radio galaxies, and their beamed counterparts the BL Lac objects as ‘jet-dominated’. Using this classification and the scaling laws we have developed, we can establish a universal radio/X-ray correlation of these sources. The theoretical predictions match the observed correlation very well. Thus, the underlying assumption of a constant geometry of the system in units of the Schwarzschild radius is reasonable. This supports the paradigm that the main parameters are indeed the black hole mass and the accretion rate. Both parameters can change over more than 9 orders of magnitude.

Following the idea that AGN and XRBs mainly differ by their sizes, we

have to assume that similar to Blazars - AGN where the relativistic jet points towards the observer - there should be microblazars. XRBS with their relativistic jet pointing towards the observer should show very bright X-ray emission, if the X-rays originate from the jet. The expected microblazars can probably be found among the recently discovered ULXs. As stellar mass black holes are more X-ray loud than AGN, microblazars should be detected in the X-rays while Blazars are best observed in the radio regime. We have shown that this concept can explain most of the recently found ULXs. The parent population - the black hole XRBS - is large enough to create enough ULXs.

The different possible explanations for ULXs, namely microblazars, super-Eddington accretion flows or intermediate-mass black holes, could be tested by finding compact radio counterparts of the X-ray sources. Compact radio emission is a direct hint to non-thermal emission and to the jet phenomenon. In the microblazar picture, however, the parent population of ULXs are the strongly accreting black hole XRBS. Those objects are typically radio transients, e.g., they show radio flares of 10-100 times their quiescent value. We have therefore monitored a well defined sample of ULXs for eight times over 5 months. Besides the already published flare in M82 (Kronberg & Sramek 1985) we have not detected another flare. These non-detections can be translated to an upper limit on the number of bright radio flares ($> 3.8 \times 10^{17}$ W/Hz) an average ULX has per year: $11 (\delta t_{\text{flare}} / (2 \text{days}))$, where δt_{flare} is the timescale of a flare. GRS 1915 has two to three bright radio flares a year, far less than our upper limit. In M82 we find supernova remnants with positions in agreement with the Chandra X-ray positions for two of the three ULXs. This supports the idea that the ULX phenomenon is connected to star formation. Besides these two sources we do not detect any continuous radio emission from the other ULXs. These non-detections are in agreement with the values estimated from the developed radio/X-ray correlation. Any detection would have supported the idea that these sources are indeed intermediate-mass black holes. The continuous radio emission from ULXs is undetectable for current radio telescopes. Only a new generation of telescopes (e.g., the SKA) will be able to detect the weak radio cores ($< 10 \mu\text{Jy}$) expected from the beamed emission of microblazars.

Finally, we have tested the disk/jet model by looking at short-term X-ray variability of black hole XRBS and blazars. As according to this model the X-rays are created by synchrotron emission, the spectrum can always be described by a power law. This power law can only vary in intensity and power law index. We considered a pivoting power law model where the intensity and the power law index are correlated, but where the power law index responds

with a slight delay to the intensity. Such a pivoting power law shows most of the observed statistical properties of XRBs. It can reproduce the Fourier time lags, the auto- and cross-correlation function and the coherence function. Thus, the observed variability pattern can indeed be created by a jet.

This thesis is the next step to the unification of all accreting objects. Here, the jet-dominated sources have been unified, and the underlying model has been tested for XRBs and AGN. This can be the basis of a broader unification of all accreting objects in the universe: from low power young stellar objects to huge and powerful quasars.

List of Figures

1.1	The quasar-microquasar analogy	3
1.2	The low and high states of Cyg X-1	4
1.3	Radio map and spectra of Cyg A	5
1.4	Sketch of the low and high state	6
1.5	Synchrotron and inverse Compton emission features	7
2.1	Sketch of the different jet geometries	21
2.2	GRS 1915 Radio/Optical/X-rays	22
2.3	Sketch of the SED of a jet:synchrotron and inverse-Compton emission	24
2.4	The stable regime of jets	35
2.5	The dominant radiation process	36
2.6	Quantitative analysis of the dominant radiation process	37
2.7	Jet/Disk Luminosities	38
2.8	The dominant radiation process for an ADAF/SS disk combination	39
3.1	Radio/X-ray correlation for XRBs	44
3.2	Proposed unification scheme	46
3.3	Black hole mass and power scaling of the jet spectrum	48
3.4	Uncorrected Radio/X-ray correlation	61
3.5	Mass corrected Radio/X-ray correlation	62
3.6	The effect of relativistic boosting	62
3.7	Scaling of the AGN X-ray flux by 10^7	63
3.8	Mass estimate from the radio/X-ray correlation	63

4.1	Comparison of the model of the luminosity function with the data	72
4.2	Intermediate-mass black holes fit the luminosity function . . .	73
4.3	Contribution of the low and the high state	74
5.1	Map of M82 in the X-rays	80
5.2	The double source in NGC 4736	83
5.3	Radio/X-ray correlation for ULXs	88
5.4	Light-curve of NGC 4736	91
6.1	Phase lag dependence on the Fourier frequency	101
6.2	Difference between the sine and cosine pulse shapes	103
6.3	Numerical evaluation of the calculated cross-correlation function for one Lorentzian only	105
6.4	Monte Carlo simulation of the cross-correlation function for negative hardness/flux correlation and negative look-back time	107
6.5	Time Lags versus photon energy	108
6.6	Illustration for the superposition of the different broad Lorentzians	109
6.7	The PSD of the artificial light curve	110
6.8	Phase-lag dependence on Fourier frequency	112
6.9	Auto- and cross-correlation function	112
6.10	Coherence Function	114
6.11	Comparison of the phase lags from a normal set of Lorentzians and a 'failed state transition'	115

List of Tables

3.1	Source list used for Radio/X-ray correlation	56
5.1	Positions of the observed ULXs	77
5.2	Observing Dates of the different Epochs	78
5.3	RMS flux values	78
5.4	Radio and X-ray detections in M82	82
5.5	Radio flux of NGC 4736	92
6.1	The parameters used for Cyg X-1	111

Bibliography

- Abramowicz, M., Kluzniak, W., McClintock, J., & Remillard, R. 2004, *astro-ph/0402012*
- Abramowicz, M. A., Czerny, B., Lasota, J. P., & Szuszkiewicz, E. 1988, *ApJ*, 332, 646
- Aharonian, F. A. 2002, *MNRAS*, 332, 215
- Antonucci, R. 1993, *ARA&A*, 31, 473
- Bach, U. 2004, PhD Thesis
- Bachiller, R. 1996, *ARA&A*, 34, 111
- Baganoff, F. K., Bautz, M. W., Brandt, W. N., et al. 2001, *Nat.*, 413, 45
- Becker, R. H., Helfand, D. J., White, R. L., Gregg, M. D., & Laurent-Muehleisen, S. A. 2003, *VizieR Online Data Catalog*, 8071, 0
- Begelman, M. C., Blandford, R. D., & Rees, M. J. 1984, *Reviews of Modern Physics*, 56, 255
- Begelman, M. C. & Kirk, J. G. 1990, *ApJ*, 353, 66
- Belloni, T., Psaltis, D., & van der Klis, M. 2002, *ApJ*, 572, 392
- Biermann, P. L., Strom, R. G., & Falcke, H. 1995, *A&A*, 302, 429
- Blandford, R. D. & Königl, A. 1979, *ApJ*, 232, 34

- Blandford, R. D., Netzer, H., Woltjer, L., Courvoisier, T. J.-L., & Mayor, M. 1990, *Active Galactic Nuclei* (Saas-Fee Advanced Course 20. Lecture Notes 1990. Swiss Society for Astrophysics and Astronomy, XII, 280 pp. 97 figs.. Springer-Verlag Berlin Heidelberg New York)
- Blandford, R. D. & Rees, M. J. 1974, *MNRAS*, 169, 395
- Böttcher, M., Jackson, D. R., & Liang, E. P. 2003, *ApJ*, 586, 389
- Bower, G. C., Falcke, H., Herrnstein, R. M., et al. 2004, *Science*, 304, 704
- Carilli, C. L., Perley, R. A., Dreher, J. W., & Leahy, J. P. 1991, *ApJ*, 383, 554
- Chiaberge, M., Capetti, A., & Celotti, A. 1999, *A&A*, 349, 77
- Chiang, J., Reynolds, C. S., Blaes, O. M., et al. 2000, *ApJ*, 528, 292
- Cohen, M. H., Linfield, R. P., Moffet, A. T., et al. 1977, *Nat.*, 268, 405
- Colbert, E. J. M. & Mushotzky, R. F. 1999, *ApJ*, 519, 89
- Colbert, E. J. M., Petre, R., Schlegel, E. M., & Ryder, S. D. 1995, *ApJ*, 446, 177
- Colbert, E. J. M. & Ptak, A. F. 2002, *ApJS*, 143, 25
- Corbel, S., Nowak, M. A., Fender, R. P., Tzioumis, A. K., & Markoff, S. 2003, *A&A*, 400, 1007
- Dermer, C. D. & Schlickeiser, R. 2002, *ApJ*, 575, 667
- Di Salvo, T., Done, C., Życki, P. T., Burderi, L., & Robba, N. R. 2001, *ApJ*, 547, 1024
- Di Stefano, R., Kong, A. K. H., Garcia, M. R., et al. 2002, *ApJ*, 570, 618
- Ebisuzaki, T., Makino, J., Tsuru, T. G., et al. 2001, *ApJ*, 562, L19
- Esin, A. A., McClintock, J. E., & Narayan, R. 1997, *ApJ*, 489, 865+
- Fabbiano, G. 1989, *ARA&A*, 27, 87
- Fabian, A. C., Iwasawa, K., Reynolds, C. S., & Young, A. J. 2000, *PASP*, 112, 1145

- Falcke, H. 1996, *ApJ*, 464, L67
- Falcke, H. & Biermann, P. L. 1995, *A&A*, 293, 665
- Falcke, H. & Biermann, P. L. 1996, *A&A*, 308, 321
- Falcke, H. & Biermann, P. L. 1999, *A&A*, 342, 49
- Falcke, H., Gopal-Krishna, & Biermann, P. L. 1995a, *A&A*, 298, 395
- Falcke, H., Körding, E., & Markoff, S. 2004, *A&A*, 414, 895
- Falcke, H., Malkan, M. A., & Biermann, P. L. 1995b, *A&A*, 298, 375
- Falcke, H. & Markoff, S. 2000, *A&A*, 362, 113
- Falcke, H., Nagar, N. M., Wilson, A. S., & Ulvestad, J. S. 2000, *ApJ*, 542, 197
- Falcke, H., Sherwood, W., & Patnaik, A. R. 1996, *ApJ*, 471, 106
- Fanaroff, B. L. & Riley, J. M. 1974, *MNRAS*, 167, 31P
- Fender, R., Wu, K., Johnston, H., et al. 2004, *Nat.*, 427, 222
- Fender, R. P. 2001, *MNRAS*, 322, 31
- Fender, R. P., Gallo, E., & Jonker, P. G. 2003, *MNRAS*, 343, L99
- Fender, R. P., Garrington, S. T., McKay, D. J., et al. 1999, *MNRAS*, 304, 865
- Feng, Y. X., Li, T. P., & Chen, L. 1999, *ApJ*, 514, 373
- Ferrarese, L. & Merritt, D. 2000, *ApJ*, 539, L9
- Ford, E. C. 1999, *ApJ*, 519, L73
- Fossati, G., Maraschi, L., Celotti, A., Comastri, A., & Ghisellini, G. 1998, *MNRAS*, 299, 433
- Freedman, W. L., Wilson, C. D., & Madore, B. F. 1991, *ApJ*, 372, 455
- Frontera, F., Palazzi, E., Zdziarski, A. A., et al. 2001, *ApJ*, 546, 1027
- Gallo, E., Fender, R. P., & Pooley, G. G. 2003, *MNRAS*, 344, 60
- Gao, Y., Wang, Q. D., Appleton, P. N., & Lucas, R. A. 2003, *ApJ*, 596, L171

- Gebhardt, K., Bender, R., Bower, G., et al. 2000, *ApJ*, 539, L13
- Ghisellini, G., Celotti, A., Fossati, G., Maraschi, L., & Comastri, A. 1998, *MNRAS*, 301, 451
- Ghisellini, G., Padovani, P., Celotti, A., & Maraschi, L. 1993, *ApJ*, 407, 65
- Gilfanov, M. 2004, astro-ph/0403552
- Griffiths, R. E., Ptak, A., Feigelson, E. D., et al. 2000, *Science*, 290, 1325
- Grimm, H.-J., Gilfanov, M., & Sunyaev, R. 2002, *A&A*, 391, 923
- Gursky, H. & Schwartz, D. A. 1977, *ARA&A*, 15, 541
- Haardt, F. & Maraschi, L. 1991, *ApJ*, 380, L51
- Heinz, S. 2002, *A&A*, 388, L40
- Ho, L. C. 1999, *ApJ*, 516, 672
- Ho, L. C., Filippenko, A. V., & Sargent, W. L. 1995, *ApJS*, 98, 477
- Homan, J., Wijnands, R., van der Klis, M., et al. 2001, *ApJS*, 132, 377
- Hynes, R. I., Steeghs, D., Casares, J., Charles, P. A., & O'Brien, K. 2003, *ApJ*, 583, L95
- Jackson, J. 1975, *Classical Electrodynamics* (John Wiley, New York)
- Jokipii, J. R. 1987, *ApJ*, 313, 842
- Junor, W., Biretta, J. A., & Livio, M. 1999, *Nat.*, 401, 891
- Kaaret, P., Corbel, S., Prestwich, A. H., & Zezas, A. 2003, *Science*, 299, 365
- Kaiser, C. R. & Alexander, P. 1997, *MNRAS*, 286, 215
- Kellermann, K., Lister, M., Homan, D., Vermeulen, R., & Cohen, M. 2004, preprint, astro
- Kellermann, K. I., Sramek, R., Schmidt, M., Shaffer, D. B., & Green, R. 1989, *AJ*, 98, 1195
- King, A. R. 2004, *MNRAS*, 347, L18

- King, A. R., Davies, M. B., Ward, M. J., Fabbiano, G., & Elvis, M. 2001, *ApJ*, 552, L109
- Königl, A. 1980, *Phys. Fluids* 23,6
- Körding, E. & Falcke, H. 2004, *A&A*, 414, 795
- Körding, E., Falcke, H., & Markoff, S. 2002, *A&A*, 382, L13
- Körding, E., Colbert, E., & Falcke, F. 2004, in prep
- Kormendy, J. & Richstone, D. 1995, *ARA&A*, 33, 581
- Kotov, O., Churazov, E., & Gilfanov, M. 2001, *MNRAS*, 327, 799
- Krichbaum, T. P., Graham, D. A., Witzel, A., et al. 1998, *A&A*, 335, L106
- Kronberg, P. P. & Sramek, R. A. 1985, *Science*, 227, 28
- Kronberg, P. P. & Wilkinson, P. N. 1975, *ApJ*, 200, 430
- Kubota, A., Mizuno, T., Makishima, K., et al. 2001, *ApJ*, 547, L119
- Kylafis, N. D. & Klimis, G. S. 1987, *ApJ*, 323, 678
- Lamer, G., McHardy, I. M., Uttley, P., & Jahoda, K. 2003, *MNRAS*, 338, 323
- Landt, H., Padovani, P., & Giommi, P. 2002, *MNRAS*, 336, 945
- Li, T. P., Feng, Y. X., & Chen, L. 1999, *ApJ*, 521, 789
- Lind, K. R. & Blandford, R. D. 1985, *ApJ*, 295, 358
- Lochner, J. C., Swank, J. H., & Szymkowiak, A. E. 1991, *ApJ*, 376, 295
- Ma, C., Arias, E. F., Eubanks, T. M., et al. 1998, *AJ*, 116, 516
- Maccarone, T. J. 2003, *A&A*, 409, 697
- Maccarone, T. J. & Coppi, P. S. 2003, *MNRAS*, 338, 189
- Maccarone, T. J., Coppi, P. S., & Poutanen, J. 2000, *ApJ*, 537, L107
- Maccarone, T. J., Gallo, E., & Fender, R. 2003, *MNRAS*, 345, L19
- Makishima, K., Kubota, A., Mizuno, T., et al. 2000, *ApJ*, 535, 632

- Malzac, J. & Jourdain, E. 2000, *A&A*, 359, 843
- Mannheim, K., Biermann, P. L., & Kruehls, W. M. 1991, *A&A*, 251, 723
- Maraschi, L., Fossati, G., Tavecchio, F., et al. 1999, *ApJ*, 526, L81
- Marcha, M. J. M., Browne, I. W. A., Impey, C. D., & Smith, P. S. 1996, *MNRAS*, 281, 425
- Markoff, S., Falcke, H., & Fender, R. 2001a, *A&A*, 372, L25
- Markoff, S., Falcke, H., Fender, R., & Biermann, P. 2001b, to appear in: Proceeding of the 27.th Cosmic Ray Conference (ICRC), Hamburg, Germany
- Markoff, S., Nowak, M., Corbel, S., Fender, R., & Falcke, H. 2003, *A&A*, 397, 645
- Marscher, A. P. & Gear, W. K. 1985, *ApJ*, 298, 114
- Matsumoto, H., Tsuru, T. G., Koyama, K., et al. 2001, *ApJ*, 547, L25
- McHardy, I. M., Papadakis, I. E., Uttley, P., Page, M. J., & Mason, K. O. 2004, *MNRAS*, 348, 783
- Meier, D. L., Koide, S., & Uchida, Y. 2001, *Science*, 291, 84
- Melia, F. & Falcke, H. 2001, *ARA&A*, 39, 309
- Merloni, A., Heinz, S., & di Matteo, T. 2003, *MNRAS*, 345, 1057
- Merritt, D. & Ferrarese, L. 2001, *ApJ*, 547, 140
- Miller, J. M., Fabbiano, G., Miller, M. C., & Fabian, A. C. 2003, *ApJ*, 585, L37
- Miller, J. M., Fox, D. W., Di Matteo, T., et al. 2001, *ApJ*, 546, 1055
- Miller, P., Rawlings, S., & Saunders, R. 1993, *MNRAS*, 263, 425
- Mioduszewski, A. J., Rupen, M. P., Hjellming, R. M., Pooley, G. G., & Waltman, E. B. 2001, *ApJ*, 553, 766
- Mirabel, I. F., Bandyopadhyay, R., Charles, P. A., Shahbaz, T., & Rodriguez, L. F. 1997, *ApJ*, 477, L45

- Mirabel, I. F. & Rodríguez, L. F. 1999, *ARA&A*, 37, 409
- Mirabel, I. F. & Rodríguez, L. F. 1998, *Nat.*, 392, 673
- Miyamoto, S., Kimura, K., Kitamoto, S., Dotani, T., & Ebisawa, K. 1991, *ApJ*, 383, 784
- Miyamoto, S. & Kitamoto, S. 1989, *Nat.*, 342, 773
- Miyoshi, M., Moran, J., Herrnstein, J., et al. 1995, *Nat.*, 373, 127
- Mizuno, T., Kubota, A., & Makishima, K. 2001, *ApJ*, 554, 1282
- Mizuno, T., Ohnishi, T., Kubota, A., Makishima, K., & Tashiro, M. 1999, *PASJ*, 51, 663
- Morris, S. L., Stocke, J. T., Gioia, I. M., et al. 1991, *ApJ*, 380, 49
- Nagar, N. M., Falcke, H., Wilson, A. S., & Ho, L. C. 2000, *ApJ*, 542, 186
- Nagar, N. M., Falcke, H., Wilson, A. S., & Ulvestad, J. S. 2002, *A&A*, 392, 53
- Nagar, N. M., Wilson, A. S., & Falcke, H. 2001, *ApJ*, 559, L87
- Narayan, R. & Heyl, J. S. 2002, *ApJ*, 574, L139
- Narayan, R. & Yi, I. 1994, *ApJ*, 428, L13
- Narayan, R. & Yi, I. 1995, *ApJ*, 452, 710+
- Negoro, H., Kitamoto, S., & Mineshige, S. 2001, *ApJ*, 554, 528
- Nolan, P. L., Gruber, D. E., Matteson, J. L., et al. 1981, *ApJ*, 246, 494
- Nowak, M. A. 1995, *PASP*, 107, 1207+
- Nowak, M. A. 2000, *MNRAS*, 318, 361
- Nowak, M. A., Vaughan, B. A., Wilms, J., Dove, J. B., & Begelman, M. C. 1999, *ApJ*, 510, 874
- Ogley, R. N., Bell Burnell, S. J., Spencer, R. E., et al. 2001, *MNRAS*, 326, 349
- Pacholczyk, A. G. 1970, *Radio Astrophysics* (San Francisco: W.H. Freeman and Company)

- Pence, W. D., Snowden, S. L., Mukai, K., & Kuntz, K. D. 2001, *ApJ*, 561, 189
- Perley, R. A., Dreher, J. W., & Cowan, J. J. 1984, *ApJ*, 285, L35
- Pottschmidt, K., Wilms, J., Nowak, M. A., et al. 2000, *A&A*, 357, L17
- Pottschmidt, K., Wilms, J., Nowak, M. A., et al. 2003, *A&A*, 407, 1039
- Pounds, K. A., Done, C., & Osborne, J. P. 1995, *MNRAS*, 277, L5
- Poutanen, J. 1998, in *Theory of Black Hole Accretion Disks*, Cambridge University Press, 100
- Poutanen, J. 2002, *MNRAS*, 332, 257
- Predehl, P., Burwitz, V., Paerels, F., & Trümper, J. 2000, *A&A*, 357, L25
- Prugniel, P., Zasov, A., Busarello, G., & Simien, F. 1998, *A&AS*, 127, 117
- Psaltis, D. & Norman, C. 2002, *astro-ph/0001391*
- Rachen, J. P. & Biermann, P. L. 1993, *A&A*, 272, 161
- Reynolds, C. S., Loan, A. J., Fabian, A. C., et al. 1997, *MNRAS*, 286, 349
- Roberts, T. P. & Warwick, R. S. 2000, *MNRAS*, 315, 98
- Rodriguez, L. F., Gerard, E., Mirabel, I. F., Gomez, Y., & Velazquez, A. 1995, *ApJS*, 101, 173
- Rybicki, G. B. & Lightman, A. P. 1979, *Radiative processes in astrophysics* (New York, Wiley-Interscience, 1979. 393 p.)
- Sambruna, R. M., Maraschi, L., & Urry, C. M. 1996, *ApJ*, 463, 444
- Sanders, D. B., Phinney, E. S., Neugebauer, G., Soifer, B. T., & Matthews, K. 1989, *ApJ*, 347, 29
- Schödel, R., Ott, T., Genzel, R., et al. 2002, *Nat.*, 419, 694
- Shakura, N. I. & Sunyaev, R. A. 1973, *A&A*, 24, 337
- Shapiro, S. L., Lightman, A. P., & Eardley, D. M. 1976, *ApJ*, 204, 187
- Shu, F. 1991, *The physics of Astrophysics* (University science books, Mill Valley)

- Spinrad, H., Marr, J., Aguilar, L., & Djorgovski, S. 1985, *PASP*, 97, 932
- Spruit, H. C. & Kanbach, G. 2002, *A&A*, 391, 225
- Stiavelli, M., Moller, P., & Zeilinger, W. W. 1991, *Nat.*, 354, 132
- Stickel, M., Fried, J. W., Kuehr, H., Padovani, P., & Urry, C. M. 1991, *ApJ*, 374, 431
- Strohmayer, T. E. & Mushotzky, R. F. 2003, *ApJ*, 586, L61
- Sun, W. H. & Malkan, M. A. 1989, *ApJ*, 346, 68
- Sunyaev, R. A. & Trümper, J. 1979, *Nat.*, 279, 506
- Swartz, K. & Tennant, A. 2003, *astro-ph/0302203*
- Tanaka, Y. & Lewin, W. 1995, in *X-ray Binaries*, Cambridge University Press, Cambridge Astrophysics Series 26, p. 126
- Tanaka, Y. & Shibazaki, N. 1996, *ARA&A*, 34, 607
- Taub, A. H. 1948, *Phys. Rev.*, 74, 328
- Taylor, G., Ulvestad, J., & Perley, R. 2004, *VLA Observational Status Summary*
- Terashima, Y. & Wilson, A. S. 2003, *ApJ*, 583, 145
- Terrell, N. J. J. 1972, *ApJ*, 174, L35
- Urry, C. M. & Padovani, P. 1995a, *PASP*, 107, 803
- Urry, C. M. & Padovani, P. 1995b, *PASP*, 107, 803
- van der Klis, M. 1989, in *Timing Neutron Stars*, ed. H. Ögelman & E.P.J. van den Heuvel (Dordrecht: Kluwer), 27
- van der Klis, M. 1994, *ApJS*, 92, 511
- van der Klis, M. 1995, in *X-ray Binaries*, ed. W. H. G. Lewin, J. van Paradijs, & E. P. J. van den Heuvel (Cambridge: Univ. Cambridge Press), 252
- Vaughan, B. A. & Nowak, M. A. 1997, *ApJ*, 474, L43

- von Montigny, C., Bertsch, D. L., Chiang, J., et al. 1995, *ApJ*, 440, 525
- Walker, R. C., Dhawan, V., Romney, J. D., Kellermann, K. I., & Vermeulen, R. C. 2000, *ApJ*, 530, 233
- Watanabe, H., Kitamoto, S., Miyamoto, S., et al. 1994, *ApJ*, 433, 350
- Woo, J. & Urry, C. M. 2002, *ApJ*, 579, 530
- Wrobel, J. M., Taylor, G. B., & Gregory, P. C. 2001, *AJ*, 122, 1669
- Yuan, F., Markoff, S., & Falcke, H. 2002a, *A&A*, 383, 854
- Yuan, F., Markoff, S., Falcke, H., & Biermann, P. L. 2002b, *A&A*, 391, 139
- Zdziarski, A. & Gierlinski, M. 2004, astro-ph/0403683
- Zdziarski, A. A., Lubiński, P., Gilfanov, M., & Revnivtsev, M. 2003, *MNRAS*, 342, 355
- Zdziarski, A. A., Poutanen, J., Mikolajewska, J., et al. 1998, *MNRAS*, 301, 435
- Zensus, J. A. 1997, *ARA&A*, 35, 607
- Zhang, Y. H. 2002, *MNRAS*, 337, 609
- Zirbel, E. L. & Baum, S. A. 1995, *ApJ*, 448, 521

8

Acknowledgments

I would like to thank my referees Prof. Heino Falcke and Prof. Peter Schneider. Without my supervisor Prof. Heino Falcke this thesis would not be here. He greatly helped me with numerous discussions, motivation, and by posing new exciting questions, some of those have been discussed here. Prof. Peter Schneider helped me by discussing a number of problems and by giving advice. I am grateful that he agreed to referee my thesis.

I am indebted to my director Dr. Anton Zensus for giving me the possibility to work in his group at the Max-Planck-Institut für Radioastronomie. I thank him and Dr. Arno Witzel for guidance and discussions. I am also grateful for support by the International Max-Planck Research School (IMPRS) for Radio and Infrared Astronomy at the University of Bonn.

Prof. Peter Biermann pointed me to many open questions and motivated me to work in this active field. I have discussed many of my theoretical questions with Dr. Thomas Beckert and I thank him for his time and patience.

Numerous people at the 'Max-Planck-Institut für Radioastronomie' helped me during my time in Bonn. The friendly atmosphere and the warm welcome made it a pleasure to work here. I express my gratitude to all of them. I thank Dr. Richard Porcas for all those little questions, the sphere problem and all the fun we had; Dr. Alan Roy for reading parts of this thesis; Dr. Thomas Krichbaum, Dr. Eduardo Ros and Dr. Antonios Polatidis for the explanation of my observational problems; Dr. Walter Alef for computer support and his correlation efforts; and Dr. Andrei Lobanov for discussion during coffee.

Also people outside our institute had a strong influence on this work. I thank Dr. Ed Colbert for his collaboration on our radio observations, Dr. Jörn

Wilms for discussions on the timing properties of XRBs and Dr. Sera Markoff for collaboration on jet models.

Work life would have dull without my fellow students. I thank Tim Huege for many fruitful discussions, which helped this thesis to evolve; my roommates Andreas Brunthaler and Andreas Horneffer for sharing these enjoyable years with me. Also the students of the 'main VLBI floor' helped me significantly. Of those I would like to thank Matthias Kadler, Uwe Bach and Enno Middelberg especially.

Finally, I would like to thank my father Alfred and my brother Konrad for their support and encouragement.

Publications

This is a list of publications which have emerged from this thesis:

- *Population X: Are the super-Eddington X-ray sources beamed jets in microblazars or intermediate mass black holes?* Körtling, E., Falcke, H., Markoff, S. 2002, A&A Letters 382, L13
- *X-ray time lags from a pivoting power law in black holes*, Körtling, E., Falcke, H. 2004, A&A 414, 795
- *A Scheme to Unify Low-Power Accreting Black Holes - Jet-Dominated Accretion Flows and the Radio/X-ray Correlation*, Falcke, H., Körtling, E., and Markoff, S. 2004, A&A 414, 895
- *Radio Observations of Ultra-Luminous X-Ray Sources*, Körtling, E., Colbert, E., Falcke, H. 2004, in prep